論文 / 著書情報
Article / Book Information

題目(和文)	
Title(English)	Mechanical properties and microstructure of Al-Mg-Cu alloys processed by plastic deformation and aging heat treatment
著者(和文)	陳 宣良
Author(English)	Xuanliang Chen
出典(和文)	学位:博士（工学）, 学位授与機関:東京工業大学, 報告番号:甲第11783号, 授与年月日:2022年3月26日, 学位の種別:課程博士, 審査員:小林 郁夫,史 蹟,村石 信二,曽根 正人,木村 好里
Citation(English)	Degree:Doctor (Engineering), Conferring organization: Tokyo Institute of Technology, Report number:甲第11783号, Conferred date:2022/3/26, Degree Type:Course doctor, Examiner:,,,,
学位種別(和文)	博士論文
Type(English)	Doctoral Thesis

Mechanical properties and microstructure of Al-Mg-Cu alloys processed by plastic deformation and aging heat treatment

by

Xuanliang Chen

Doctoral Thesis

Department of Materials Science and Engineering

Tokyo Institute of Technology

2022

Acknowledgments

I would like to thank many people for their kind support during this Ph.D. work.

First and foremost, I would like to express my sincere gratitude to my supervisor Prof. Equo Kobayashi for his constant guidance and support. He enlightened me at the first glance of research and provided me the opportunities to participate in several conferences and to visit Norway, which are very important for my academic growth. I would also like to thank him for constructing a friendly atmosphere in our research group, making these years an entirely great experience. I am grateful to Prof. Tatsuo Sato, Dr. Minho O, and Mr. Hiroyasu Tezuka for their warm encouragement and thankful to Dr. Mami Mihara Narita for supporting my research work.

I would like to thank the members of my thesis committee, Prof. Ji Shi, Prof. Masato Sone, Prof. Yoshisato Kimura, and Prof. Shinji Muraishi for their insightful and meticulous comments and encouragement, which motivated me to broaden my research from various perspectives.

My sincere thanks also go to Prof. Randi Holmestad, Dr. Calin Daniel Marioara, Dr. Sigmund Jarle Andersen, Dr. Eva Anne Mørtsell, Dr. Jesper Friis, Dr. Adrian Lervik, and Dr. Jonas Kristoffer Sunde. Prof. Randi provided me with a valuable opportunity to join her TEM group at NTNU. Dr. Calin, Sigmund, and Jesper from SINTEF patiently and meticulously taught and helped me on modeling and first-principle calculations. Dr. Eva from Hydro aluminum helped me to start research about cyclic deformation. Dr. Adrian and Dr. Jonas helped me with TEM observations. The three months of studying and living in Norway in 2019 are fond memories in my mind.

I would like to acknowledge the technical support from Dr. Yu Kurokawa and Yuka Akimoto. My heartfelt appreciation goes to the Japanese Ministry of Education, Culture, Sports, Science and Technology (MEXT) for financial support.

My colleagues Dr. Daehan Kim, Dr. Dinh N. Pham, and Yujin Rhee have been my good friends throughout the years, whose advice and support have enriched my study time at Tokyo Institute of Technology. I am also grateful to all members of Equo Kobayashi laboratory for their kindness, friendship and cooperation. I acknowledge all the other people who helped me in some ways to complete my dissertation.

Finally, I wish to express my deepest gratitude to my parents for their infinite love, support, and understanding throughout my life.

Abstract of the present thesis

The Al-Mg-Cu alloy with a low Cu/Mg ratio is heat-treatable Al alloy and belongs to newly developing alloying systems. This alloy is expected to have potential applications in the automotive industry, due to its rapid aging hardening, good formability and corrosion resistance. The mechanical properties and microstructure of Al-Mg-Cu alloys processed by plastic deformation and aging heat treatment have been studied by using several experimental techniques.

The research content of this thesis consists of three parts: Chapter 2: Effect of pre-deformation on age-hardening behavior in the Al-3Mg-1Cu alloy. Chapter 3: Precipitation processes and structural evolutions of various GPB zones and two types of S phases in a cold-rolled Al-3Mg-1Cu alloy. Chapter 4: Enhanced mechanical properties in an Al-Mg-Cu alloy processed by the combination of cyclic deformation and aging heat treatment.

The effects of 3%–50% cold rolling (CR) following solution heat treatment on the age hardening of an Al-3Mg-1Cu alloy have been investigated. Pre-deformation has a strong effect on subsequent age-hardening behavior. Rapid age hardening of the base alloy is absent in CR alloys. Instead, recovery was observed in the highly pre-deformed samples. The hardness peak advances with the increasing reduction rate. A larger fraction of precipitates was observed along the dislocation lines and the S phase formation peaks in the DSC curves of the CR alloys appeared at lower temperatures, indicating that the precipitation of S phases was accelerated by deformation-induced dislocations. Since Guinier–Preston–Bagaryatsky (GPB) zones were observed in the 20 min aged CR samples and two types of S phases were detected in the CR samples aged for 1 day, the GPB zones and S phases were thought to cause first and second hardness increases in cold rolled samples, respectively. The contributions of clusters/GPB zones and S phases to hardness were evaluated in both non-deformed and deformed alloys for comparison. The hardness of the plateau was found to be dynamically balanced by the dissolution of clusters/GPB zones and the formation of S phases. In the base alloy, clusters/GPB zones and S phases contribute together to the peak hardness, and clusters/GPB zones are still stable even after long-term aging. However, the contribution of GPB zones becomes lower in the CR alloys, and all of them will transform into S phases after long-term aging. It was found that paint-baking (443 K

for 20 min) performed on the as-rolled samples resulted in a good strength-elongation balance because of the annihilation of dislocations and the formation of GPB zones. The results are significant for the development of combined mechanical deformation and heat treatment processes.

The GPB zone and the S phase are the key strengthening precipitates in Al-Mg-Cu alloys. However, their respective structures evolution during aging has not been fully understood. In this work, the precipitation process and the structure of precipitates in an Al–3Mg–1Cu (wt.%) alloy were investigated. A series of common GPB zones and a novel type of GPB zone named “GPBX” were observed in the cold-worked samples aged at 443 K for 20 min. In the subsequent aging, two types of S phases were found to coexist, labeled S-I and S-II phases. Density functional theory calculation results indicate that the GPBX zone is stable and the S-I and S-II phases have almost the same formation enthalpy. Common GPB zones transform to S-I phases, while S-II phases are formed from GPBX zones preferentially along dislocation lines. Also, a structural model for the S-II phase is proposed, supported by atomic-resolution HAADF-STEM in association with first-principles energy calculations. The misorientation angles of the S phases were discussed. Changes in morphologies of two types of S phases during aging were observed, and related growth mechanisms were proposed. Finally, the similar behavior of Cu and Si regarding the formation of precipitates has been discussed. GPB zones were confirmed to be structurally linked to β” and U2 precipitates reported in 6xxx (Al-Mg-Si) series Al alloys. The complex structure mixed with different types of precipitates is confirmed. The revealed precipitate structures and their interrelationships may provide insights into future alloy design.

Aging is known as a traditional strengthening method for heat treatable Al alloys. Recently, cyclic strengthening has received widespread attention as a novel method. Cyclic deformation was applied to introduce dislocations and promote cluster formation in an Al-Mg-Cu alloy. The cyclically strengthened (CS) samples have both higher strength and ductility than the peak-aged samples. The aging behavior of CS samples as well as the effect of pre-aging on cyclic strengthening were also studied. The recovery and precipitation promotion were found during the aging of CS samples regardless of the pre-aging for 20 min. Since more clusters (or precipitates) have been formed in pre-aged CS samples, they show higher strength than those CS samples without pre-aging. Interestingly, after subsequent aging, the mechanical properties of

CS samples with and without pre-aging for 20 min became the same. This indicates that there is no essential difference between clusters formed during cyclic deformation and aging. In summary, aging and cyclic deformation methods were combined to maximize the effects of precipitation strengthening and work hardening. The strength limit obtained by individual aging or cyclic deformation methods was successfully broken through. These provide new insights into alloy strengthening.

Overall, this study deepens the understanding of relationships among microstructure (at atomic- and nano-scale), mechanical properties, plastic deformation and aging heat treatment of aluminum alloys.

List of Acronyms

AA	artificial aging
APT	atom probe tomography
AQ	as-quenched
AR	as-rolled
BF	bright field
CR	cold rolling
CS	cyclic strengthening
DF	dark-field
DFT	density functional theory
DSC	differential scanning calorimetry
EDS	energy dispersive spectroscopy
FE-SEM	field emission scanning electron microscopy
FCC	face-centered cubic
FFT	fast Fourier transform
GP	Guinier–Preston
GPB	Guinier–Preston–Bagaryatsky
HAADF	high-angle annular dark-field
HRTEM	high-resolution transmission electron microscopy
IFFT	inverse fast Fourier transform
NA	natural aging

OR	orientation relationship
PA	peak aging
PBE	Perdew–Burke–Ernzerhof
PLC	Portevin–Le Chatelier
RK	Radmilovic Kilaas
RT	room temperature
PW	Perlitz Westgren
SADP	selected area diffraction pattern
SEM	scanning electron microscopy
SHT	solution heat treatment
SSSS	supersaturated solid solution
STEM	scanning transmission electron microscopy
TEM	transmission electron microscopy
UTS	ultimate tensile strength
VASP	Vienna ab initio simulation package
XRD	X-ray diffraction
YS	yield strength

Table of Contents

Chapter 1. General Introduction

1.1 Aluminum and aluminum alloy

1.1.1 Background

Aluminum is the third most abundant element in the earth's crust after oxygen and silicon, with the chemical symbol of Al and the atomic number of 13. It is a soft and ductile silver-white metal, generally obtained by smelting bauxite ores.

Aluminum has a face-centered cubic lattice structure, which has many slip systems. Therefore, aluminum has high plasticity and is easy to be processed into various shapes. However, the strength of pure aluminum is very low (about 80 MPa), limiting its application as a structural material. The strength can be improved by adding trace elements to form aluminum alloys. Typical alloying elements are copper, magnesium, manganese, silicon, tin, and zinc.

1.1.2 Classification of aluminum alloys

Al alloys are principally classified into cast alloys and wrought alloys, both of which are further subdivided into heat-treatable and non-heat-treatable categories, as shown in Fig. 1.1. In general, cast alloys have lower costs, while wrought alloys have better mechanical properties.

Wrought and cast alloys use different identification systems. Wrought alloy uses four-digit numbers to identify alloying elements. The first digit indicates the main alloying elements. The second digit indicates the variant of alloys. The third and fourth digits indicate the specific alloy in the series. Cast alloys use four to five-digit numbers with a decimal point. The digit in the hundreds place represents the alloying elements, while the digits after the decimal point represent the form.

According to whether the alloy can be strengthened by aging heat treatment, wrought alloys are divided into 2xxx series Al-Cu, 6xxx series Al-Mg-Si and 7xxx series Al-Zn-Mg of heat-treatable alloys and 1xxx series pure Al, 3xxx series Al-Mn, 4xxx series Al-Si, and 5xxx series Al-Mg of non-heat-treatable alloys.

The heat-treatability of Al alloys was accidentally discovered by German researcher Alfred Wilm [1]. He conducted solution heat treatment (SHT) at 798 K on an Al-Cu-

Mg-Mn alloy on Saturday afternoon. When he measured the hardness next Monday, he was surprised to find that the alloy was much stronger. The reasons are as follows: in these heat-treatable alloys, the solubility of solid solution elements decreases as the temperature decreases. Therefore, after SHT and quenching to room temperature, a supersaturated solid solution is formed. These supersaturated solute atoms are unstable at room temperature and will spontaneously escape from the Al matrix to form precipitates, resulting in precipitation strengthening.

In non-heat-treatable alloys, the commonly used strengthening methods are work hardening and solid solution strengthening. These above-mentioned strengthening methods will be explained in detail in the later section.

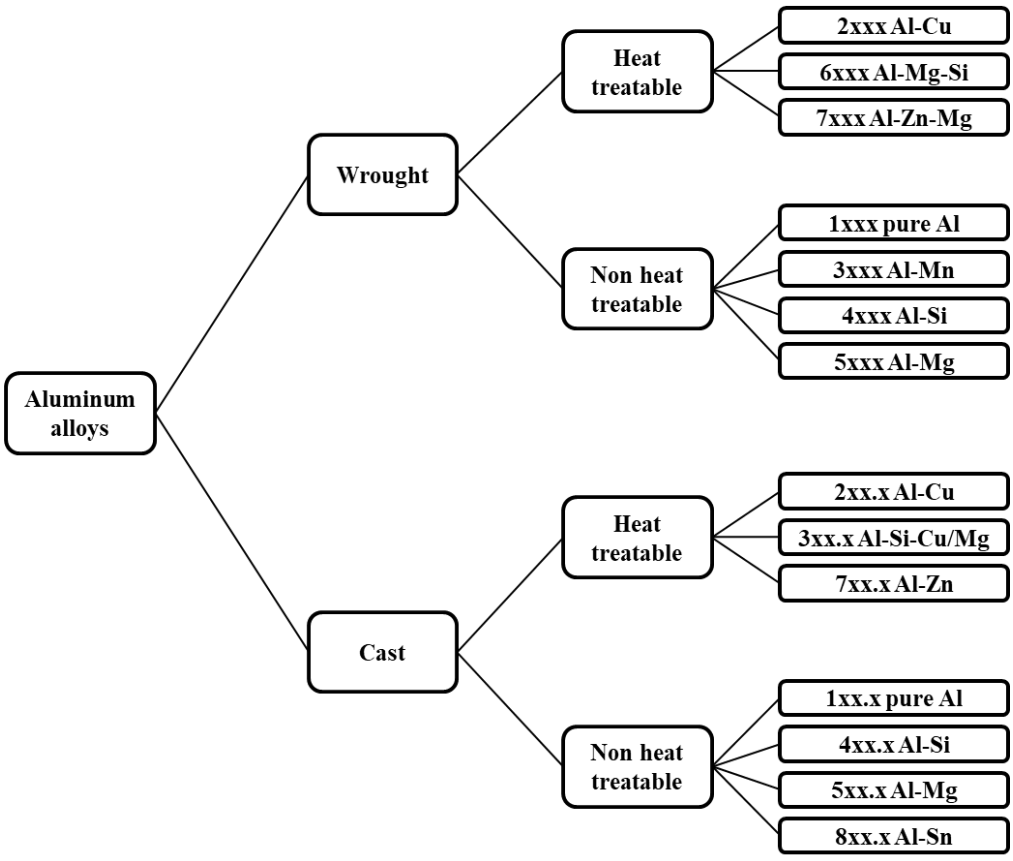

Fig. 1.1 Classification of aluminum alloys.

1.1.3 Application of Aluminum alloys in the automobile industry

In recent decades, the global warming caused by the greenhouse effect has become severe. Especially with the popularity of automobiles, the emission of automobile

exhaust has increased year by year, which has worsened the situation and caused serious environmental pollution problems.

As a response, countries around the world have reached a consensus and unanimously decided to limit greenhouse gas emissions [2]. In order to improve fuel efficiency, light-weighting has become an important issue. Aluminum alloys are widely used in engineering structures and components where lightweight is required. The density of aluminum is only 1/3 of that of steel, so weight savings of parts up to 50 % can be achieved by light-weighting with aluminum [3]. A senior automotive engineer predicts that every part of cars can be made of aluminum alloys, and more aluminum alloy parts will be applied to cars in the future [4]. In addition to the advantage of weight reduction, the impact toughness of aluminum alloy materials is higher than that of steel, which increases the safety of automobiles. The aluminum alloy also has good corrosion resistance and an extremely high recycling rate, which have become important factors to promote the application of aluminum parts [5].

2xxx, 5xxx, 6xxx, and 7xxx series aluminum alloys are commonly used in automobiles.

(1) 2xxx series Al-Cu alloys

2xxx series Al-Cu alloys are represented by 2017 and 2024, which are also known as duralumin. They have superior performance in terms of strength and cutting. However, their corrosion resistance is poor due to the high content of Cu. These alloys are generally used for mechanical parts and structural materials. Commercial 2xxx Al alloys always contain Cu and Mg as the main alloying elements. Two precipitation strengthening phases can be formed during aging, namely S (Al_2MgCu) and θ (Al_2Cu) phases. S and θ phases preferentially form in the Al alloys with high and low Mg/Cu ratios, respectively. S and θ phases coexist when the Mg/Cu ratio is in a moderate range. The strengthening effect of the metastable S phase is the highest, and that of the metastable θ phase is slightly inferior. The strengthening effect is the largest when both metastable S and θ phases are present in the alloy.

(2) 5xxx series Al-Mg alloys

5xxx series Al alloys are medium-strength Al alloys with Mg as the main alloying element and are non-heat-treatable. The strengthening methods are mainly solid solution strengthening of Mg solute atoms, work hardening, and fine grain

strengthening. Al-Mg alloys have good weldability and corrosion resistance, are often used in automotive, construction, and marine applications. Serrations always appear on the stress-strain curves of Al-Mg alloys, also known as the Portevin–Le Chatelier (PLC) effect, which is associated with the competition between diffusing solutes pinning dislocations and dislocations breaking free of this stoppage [6]. These will reduce the surface quality, so Al-Mg alloys are generally used for automobile interior panels.

(3) 6xxx series Al-Mg-Si alloys

6xxx series Al-Mg-Si alloys have medium strength, superior corrosion resistance and welding performance. They are suitable for automobile exterior panels. They have low strength and good press-forming ability after SHT and have a significant bake hardening effect in the subsequent paint baking process. The precipitation strengthening phase is Mg_2Si.

(4) 7xxx series Al-Zn-Mg alloys

The strength of 7xxx series Al alloys is higher than that of other series Al alloys. 7xxx series Al alloys have good wear resistance and weldability, but poor formability and corrosion resistivity. They are generally used in automobile bumpers, suspensions and body frames that require low formability. The main alloying elements are Zn, Mg and Cu. The precipitation strengthening phase is $MgZn_2$. With the improvement of material strength requirements for automobile lightweight, high-strength Al-Zn-Mg alloys have gradually become one of the hot spots of material development in the world.

1.2 Strengthening mechanisms in metals

The deformation of metals is divided into two stages: elastic deformation and plastic deformation, with the yield point as the dividing point. The movement of dislocations causes plastic deformation of the material. Therefore, the strength can be improved by obstructing the movement of these dislocations. In this section, we will introduce four common strengthening mechanisms in metals.

1.2.1 Fine-grain hardening

Also known as grain boundary strengthening, it refers to a strengthening method through grain refinement. It is also the only method that improves both the strength and ductility of the four strengthening methods.

When the polycrystalline metal material undergoes plastic deformation, the slip system with a large Schmidt factor in some grains starts first. However, since adjacent grains have different orientations and the grain boundary is much more disordered than inside of the grain, the movement of dislocations will be hindered when they slip to the grain boundary. Therefore, the smaller the crystal grains, the more the grain boundaries, the stronger the hindering effect on dislocations, leading to the more significant the strengthening effect. The ductility can be also improved, because the plastic deformation is more uniform in fine-grained materials, and stress concentration is less likely to occur.

The relation between yield stress and grain size is described mathematically by the Hall–Petch equation [7]:

$$\sigma_y = \sigma_0 + \frac{k_y}{\sqrt{d}} \quad (1.1)$$

where σ_y is the yield stress, σ_0 is the resistance of the lattice to dislocation motion (a material constant), k_y is the strengthening coefficient (a material constant), and d is the average grain diameter.

Note that this formula will no longer be applicable when the grain size is reduced to about 10 nm. Because the small enough grains undergo other yielding mechanisms, such as grain boundary sliding [8].

1.2.2 Solid solution strengthening

Solid solution strengthening refers to the phenomenon that the strength and hardness of pure metal can be improved by introducing appropriate alloying elements. The reason can be attributed to the interaction of solute atoms and dislocations.

Solute atoms induce local lattice distortions in the crystal lattice, resulting in stress fields that hinder the movement of dislocations and thus increase the strength. Solid solutions can be classified into interstitial and substitutional according to the size difference between solute and solvent atoms [9], as shown in Fig. 1.2. It can also be classified into finite and infinite solid solutions according to the solid solubility of solute elements in the solvent. When it is below the solid solubility limit, more solute atoms always lead to greater strengthening effects. However, when it exceeds the solid solubility limit, such as the material undergoing SHT and quenching, an unstable

supersaturated solid solution will be obtained. Supersaturated solute atoms will leave the matrix to form a second phase, leading to precipitation strengthening.

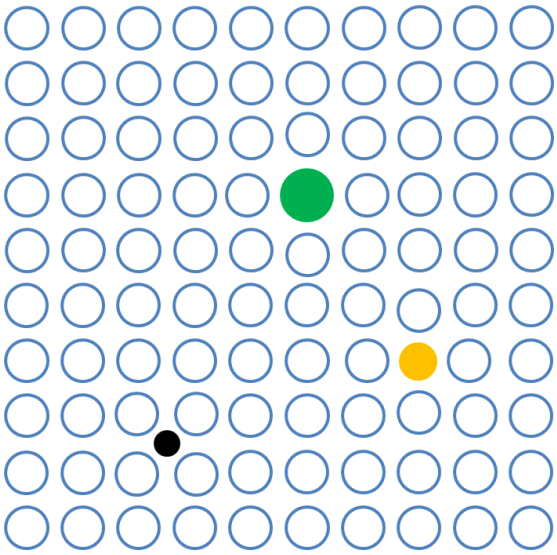

Fig. 1.2 Interstitial and substitutional solute atoms in a lattice.

1.2.3 Precipitation strengthening

Precipitation strengthening, also called precipitation hardening or age hardening, refers to a heat treatment process that forms solute atom segregation zones and/or dispersed particles in a supersaturated solid solution to cause strengthening.

Precipitation strengthening is the most commonly used strengthening method for aluminum alloys. The schematic diagram of precipitation strengthening for Al alloys is shown in Fig. 1.3, it can be completed in 3 steps:

1. Heat the material to a temperature between solvus and solidus to obtain a uniform single α phase solid solution.

2. Quench the material to a low temperature (usually room temperature or 273 K) to get the supersaturated solid solution. Since the temperature is too low and the solute atoms have no time to diffuse, the organization still maintains the single α phase after quenching, although the equilibrium organization should also contain the second phase.

3. Heat the material to an appropriate temperature to increase the diffusivity, so that the supersaturated solute atoms can aggregate to form a high density of clusters, which are evenly distributed within the matrix. Then these clusters will grow into metastable

phases, such as Guinier–Preston (GP) or Guinier–Preston–Bagaryatsky (GPB) zones [10]. As the aging further progresses, the metastable phase will become the stable phase, such as S and θ phases of 2xxx Al alloys, β phase of 6xxx Al alloys, and η phase of 7xxx Al alloys.

The specific precipitation process is very complicated and varies from each alloy system. This thesis mainly studies the Al-Mg-Cu alloy system, the detailed precipitation process will be introduced in section 1.3.

Fig. 1.4(a, b) shows two mechanisms for precipitation strengthening: cutting through and bowing around mechanisms, corresponding to deforming and non-deforming precipitates, respectively. The strengthening mechanism varies from Al alloy systems due to different precipitate phases. Even in the same alloy, the strengthening mechanism can also change in different aging stages. As shown in Fig. 1.3(b) and 1.4(c), the precipitate size is small in the under-aged state, and the precipitates are easy to be cut through by dislocations. While the precipitate size becomes large after over-aging, dislocations tend to bypass the precipitates. There is a critical or optimal precipitates radius at which max strengthening occurs, corresponding to the peak aging states.

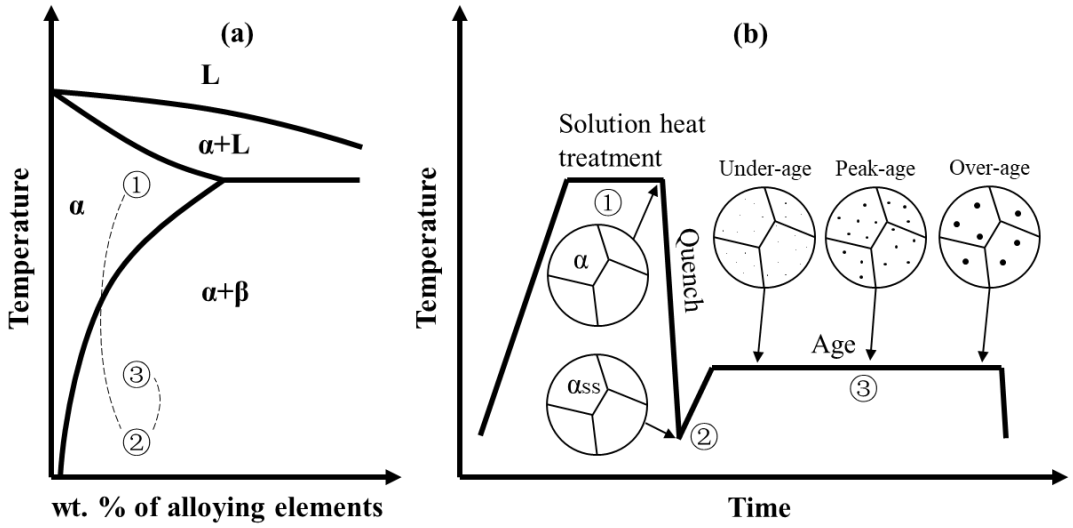

Fig. 1.3 Schematic diagram of precipitation strengthening for Al alloys. (a) A phase diagram of binary Al alloys. (b) Heat treatment history.

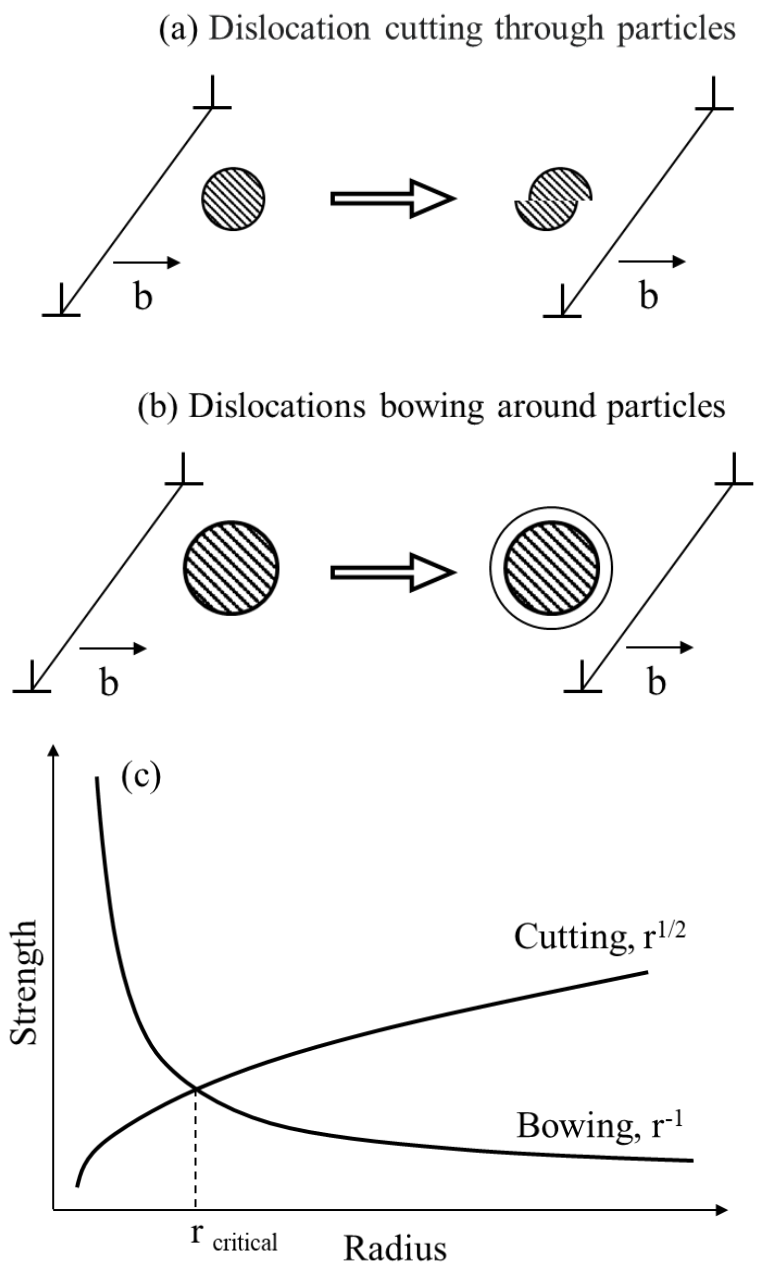

Fig. 1.4 Schematic diagrams of dislocation (a) cutting through and (b) bowing around particles. (c) Schematic graph of the strength changes with particle radius under the cutting and bowing mechanisms.

1.2.4 Work hardening

Not only other factors can hinder the movement of dislocations to strengthen the material, but dislocations' interaction with each other can also lead to the strengthening.

Work-hardening refers to the phenomenon that the strength and hardness of metal materials increase when they are plastically deformed below the recrystallization temperature. The plastic deformation process is accompanied by the dislocation generation and movement within the crystal structure of the material. With the continuous generation of dislocations, a large number of dislocations will interact with each other and thus hinder their further movement.

Quantification of work hardening can be carried out by the following formula [11]:

$$\tau = \tau_0 + G\alpha b\rho^{1/2} \quad (1.2)$$

Where τ_0 is the intrinsic strength, G is the shear modulus, α is a correction factor specific to the material, b is the Burgers vector, and ρ is the dislocation density.

There are many types of plastic deformation that cause work hardening, such as cold rolling and cyclic plastic deformation used in this thesis. Cold rolling refers to a processing method of passing the metal blank between the upper and lower rolls below the recrystallization temperature to reduce the thickness. Cyclic plastic deformation refers to the method of applying alternating tension and compression loading on materials. In this thesis, ultra-short cycles are adopted to prevent the influence of the formation or propagation of fatigue cracks on the experimental results.

1.3 Age-hardening in Al-Mg-Cu alloys

As mentioned above, Al-Mg alloys are widely used for automobiles because of their good weldability and corrosion resistance. However, softening always occurs in classical Al-Mg alloys during heat treatments such as the paint baking treatment (i.e. heat treating the body panel sheets for 20-30 min at temperatures between 433K and 453 K after painting). Si and Cu can be added into Al-Mg alloys to overcome age-softening. Al-Mg-Si alloys belong to the 6xxx series Al alloy that has been extensively studied and commercially used. However, there are problems with the application of Al-Mg-Si alloys. The cluster (1) formed during natural aging has a negative effect on subsequent precipitation, limiting the storage at room temperature or requiring additional pre-aging to prevent the formation of cluster (1) [12]. The Al-Mg-Si alloy is easy to be over-aged when exposed to the sun in summer due to its ‘relatively fast’ hardness peak. The basic properties of the Al-Mg-Cu alloy have been investigated, this alloy is expected to solve the above problems, but there is still a lack of systematic

research to expand the potential application. Therefore, this thesis mainly studies Al-Mg-Cu alloys, and the basic knowledge about the aging of Al-Mg-Cu alloys will be introduced in this section.

1.3.1 Age-hardening behavior

The typical age-hardening behavior of an Al-Mg-Cu alloy is shown in Fig. 1.5. There are two characteristics of this alloy, one is “rapid age-hardening”: the first stage of age hardening starts immediately and can be completed within approximately 60 s at 443 K. The hardness increment of the first stage accounts for 60% of the total. The other is “hardness plateau”, where the hardness remains the same for a long time, appearing between two hardening stages [13].

After the plateau, the precipitates continue to grow, leading to the phenomenon that the strength firstly increases and then decreases as depicted in Fig. 1.4(c). In fact, there are defects such as vacancies, dislocations, and grain boundaries in the material, which make the nucleation and growth of each precipitate not homogeneous, so the actual situation is more complicated.

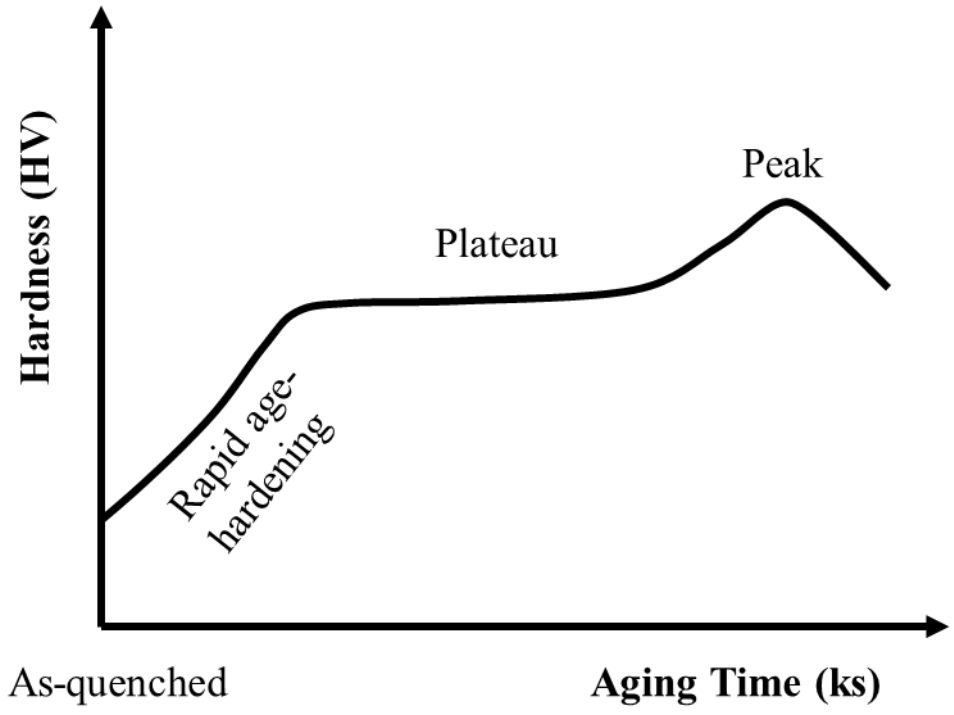

Fig. 1.5 Age-hardening behavior of an Al-Mg-Cu alloy.

1.3.2 Precipitation process

There have been many studies and discussions about the precipitation process of forming S, as listed in Table 1.1.

In 1952, Bagaryatsky firstly proposed the precipitation sequence as below [14]:

$$SSSS \rightarrow GPB \rightarrow S'' \rightarrow S' \rightarrow S$$

In 1965, Wilson et al. observed S' phases that grow along dislocations [15]. In 1976, Mondolfo pointed out that S and S' phases have the same structure [16]. Then S.P. Ringer et al. added clusters into the precipitation process and proposed that GPB may nucleate at the site of clusters [17–20]. Next, Ratchev et al. and Charai et al. further modified the precipitation process [21–23]. Among them, Ratchev et al. proposed that the precipitation process on dislocations is different from that in the Al matrix [22].

Zhang et al. [24] and Radmilovic et al. [25] reported that the S phase has different variants, S-I and S-II. Subsequently, in 2007, Wang et al. proposed the precipitation process of S-I to S-II [26]. In 2010, Feng et al. reported that GPB zones instead of Cu–Mg clusters are detected near dislocations in the initial stage of the aging process, and both S-I and S-II phases were observed on the dislocation [27].

In 2011, Sha reported that fine-scale, equiaxed solute clusters, GPB zones and S phase precipitates were found to coexist in the AA2024 alloy at the peak hardness condition using atom probe tomography (APT) [28].

With the further development of precipitation theory in recent years, without considering S-I and S-II variants, the generally accepted precipitation sequence is as follows [29]:

$$SSSS \rightarrow \text{Cu/Mg clusters} \rightarrow \text{GPB zones } (S'') \rightarrow S' \rightarrow S$$

S' phase is partially coherent with the matrix, corresponding to the peak-aged state. S phase is the stable precipitate, corresponding to the over-aged state. Since the S' and S phases have the same structure with only slightly different lattice parameters [30], the notation of "S' phase" is often omitted [31].

The formation mechanisms and structural differences of S-I and S-II phases are still unclear, and the influence of dislocations on their precipitation process lacks further systematic research. These will be presented and discussed in detail later in this thesis.

Table 1.1 History of research on precipitation sequence to form the S phase in Al-Cu-Mg or Al-Mg-Cu alloys.

	In Matrix	On Dislocations
1952 Y.A. Bagaryatsky	SSSS → GPB → S'' → S' → S	
1965 R.N. Wilson and P.G. Partridge		S' on dislocation
1976 L.F. Mondolfo	S and S' phases have the same structure	
1996-1998 S.P. Ringer et al.	SSSS → Cu/Mg clusters → GPB → S	
1998-1999 P. Ratchev et al.	SSSS → Cu/Mg clusters (GPB) → S'' → S'	SSSS → S'' → S'
2000 A. Charai et al.	SSSS → Cu/Mg clusters → GPB → S'' → S' → S	
2007 S. Wang et al.	SSSS → Cu/Mg clusters → GPB /S''→ S I → S II	
2010 Z. Feng et al.		SSSS → GPB → S I → S I + S II
2011 G. Sha et al.	SSSS → solute clusters → GPB zones + solute clusters → GPB zones + solute clusters + S → S	
Recently	SSSS → Cu/Mg clusters → GPB zones (→ S') → S	

1.3.3 Precipitation phases

1. clusters and GPB zones

Clusters are used to describe regions in the matrix where solute content is more abundant than the nominal composition. GPB zones are also defined as fine solute enriched regions. The boundaries between them are blurred, and sometimes they are not even distinguished. In order to clarify this question, Komiya et al. used APT to investigate the shape and concentration of solute clusters and GP zones [32]. It is defined that clusters are solute atoms aggregated together without a definite structure, whereas GP zones possess a definite structure.

Bagaryatsky [14] and Silcock [33] were among the first authors to study the microstructure development in Al-Cu-Mg alloys during aging. The diffuse streaks/spots were noticed from rotating crystal X-ray diffraction experiments. Silcock envisioned that the diffuse streaks/spots were due to the formation of rod-shaped GPB zones with a diameter of 1-2 nm and a length of 4-8 nm.

After decades of continuous research on GPB zones by many scientists [19,23,34–36], Kovarik et al. [37–40] finally revealed the atomic structure of GPB through high-angle annular dark-field scanning transmission electron microscopy (HAADF-STEM), and named various GPB zones based on the number of containing solute atoms, as shown in Fig. 1.6.

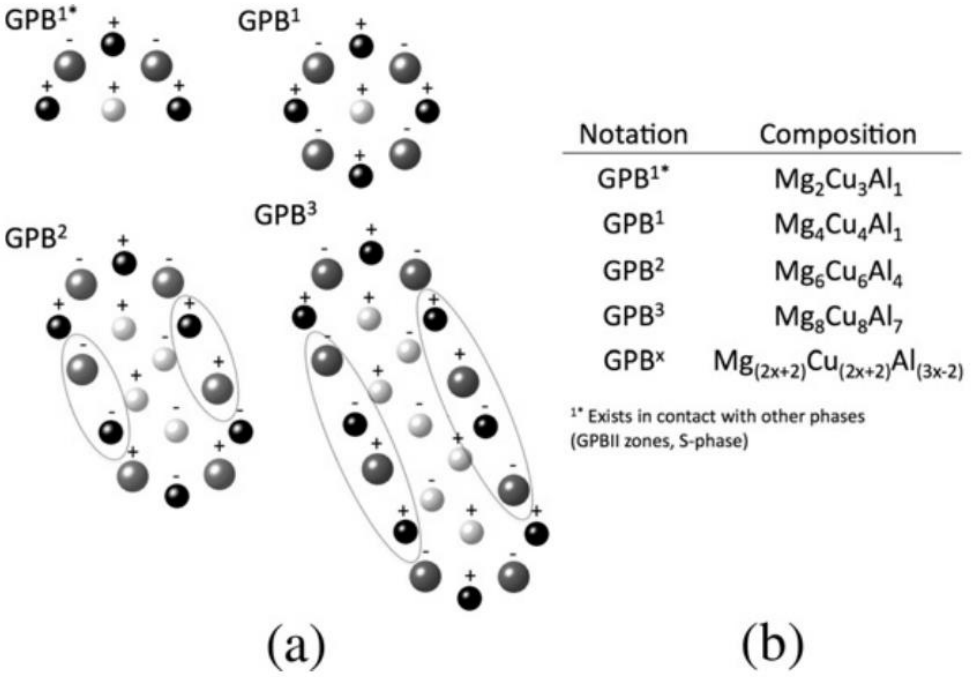

Notation	Composition
GPB^{1*}	$Mg_2Cu_3Al_1$
GPB^{1}	$Mg_4Cu_4Al_1$
GPB^{2}	$Mg_6Cu_6Al_4$
GPB^{3}	$Mg_8Cu_8Al_7$
GPB^{x}	$Mg_{(2x+2)}Cu_{(2x+2)}Al_{(3x-2)}$

^{1*} Exists in contact with other phases (GPBII zones, S-phase)

Fig. 1.6 (a) Structural relationship between the 1D-GPBx crystals. The 1D-GPBx are depicted along their periodic direction. The plus and minus signs indicate the position of the atoms along z in these 1D periodic cells: plus, z = 0.5; minus, z = 0. (b) Stoichiometries of the 1D crystals of the GPB zones [39].

2. S phases

The models of S phases proposed in history are shown in Fig. 1.7.

In 1943, Perlitz and Westgren proposed the first model (PW model) of the S phase based on X-ray diffraction (XRD) work [41]. The crystal structure is determined to be orthorhombic (Cmcm, a=0.400 nm, b=0.923 nm, c=0.714 nm) and the formula unit is Al_2CuMg. In 1976, Mondolfo [16] proposed a modified PW model (Mondolfo model) with the space group P1 and with atomic positions shifted for Cu and Mg atoms. From 1999 to 2001, due to the inconsistency between high-resolution TEM (HRTEM) observation and simulated image, Radmilovic et al. [25] and Kilaas et al. [42] proposed a different S-phase model (referred to as the RK model) by exchanging Cu and Mg positions to fit simulated images with the experimental observations. This proposal was supported by Majimel et al. [43] using HRTEM but was opposed by Wolverton et al. using first principle calculations [44]. Finally, in 2011, Liu et al. proved that the structure of the S phase conforms to the PW model by means of the combination of experiments and calculations [45].

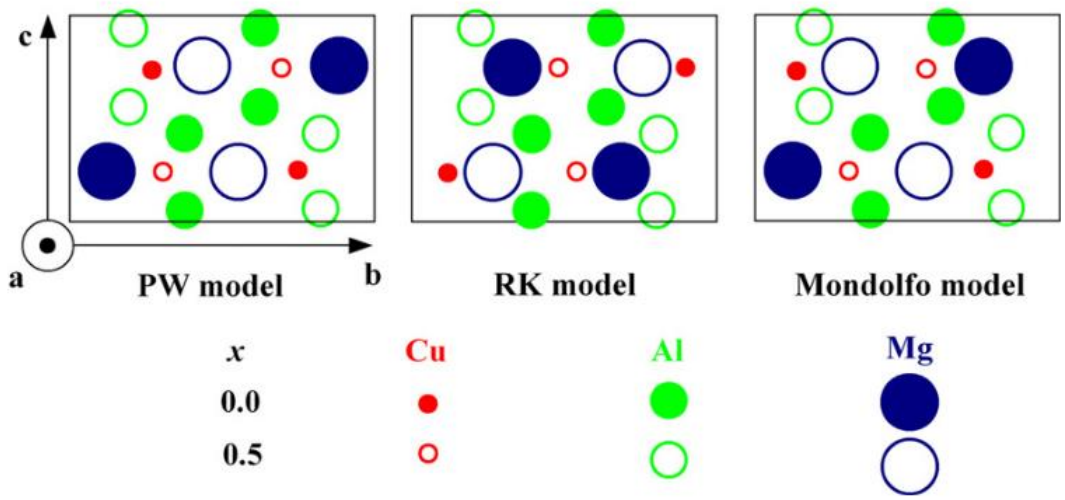

Fig. 1.7 Schematic unit cells of the existing controversial structure models for S-phase, projected along the [100]S direction. a, b and c are the lattice vectors, and x is the fractional coordinates of atoms in the a or [100]S direction. In the Mondolfo model, one of the (001)S Cu–Mg atomic layers is shifted along [010]S with respect to that in the PW model. The difference between the RK model and the PW model is that the Cu atoms and the Mg atoms are swapped [45].

1.4 Heat treatments process for Al alloys

Precipitation strengthening induced by aging heat treatment is the most common and important strengthening method for heat-treatable Al alloys. Aging heat treatment can be classified into many types according to the process, including one-step aging, two-step aging (sometimes even multi-step), deformation aging and so on.

1.4.1 One-step aging

One-step aging is the simplest aging process. After SHT and quenching, the material is directly aged at a certain temperature. Note that isothermal aging at room temperature is called natural aging (NA), and isothermal aging at elevated temperature is called artificial aging (AA). It is easier to nucleate but hard to grow during NA, so the main strengthening effects are from dispersed nano-sized clusters and/or GP(B) zones. The diffusivity during AA is higher, leading to faster precipitation and coarser precipitates. The one-step aging behavior of Al-Mg-Cu alloys has been introduced in Section 1.3.

1.4.2 Two-step aging

Two-step aging refers to the heat treatment of maintaining a period at room temperature after SHT and quenching, and then performing aging at elevated temperature. This is not rare in the industry. For example, the produced automobile body panels will inevitably undergo natural aging before being delivered to the car factory for paint baking.

Mihara has studied the two-step aging in Al-Mg-Cu(-Ag) alloys, as shown in Fig. 1.8(a) [46]. It was found that a higher hardness peak could be obtained if the material was pre-aged at 323 K for 1.2 ks. This is because pre-aging at low temperature can obtain more nuclei of precipitates, so that the finer precipitates will be formed during the subsequent aging. Note that this phenomenon was not seen in the Ag-added alloys.

For the same reason, two-step aging also leads to a higher hardness peak in Al-Zn-Mg alloys [47]. However, two-step aging in some Al-Mg-Si alloys results in an opposite effect, as shown in Fig. 1.8(b) [48]. The reason lies in clusters. Al-Mg-Si alloys have cluster (1) and cluster (2) formed at RT and temperature above 373 K, respectively. Cluster (1) cannot transform into the β'' phase like cluster (2) does during subsequent aging, but instead occupies solute atoms necessary for the β'' phase formation, resulting in fewer β'' phases at the peak state.

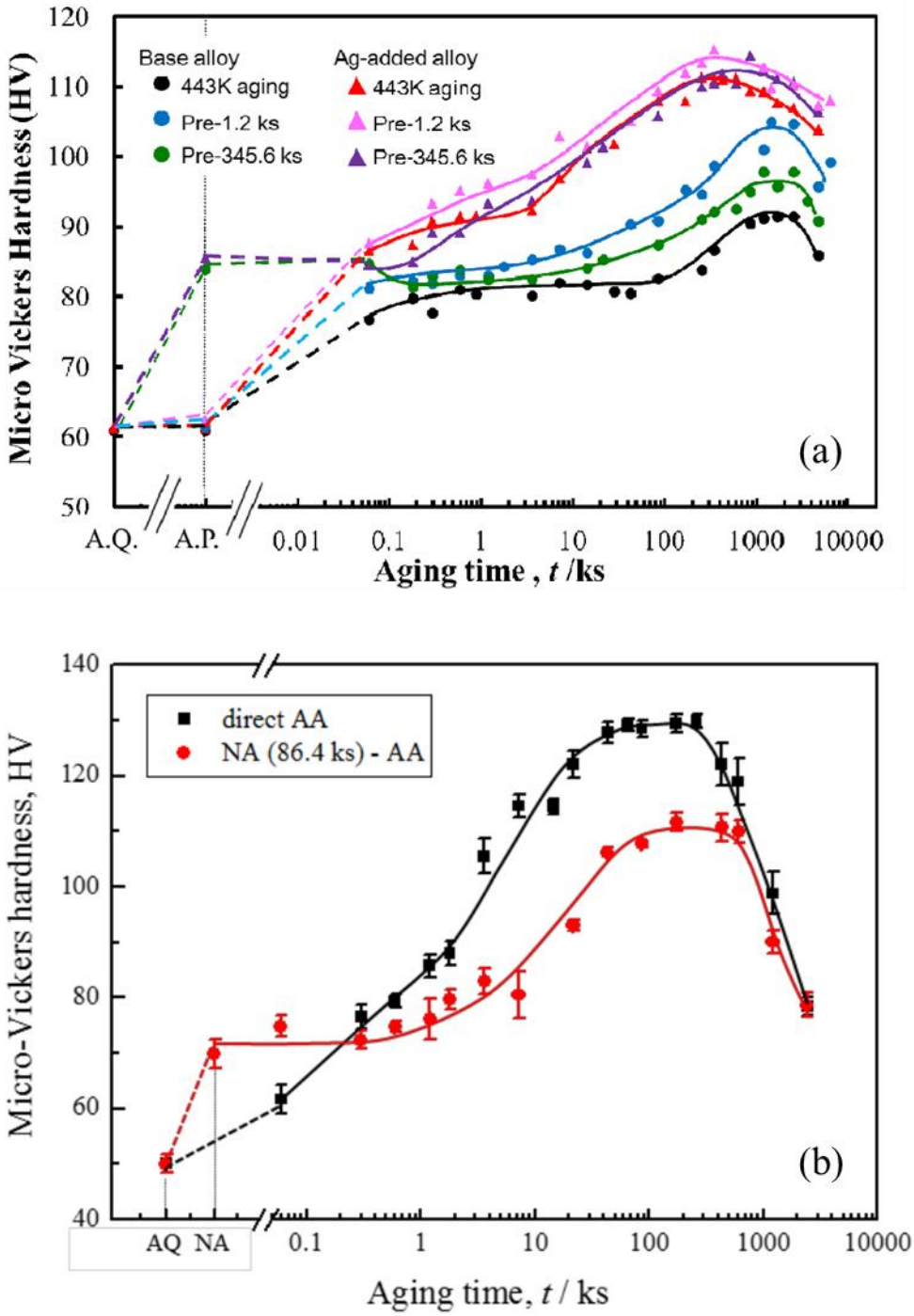

Fig. 1.8 (a) Two-step aging (pre-aging at 323 K) effects on the hardness for the Base (Al-Mg-Cu) and Ag-added (Al-Mg-Cu-Ag) alloys [46]. (b) Hardness changes for the Al-Mg-Si alloy during artificial aging at 443 K directly and two-step aging after natural aging at RT for 86.4 ks [48].

1.4.3 Deformation aging

Deformation aging refers to an aging method combined with plastic deformation. A representative example is that the material is firstly solution heat treated and quenched, then cold deformed at RT, finally subjected to aging. Both cold rolling and cyclic deformation combined with aging used in this thesis belong to this mode and will be investigated and discussed later.

A large number of dislocations can be introduced into the alloy during the cold deformation before aging. These dislocations will promote the diffusion of solute atoms to form precipitates. They can also help to eliminate the precipitate free zone near grain boundaries. A comprehensive effect of work hardening and precipitation strengthening can be achieved by the interaction between dislocations and precipitates.

In order to designate a variety of treatments simply and clearly, a standardized system has been developed, as shown in Table 1.2 [49,50].

Table 1.2 Common heat treatment in aluminum alloy.

	Heat treatment history
T1	Cooled from hot working and naturally aged (at room temperature)
T2	Cooled from hot working, cold-worked, and naturally aged
T3	Solution heat treated and cold worked
T4	Solution heat treated and naturally aged
T5	Cooled from hot working and artificially aged (at elevated temperature)
T6	Solution heat treated and artificially aged
T7	Solution heat treated and stabilized
T8	Solution heat treated, cold worked, and artificially aged
T9	Solution heat treated, artificially aged, and cold worked
T10	Cooled from hot working, cold-worked, and artificially aged

1.5 Objectives of the present thesis

There are four steps to make car body panels: cold-rolling, solution heat treatment, press-forming, and bake-hardening treatment (paint baking). Paint baking can be considered as aging, press-forming is the pre-deformation before aging. The aging behavior of Al-Mg-Cu alloys has been investigated, while the pre-deformation effect is still unclear. The general precipitation process has been introduced in the previous section, and it is known that GPB zones transform into two types of S phases during aging. However, the structure evolution of precipitates and precipitation process along dislocations have not been fully understood. The strength of Al alloys needs to be further improved to accelerate the lightweight process of automobiles.

The present thesis mainly studies the mechanical properties and microstructure of Al-Mg-Cu alloys processed by plastic deformation and aging heat treatment. Micro Vickers hardness measurement, tensile test, differential scanning calorimetry (DSC), scanning electron microscopy (SEM), transmission electron microscopy (TEM), density functional theory (DFT) calculation were applied for mechanical properties measurement and microstructure characterization.

The detailed aims of the present thesis are as follows:

1. To investigate the effect of pre-deformation on the age-hardening behavior of an Al-Mg-Cu alloy.

2. To understand precipitation sequences in the Al matrix and along dislocations to form S phases.

3. To reveal the structure evolutions from several GPB zones to two types of S phases during aging.

4. To study the cyclic strengthening phenomenon in an Al-Mg-Cu alloy and the aging behavior of cyclically deformed samples.

5. To achieve better mechanical properties by combining cyclic deformation and aging.

1.6 Outline of the present thesis

The outlines of each chapter are briefly summarized as follows:

Chapter 1 “General introduction”

This chapter introduces the basic knowledge of aluminum alloys, four major strengthening mechanisms, the aging behavior and precipitation of Al-Mg-Cu alloys, and several heat-treatment processes. Finally, the objective and construction of this thesis are presented.

Chapter 2 “Effect of pre-deformation on age-hardening behavior in an Al-Mg-Cu alloy”

The effects of 3%–50% cold rolling following solution heat treatment on the age hardening of an Al-3Mg-1Cu alloy have been studied in this chapter. The age-hardening behavior under RT, 393 K and 443 K of an Al-3Mg-1Cu alloy with reduction rates of 0%, 3%, 7%, 10%, 25%, and 50% are investigated by Vickers microhardness measurement at RT. Differential scanning calorimetry (DSC) is used to evaluate the effect of dislocations on the formation of clusters and S phases. High-angle annular dark-field scanning transmission electron microscopy (HAADF-STEM) technique is employed to investigate the precipitates formed under various conditions. Dissolution heat treatments are performed to determine and discuss the contribution of various precipitates to hardness under different aging durations. Tensile properties of base and 10% cold-rolled samples with various aging time were tested.

Chapter 3 “Precipitation processes and structural evolutions of various GPB zones and two types of S phases in a cold-rolled Al-Mg-Cu alloy”

The Guinier–Preston–Bagaryatsky (GPB) zone and the S phase are the key strengthening precipitates in Al-Cu-Mg alloys. However, how their respective structures evolve during aging has not been fully understood. In this work, the age-hardening behavior and the precipitates in an Al–3Mg–1Cu (wt.%) alloy were investigated. A novel type of GPB zone named “GPBX” was observed, and the crystal structure of S-II phases is determined. The precipitation process, structural evolution

and growth mechanisms of GPB zones and S phases are proposed. The structural similarity between GPB zones and precipitates in Al-Mg-Si alloys as well as the complex structure mixed of different types of precipitates are also confirmed.

Chapter 4 “Enhanced mechanical properties in an Al-Mg-Cu alloy processed by the combination of cyclic deformation and aging heat treatment”

Aging heat treatment is known as a traditional strengthening method for heat treatable Al alloys. Recently, cyclic strengthening has received widespread attention as a novel method. In this chapter, cyclic deformation was applied to introduce dislocations and promote cluster formation in an Al-Mg-Cu alloy. The cyclically strengthened (CS) samples were found to have both higher strength and ductility than the peak-aged samples. The cyclic strengthening effects in the Al-Mg-Cu alloy with pre-aging were also studied. The aging behaviors of cyclically strengthened samples with or without pre-aging were also investigated. Finally, aging and cyclic deformation methods were combined to maximize the effects of precipitation strengthening and work hardening.

Chapter 5 “General conclusions”

This chapter summarizes the main findings in the present work and presents general conclusions.

1.7 References

[1] M.E. Fine, Precipitation hardening of aluminum alloys, Metall. Trans. A. 6 (1975) 625–630. https://doi.org/10.1007/BF02672283.

[2] Kyoto protocol to the united nations framework convention on climate change, (1998). https://unfccc.int/resource/docs/convkp/kpeng.pdf (accessed September 29, 2021).

[3] J. Hirsch, Aluminium in Innovative Light-Weight Car Design, Mater. Trans. 52 (2011) 818–824. https://doi.org/10.2320/matertrans.L-MZ201132.

[4] W.S. Miller, L. Zhuang, J. Bottema, A.J. Wittebrood, P. De Smet, A. Haszler, A. Vieregge, Recent development in aluminium alloys for the automotive industry, Mater. Sci. Eng. A. 280 (2000) 37–49. https://doi.org/10.1016/S0921-5093(99)00653-X.

[5] M.E. Schlesinger, Aluminum Recycling, 2nd ed., CRC Press, Boca Raton, 2017.

[6] M. Abbadi, P. Hähner, A. Zeghloul, On the characteristics of Portevin - Le Chatelier bands in aluminum alloy 5182 under stress-controlled and strain-controlled tensile testing, Mater. Sci. Eng. A. 337 (2002) 194–201. https://doi.org/10.1016/S0921-5093(02)00036-9.

[7] W.F. Smith, J. Hashemi, F. Presuel-Moreno, Foundations of Materials Science and Engineering, 4th ed., Mcgraw-Hill Publishing, 2006. http://sutlib2.sut.ac.th/sut_contents/H97858.pdf.

[8] C.A. Schuh, T.G. Nieh, Hardness and abrasion resistance of nanocrystalline nickel alloys near the Hall-Petch breakdown regime, Mater. Res. Soc. Symp. - Proc. 740 (2002) 27–32. https://doi.org/10.1557/proc-740-i1.8.

[9] W. Soboyejo, Mechanical Properties of Engineered Materials, 1st ed., CRC Press, New York, 2002. https://doi.org/10.1201/9780203910399.

[10] S.P. Ringer, K. Hono, Microstructural evolution and age hardening in aluminium alloys: atom probe field-ion microscopy and transmission electron microscopy studies, Mater. Charact. 44 (2000) 101–131. https://doi.org/10.1016/S1044-5803(99)00051-0.

[11] U.F. Kocks, Laws for work-hardening and low-temperature creep, J. Eng. Mater. Technol. Trans. ASME. 98 (1976) 76–85. https://doi.org/10.1115/1.3443340.

[12] K. Yamada, T. Sato, A. Kamio, Cluster formation and two-step aging behaviors of Al-Mg-Si alloys, Keikinzoku/Journal Japan Inst. Light Met. 51 (2001) 215–221. https://doi.org/10.2464/jilm.51.215.

[13] M. Mihara, E. Kobayashi, T. Sato, Rapid age-hardening behavior of Al-Mg-Cu (-Ag) alloys and incubation stage in the low-temperature aging, Mater. Trans. 54 (2013) 1898–1904. https://doi.org/10.2320/matertrans.MAW201315.

[14] Y.A. Bagaryatsk, Structural changes on aging Al-Cu-Mg alloys, Dokl. Akad.

SSSR. 87 (1952).

[15] R.N. Wilson, P.G. Partridge, The nucleation and growth of S' precipitates in an aluminium-2.5% copper-1.2% magnesium alloy, Acta Metall. 13 (1965) 1321–1327. https://doi.org/10.1016/0001-6160(65)90043-X.

[16] L.F. Mondolfo, Aluminum alloys: structure and properties, Butterworths, London, 1976.

[17] S.P. Ringer, K. Hono, I.J. Polmear, T. Sakurai, Nucleation of precipitates in aged AlCuMg(Ag) alloys with high Cu:Mg ratios, Acta Mater. 44 (1996) 1883–1898. https://doi.org/10.1016/1359-6454(95)00314-2.

[18] S.P. Ringer, K. Hono, I.J. Polmear, T. Sakurai, Precipitation processes during the early stages of ageing in Al-Cu-Mg alloys, Appl. Surf. Sci. 94–95 (1996) 253–260. https://doi.org/10.1016/0169-4332(95)00383-5.

[19] S.P. Ringer, T. Sakurai, I.J. Polmear, Origins of hardening in aged Al-Cu-Mg-(Ag) alloys, Acta Mater. 45 (1997) 3731–3744. https://doi.org/10.1016/S1359-6454(97)00039-6.

[20] S.P. Ringer, S.K. Caraher, I.J. Polmear, cluster hardening in an aged Al-Cu-Mg alloy, Scr. Mater. 36 (1997) 517–521. https://doi.org/10.1016/S1359-6462(96)00415-0.

[21] P. Ratchev, B. Verlinden, P. De Smet, P. Van Houtte, Precipitation hardening of anAl–4.2wt% Mg–0.6wt% Cu alloy, Acta Mater. 46 (1998) 3523–3533. https://doi.org/10.1016/S1359-6454(98)00033-0.

[22] P. Ratchev, B. Verlinden, P. De Smet, P. Van Houtte, Artificial Ageing of Al-Mg-Cu Alloys, Mater. Trans. JIM. 40 (1999) 34–41. https://doi.org/10.2320/matertrans1989.40.34.

[23] A. Charai, T. Walther, C. Alfonso, A.M. Zahra, C.Y. Zahra, Coexistence of clusters, GPB zones, S″-, S′- and S-phases in an Al-0.9% Cu-1.4% Mg alloy, Acta Mater. 48 (2000) 2751–2764. https://doi.org/10.1016/S1359-6454(99)00422-X.

[24] C.B. Zhang, W. Sun, H.Q. Ye, Investigation of the crystallography and morphology of the s' precipitate in an Al(Cumg) alloy by hrem, Philos. Mag.

Lett. 59 (1989) 265–271. https://doi.org/10.1080/09500838908206354.

[25] V. Radmilovic, R. Kilaas, U. Dahmen, G.J. Shiflet, Structure and morphology of S-phase precipitates in aluminum, Acta Mater. 47 (1999) 3987–3997. https://doi.org/10.1016/S1359-6454(99)00259-1.

[26] S.C. Wang, M.J. Starink, Two types of S phase precipitates in Al-Cu-Mg alloys, Acta Mater. 55 (2007) 933–941. https://doi.org/10.1016/j.actamat.2006.09.015.

[27] Z. Feng, Y. Yang, B. Huang, M. Han, X. Luo, J. Ru, Precipitation process along dislocations in Al-Cu-Mg alloy during artificial aging, Mater. Sci. Eng. A. 528 (2010) 706–714. https://doi.org/10.1016/j.msea.2010.09.069.

[28] G. Sha, R.K.W. Marceau, X. Gao, B.C. Muddle, S.P. Ringer, Nanostructure of aluminium alloy 2024: Segregation, clustering and precipitation processes, Acta Mater. 59 (2011) 1659–1670. https://doi.org/10.1016/j.actamat.2010.11.033.

[29] M. Mihara, C.D. Marioara, S.J. Andersen, R. Holmestad, E. Kobayashi, T. Sato, Precipitation in an Al-Mg-Cu alloy and the effect of a low amount of Ag, Mater. Sci. Eng. A. 658 (2016) 91–98. https://doi.org/10.1016/j.msea.2016.01.087.

[30] A.K. Gupta, P. Gaunt, M.C. Chaturvedi, The crystallography and morphology of the S'-phase precipitate in an Al(CuMg) alloy, Philos. Mag. A Phys. Condens. Matter, Struct. Defects Mech. Prop. 55 (1987) 375–387. https://doi.org/10.1080/01418618708209875.

[31] L. Kovarik, Microstructural study and modeling of metastable phases and their effect on strenghthening in Al-Mg-Cu-Si alloying system, The Ohio State University, PhD Dissertation, 2006.

[32] Y. Komiya, S. Hirosawa, T. Sato, 3DAP nano-scale analysis of solute clusters formed in a naturally aged Al-Zn alloy, Keikinzoku/Journal Japan Inst. Light Met. 56 (2006) 662–666. https://doi.org/10.2464/jilm.56.662.

[33] J.M. Silcock, The structural ageing characteristics of Al-Cu-Mg alloys with copper-magnesium weight ratios of 7-1 and 2.2-1, J. Inst. Met. 89 (1961) 203–210.

[34] L. Reich, S.P. Ringer, K. Hono, Origin of the initial rapid age hardening in an Al-1.7 at.% Mg-1.1 at.% Cu alloy, Philos. Mag. Lett. 79 (1999) 639–648.

https://doi.org/10.1080/095008399176689.

[35] C.R. Hutchinson, S.P. Ringer, Precipitation processes in Al-Cu-Mg alloys microalloyed with Si, Metall. Mater. Trans. A Phys. Metall. Mater. Sci. 31 (2000) 2721–2733. https://doi.org/10.1007/BF02830331.

[36] C. Wolverton, Crystal structure and stability of complex precipitate phases in Al-Cu-Mg-(Si) and Al-Zn-Mg alloys, Acta Mater. 49 (2001) 3129–3142. https://doi.org/10.1016/S1359-6454(01)00229-4.

[37] L. Kovarik, P.I. Gouma, C. Kisielowski, S.A. Court, M.J. Mills, A HRTEM study of metastable phase formation in Al–Mg–Cu alloys during artificial aging, Acta Mater. 52 (2004) 2509–2520. https://doi.org/10.1016/j.actamat.2004.01.041.

[38] L. Kovarik, S.A. Court, H.L. Fraser, M.J. Mills, GPB zones and composite GPB/GPBII zones in Al–Cu–Mg alloys, Acta Mater. 56 (2008) 4804–4815. https://doi.org/10.1016/j.actamat.2008.05.042.

[39] L. Kovarik, M.J. Mills, Structural relationship between one-dimensional crystals of Guinier–Preston–Bagaryatsky zones in Al–Cu–Mg alloys, Scr. Mater. 64 (2011) 999–1002. https://doi.org/10.1016/j.scriptamat.2011.01.033.

[40] L. Kovarik, M.J. Mills, Ab initio analysis of Guinier-Preston-Bagaryatsky zone nucleation in Al-Cu-Mg alloys, Acta Mater. 60 (2012) 3861–3872. https://doi.org/10.1016/j.actamat.2012.03.044.

[41] H. Perlitz, A. Westgren, The crystal structure of Al2CuMg, Ark. Kemi Miner. Geol. 16B (1943) 13.

[42] R. Kilaas, V. Radmilovic, Structure determination and structure refinement of Al2CuMg precipitates by quantitative high-resolution electron microscopy, Ultramicroscopy. 88 (2001) 63–72. https://doi.org/10.1016/S0304-3991(00)00107-8.

[43] J. Majimel, G. Molenat, F. Danoix, O. Thuillier, D. Blavette, G. Lapasset, M.J. Casanove, High-resolution transmission electron microscopy and tomographic atom probe studies of the hardening precipitation in an Al-Cu-Mg alloy, Philos. Mag. 84 (2004) 3263–3280. https://doi.org/10.1080/14786430412331283983.

[44] C. Wolverton, V. Ozoliņš, First-principles aluminum database: Energetics of

binary Al alloys and compounds, Phys. Rev. B - Condens. Matter Mater. Phys. 73 (2006). https://doi.org/10.1103/PhysRevB.73.144104.

[45] Z.R. Liu, J.H. Chen, S.B. Wang, D.W. Yuan, M.J. Yin, C.L. Wu, The structure and the properties of S-phase in AlCuMg alloys, Acta Mater. 59 (2011) 7396–7405. https://doi.org/10.1016/j.actamat.2011.08.009.

[46] M. Mihara, E. Kobayashi, T. Sato, Nanocluster formation and two-step aging behavior of rapid hardening Al-Mg-Cu-(Ag) alloys, Mater. Sci. Forum. 794–796 (2014) 996–1001. https://doi.org/10.4028/www.scientific.net/MSF.794-796.996.

[47] 里達雄, 誰でもわかる技術, 日本鋳造工学会関東支部. 12 (2014).

[48] S. KIM, Composition Dependence of Nanocluster Characteristics in Natural- and Pre-aged Al-Mg-Si alloys Responsible for Two-step Aging Behavior, Tokyo Institute of Technology, Doctoral thesis, 2016. http://t2r2.star.titech.ac.jp/rrws/file/CTT100712455/ATD100000413/thesis_13D51066_SeongNyeong Kim.pdf.

[49] H. Möller, Optimisation of the heat treatment cycles of CSIR semi-solid metal processed Al-7Si-Mg alloys A356/7, University of Pretoria, Doctoral thesis, 2011.

[50] A.K. Dahle, Heat Treatment of Aluminium Alloys, Encycl. Mater. Sci. Technol. 3 (2001).

Chapter 2. Effect of pre-deformation on age-hardening behavior in an Al-Mg-Cu alloy

2.1 Introduction

Aluminum alloys with Cu and Mg as the main alloying elements are important lightweight structural materials for aerospace and automotive applications [1,2]. This is due to their superior mechanical properties developed by a complex heat treatment process that includes solution heat treatment (SHT) followed by aging heat treatment. SHT takes place at a temperature above the solvus line, where the solute elements dissolve in the Al lattice. Subsequent fast cooling to a low temperature, typically room temperature (RT), produces a supersaturated solid solution (SSSS) in which the alloying elements are bound to the Al face-centered cubic (FCC) lattice positions. The same applies to the vacancies: The high natural concentration of vacancies at the SHT temperature is quenched into the RT state. These quenched-in vacancies [3] mediate solute transport (diffusion) in the lattice and are responsible for the initial formation of solute clusters. They may also join to form low-energy vacancy orderings, such as dislocation loops [4]. After SHT, the alloy is heated to an intermediate temperature (approximately 443 K) in a process known as artificial aging (AA). This leads to precipitation, where the supersaturated and well-distributed Cu and Mg solute atoms are ordered into nanoscale precipitates that are partly coherent with the aluminum host matrix. The resulting chemical differences create obstacles for the movement of dislocations during deformation, which greatly increase the strength of the material. Depending on the temperature and holding time, the precipitates grow, dissolve, nucleate, and transform into new forms until the most stable phase is reached. The sequence of precipitation leading to the stable S phases can be summarized as [5–9]:

$$\text{SSSS} \rightarrow \text{Cu/Mg clusters} \rightarrow \text{GPB zones} \rightarrow \text{S phases} \quad (1)$$

Here, SSSS is the state in which the Al lattice is a supersaturated solid solution. Clusters are local aggregates of solute atoms and there are often vacancies at the Al positions in the FCC structure. The Guinier–Preston–Bagaryatsky (GPB) zones are considered as fine-scaled solute-enriched regions of longer order where both vacancies and interstitials can deviate from the host lattice. The S phases are equilibrium

precipitates with the composition Al_2CuMg, which are, in principle, stable phases that can exist independent of the Al.

Available literature rarely makes a clear distinction between the Cu/Mg clusters and GPB zones. We define GPB zones as those possessing a definite structure, whereas clusters do not have such a structure. Several types of GPB zones exist. Some of the examples of this system are the frequently reported $GPB^{(n)}$ zones [10–12], and GPB-T zones [13]. The S phase is related to S' and S'' [8,14,15]. The S'' phase is considered a GPB zone [8], while S', due to coherency, is a slightly strained version of the equilibrium S phase [14]. They are collectively denoted as S phases as their structures are similar, although with lattice parameters that can change during aging [14]. The S phases are also classified into two different categories based on their morphology and orientation relationship with the Al matrix: the $<012>_{Al}$ oriented lath-shaped S-I phase and the $<014>_{Al}$ orientated rod-shaped S-II phase [9,16–18].

Age-hardening behavior in Al-Cu-Mg alloys has been investigated by several groups [19–23]. A characteristic feature of these alloys is the rapid age-hardening phenomenon. This refers to an initial rapid increase in hardness during aging, which may be attributed to the formation of solute clusters [6,21–23] or GPB zones [10,12,24]. However, there are no unified interpretations. A second feature during aging is the presence of a hardness plateau after the initial increase, where the hardness remains constant for a long time. A second hardening stage occurred after the plateau ended at the peak hardness value. This is followed by the conventional over-aging stage, where the hardness decreases owing to the coarsening of precipitates and less coherency strain.

Although the conventional age-hardening behavior is well understood, materials (or components) sometimes need to undergo processing before heat treatment. For example, car body panel sheets are often press-formed before the paint is subjected to baking which involves the heat treatment (443 K for 20–30 min) of the sheets after painting, but without a solution heat treatment in between. This implies that the precipitation takes place in a deformed material. Therefore, the pre-deformation has a significant effect on subsequent precipitation heat treatment. It has been investigated in Al-Cu alloys [25,26], but Al-Mg-Cu alloys with high Mg/Cu ratios have not been the subject of wide study.

In this work, cold rolling (CR) of the Al-Mg-Cu alloy is performed before aging to investigate the effect of pre-deformation on the aging behavior. Considering that the local deformation of the different parts may be different during the press-forming process, a wide range of reduction rates (from 3 to 50%) were selected. This ensures that the obtained results have a broader range, which is significant for both shape and process design. The microstructure and mechanical properties of the pre-deformed aged sample are reported and discussed. In addition, the hardness contributions of the GPB zones and S phases under various conditions are evaluated.

2.2 Experimental methods

Table 2.1 lists the chemical composition of the high-purity Al-3Mg-1Cu alloy used in this study. The heat treatment and cold rolling processes are illustrated in Fig. 2.1(a) and (b), respectively. Samples of size 10 × 10 × 1.2 mm^3 were solution heat-treated in a salt bath at 793 K for 1 h, followed by quenching in iced water, where it was held for 1 min. The quenched samples were subsequently cold-rolled at RT at reduction rates of 0%, 3%, 7%, 10%, 25%, and 50%. The rolling ratio was determined by measuring the reduction in sheet thickness. Isothermal aging was carried out in oil baths at RT, 393 K, and 443 K for the selected holding times. The as-quenched and as-rolled conditions are abbreviated as “AQ” and “AR,” respectively. The samples with and without pre-deformation are called “base” and “CR” samples, respectively. Dissolution heat treatment was performed in salt baths for 2 min at the corresponding dissolution peak temperatures of GPB zones to determine the contribution of the precipitates to hardness.

The micro-Vickers hardness was measured at RT by applying a load of 200 g for 15 s in a Matsuzawa MMT-X micro-hardness tester. Every reported hardness value is the average of five out of a set of seven hardness data points (excluding the two extremal values).

Differential scanning calorimetry (DSC) tests were carried out in an argon atmosphere in a Rigaku DSC8230 instrument using 40 mg of pure Al (99.99 %) as a reference, at a heating rate of 10 K/min. The temperature range for the DSC measurements (223–773 K) was monitored using a liquid nitrogen controller.

The samples were cold-rolled and aged prior to the tensile tests, from which flat dog-bone test specimens, as shown in Fig. 2.1(c), were cut out. For the tensile

experiments, an Autograph AG-X plus tester manufactured by Shimadzu was used. The tests were conducted at RT at a strain rate of 6.07×10^{-4} s^{-1}. Three tensile specimens were tested for each condition and the results were found to be reproducible.

The tensile direction is parallel to the rolling direction. The fracture surfaces of the tensile-tested samples were observed using a field emission scanning electron microscope (FE-SEM, JEOL JSM-7200F) operated at 15 kV.

Specimens for transmission electron microscopy (TEM) were prepared from 1.2 mm sheet samples. They were reduced by grinding the samples into foils with a thickness of ~ 100 μm. Discs of 3 mm diameter were punched from the resulting foils and further electropolished to perforation using a Struers TenuPol-5. The electrolyte (1/3 nitric acid and 2/3 methanol) was maintained between 243 K and 253 K during electropolishing, with an applied potential of 20 V.

The microstructure of precipitate was investigated by high-resolution, high-angle annular dark-field scanning TEM (HAADF-STEM) in a double Cs-corrected JEOL ARM 200CF STEM operated at 200 kV. The convergence semi-angle was set to 28 mrad, and the inner collection angle of the HAADF detector was 48 mrad. To reduce contamination, all specimens were treated for 3 min in a Fischione 1020 Plasma Cleaner prior to the TEM observations. All the presented images are along the <100>Al orientation. This is because all the precipitates are elongated along the <100>Al direction and extend mostly through the TEM specimen in the thin regions investigated, enabling good contrast.

The column contrast in the images was further enhanced by a circular bandpass mask applied to the respective fast Fourier transform (FFT), which corresponds to the removal of high spatial frequencies (noise) in the real space below 0.15 nm. An inverse FFT (IFFT) was performed on the masked area.

The HAADF-STEM technique utilizes the Z contrast arising from Rutherford scattering from the core electrons of atoms. In column-resolved images, a column having a larger average atomic number Z will have more scattering, which results in a greater brightness in the STEM image [27].

2.3 Results and discussion

2.3.1 Age-hardening behavior

I. Age-hardening at 443 K

Fig. 2.2(a) shows the hardness response for aging of the investigated alloy by different treatments at 443 K. The (undeformed) base material reveals a standard four-stage change in hardness, namely a rapid initial increase, plateau, second increase to maximum hardness, and final decrease. Rapid age-hardening (R1) from 66.4 to 88.9 HV occurs within the first 60 s, followed by a plateau stage (L) that lasts for approximately 1 day. After aging for 7 to 14 days, the hardness increases again (R2) to a maximum with a peak hardness of approximately 101.0 HV. The last stage (D) is characterized by a decrease in hardness due to over-aging. It should be mentioned that R1 contributes to approximately 65% of the total increase in hardness.

The curves show that cold rolling delays the first increase in hardness, R1. Deformation effectively adds an initial incubation stage. Although more deformation generally leads to higher hardness, the two lower curves in Fig. 2.2(a) show that for a brief period during aging, where R1 and L meet, the delay in precipitation of the 3% CR sample results in a hardness below that of the base sample. For the 3% CR sample, R1 increases from 1 to 20 min, finally reaching a plateau level (L) above that of the base, but it starts later and ends sooner. Then, it reached a broad peak that lasted up to 1 month, after aging for 24 h. The deformation reduces the aging time for maximum hardness by a factor of approximately 10.

The curves show that the increased deformation of up to 50% shows similar age-hardening behavior and consistently higher hardness. Higher reduction rates indicated faster precipitation. Evidence of recovery behavior is obvious at the early stage for the two upper curves corresponding to the 25% and 50% CR samples. Compared with the base sample, the hardness plateaus L (and the first hardening stage R1) in samples with small reduction rates (3 to 10%) were delayed initially, but recovered again as the reduction rate increased (25 and 50%). This is discussed further in section 2.3.2-II. The vertical dotted line indicates the bake-hardening condition. At the position where this line intersects the curves, we see that the hardness is increased from 90.6 to 119.7 HV when 50% cold-rolling is applied.

II. Age-hardening at 393 K and room temperature

Artificial aging is typically performed at a temperature of 443K. However, it is important to understand aging behavior in a more general sense because precipitation depends strongly on temperature. During production, the processing steps are often separated by RT storage, also called “natural aging” (NA). Such low-temperature steps in the process often affect the precipitation. For example, different clusters have been observed to form preferentially at RT and 373 K in Al-Mg-Si alloys [28]. In this work, the age-hardening of the Al-Mg-Cu alloy at 293 K (RT) and 393 K was investigated.

The age-hardening curves for the base, 10%, and 25% CR samples aged at 393 K and RT are shown in Fig. 2.2 (b) and (c), respectively. For the base alloy aged at 393 K, the initial incubation stage appears before the first hardening increases the R1. The 10% and 25% CR samples behave similarly to the base; however, as their kinetics are slower, they require a longer aging time to reach plateau L. The right-hand side of the curves in Fig. 2.2(b) shows all three samples at the L-stage after aging at 393 K for 14 days. This can be compared to 443 K in Fig. 2.2(a), where 14 days would allow all of them to reach the peak or the overaged stage D. As expected, Fig. 2.2(c) shows much slower kinetics at RT: even after 2 years of aging, the three samples remained on the plateau. The similarity in the overall aging curve shape indicates that the same mechanisms are at play, but that the activity increases with temperature.

The main issue that curtails the large-scale application of Al alloys to automobile body panels is the requirement of long-term usage at high service temperatures (such as due to exposure to sunlight). This leads to over-aging, decreased strength, and reduced service life. The long aging time required to reach the peak hardness for the investigated Al-Mg-Cu alloy indicates good thermal stability, which can potentially address this concern.

2.3.2 DSC results

I. DSC of the base material for various aging times

Fig. 2.3(a) shows the DSC curves of the base alloy aged at 443 K for different durations. For the AQ sample, two exothermic peaks appear at 376.3 K (I) and 567.7 K (III). They signify the formation of clusters [29] and S phases [30], respectively. The exothermic peak II, expected to accompany the formation of GPB zones, was absent. The endothermic negative peaks (dips) I’ and II’ are attributed to the dissolution of the

clusters and GPB zones, respectively [31], while the endothermic peak III' represents the dissolution of the S phase.

Peak I disappears after short-term aging at 443 K, indicating that clusters have been formed and are responsible for rapid age-hardening. After aging for 12 days, peak III was strongly reduced, suggesting the formation of the S phase. Peak I' almost disappeared while peak II' still exists, indicating that the clusters have been dissolved and there are still GPB zones remaining to be dissolved in order to form S phases.

The exothermic peak IV is likely to correspond to a precipitate phase other than the S phase, which may form at temperatures above 443 K. It disappears after a short time, which is insufficient to form a precipitate. This peak is not considered in the further examination.

II. DSC of the as-quenched and as-rolled samples

The DSC curves of the AQ and AR alloys at different reduction rates are shown in Fig. 2.3(b). The cluster formation peak I is absent in the AR samples, indicating that the clusters have already been formed, or that they will not form during subsequent aging. The absence of a cluster dissolution peak I' in the AR samples supports the second option, because this means that there are no clusters to dissolve. This is because the dislocations introduced in the CR samples act as vacancy sinks, reducing the fraction of vacancies available for the formation of clusters [32]. This is consistent with the hardness curves of the CR samples without a rapid initial increase in hardness.

We assume that the broad and weak peak II is attributed to the GPB zone formation in the CR samples. The presence of GPB zones is also indicated by the subsequent dissolution peak II'. The temperature related to peak III decreased (567.7 K to 535.8 K) with an increased reduction rate (0 to 25%), indicating that the presence of dislocations may accelerate the formation of the S phase. This is consistent with the hardness curve: the higher the reduction rate, the shorter the time required to reach the peak hardness.

The age-hardening behavior of the base and CR materials are dominated by different mechanisms. In the base sample, the quenched-in vacancies dominated the diffusion of the solute atoms. This leads to homogenous solute clusters that are responsible for rapid age-hardening. In the CR samples, the deformation-induced dislocations hindered the formation of clusters, but promoted precipitation on the dislocations. We suggest that this is the reason for the initial hardening stage R1. With more deformation, the

dislocations increasingly dominate the diffusion, which results in an accelerated R1 stage as well as a shorter hardness plateau L.

III. DSC of 7% cold-rolled samples as a function of aging time

The DSC curves of the 7% CR samples aged at 443 K for different durations are shown in Fig. 2.3(c). The DSC curve did not change after aging for 1 min, corresponding to the first incubation stage in the age-hardening behavior. The GPB zone formation peak II nearly disappeared after aging for 20 min, indicating that the GPB zones had already formed. Both the GPB zone dissolution peak II' and the S phase formation peak III become smaller in the CR samples aged for 1 day, which suggests that a portion of the GPB zones is consumed by the S phases. Only peak III' remained after aging for 7 days. This suggests that the GPB zones do not exist anymore, and the precipitation of the S phases is completed.

2.3.3 Microstructural characterization

I. Microstructure in base samples

Fig. 2.4 (a) and (b) show the HAADF-STEM images of the base samples aged at 443 K for 1 min and 8 h, respectively. The matrix in the sample aged for 1 min contains a high density of small regions of higher contrast (some regions are circled in Fig.4(a) as examples). This indicates a greater number of clusters. In addition, as indicated by the arrows, some clusters form GPB zones. They grow as short needle-like structures along the <100>Al direction, therefore only the ones viewed in the cross-section have sufficient Cu in the atomic columns to show strong contrast. GPB zones viewed perpendicular to their lengths would contain fewer Cu atoms along the atomic columns and overlap more with the Al matrix. The zones are mostly double eye-like units connected by a distance a_{Al}<210>/2 on a dislocation line [8–10]. This shows that the clusters and GPB zones are responsible for the initial age hardening.

Fig. 2.4(b) presents an image of the 8 h sample. Here, two S-I plate-shaped precipitates with traces along the <210> Al direction, as visualized by their double Cu layers, have a GPB zone in the middle. This indicates that they were nucleated from the GPB zone. This signifies an S-phase formation that is faster than expected, which corresponds to the plateau stage that represents the "incubation period" for S phase formation [21]. The plates had the smallest possible thickness, indicating a recent formation. This shows that the formation of the S phases can occur before the second

hardening stage. This is discussed in Section 2.3.4, in relation to the dissolution experiments.

II. Microstructure of cold-rolled samples

Fig. 2.5 shows the typical HAADF-STEM images of the 7% CR samples after aging for 20 min (a) and 1 day (b-c) at 443 K. After 20 min, the normal GPB zones and GPBX zones (will be introduced in detail in next chapter), together with thin plates of the S-I phase, formed a continuous band on a dislocation. Normal GPB zones can grow and transform into S-I phases, while the GPBX zones transform into S-II phases upon further aging [9]. This can explain the observation in Fig. 2.5(b) after aging for 1 day: that two types of S phase predominantly form on the dislocations. The intergrowth of S phases shown in Fig. 2.5(c) can be explained if the nuclei (normal GPB or GPBX zones) are present on a suitable dislocation line at suitable distances. Evidence of a high density of dislocation lines and loops can be found in the overview of S phases on the dislocations in Figs. S2.1 and S2.2 in Supplementary Material. No precipitates were observed in the AR samples [33].

Combining the results of the hardening curves (Fig. 2.2(a)), DSC curves (Fig. 2.3(c)), and TEM analysis (Fig. 2.5), we conclude that the two hardening stages R1 and R2 in the CR samples correlate with the presence of GPB zones and S phases, respectively.

2.3.4 Contribution of precipitates to hardness

As mentioned in the previous section, the S phases were found in both the base sample aged for 8 h and the 7% CR sample aged for 20 min at 443 K. However, this may seem inconsistent with the hardening responses. There has been disagreement about whether the GPB zone [23], S phase [30] or a combination [7] are responsible for the peak hardness condition. To elucidate the matter, dissolution experiments for different aging times were performed to evaluate the actual contribution of the GPB zones and S phases to the hardness, for both the base and CR samples.

The samples were heat-treated in a salt bath at each dissolution peak temperature of GPB zones (531 K, 520 K, 516 K, and 510 K in base, 3%, 7%, and 25% CR samples, respectively) for 2 min to achieve complete dissolution. The hardness reached the maximum value at 2 min of heat treatment and remained almost constant even with further heat treatment. As the dissolution peaks of both the clusters and GPB zones are

close to each other, it is difficult to separate them while maintaining accuracy. Both two types of S phases are collectively referred to as S phases because they have the same formation and dissolution peaks and cannot be separated. The loss of hardness after dissolution can be understood as the combined contribution from the clusters and GPB zones. The contribution of S phases to the hardness was obtained by subtracting the contribution of the clusters/GPB zones from the total increase in hardness during aging. The original contribution of the dislocations was determined by the hardness difference before and after cold rolling. The change in the contribution during aging is estimated by referring to the initial stage of age-hardening behavior where no precipitation is formed, and it is assumed that there is no change in the subsequent aging. Therefore, the real drop in hardness due to recovery should be slightly higher than the estimated value. It should also be pointed out that because many S phases are formed along the dislocations, in addition to the individual contribution of the precipitates and the dislocation to the hardness, the interaction between the S phases and the dislocations can also increase the hardness. The contribution of the S phase/dislocation interaction is not shown in the figure because it is difficult to quantify accurately. The interaction can also stabilize the S phases and dislocations, resulting in fewer dislocations being recovered during aging. In this chapter, the contributions of the clusters/GPB zones, S phases, and dislocations to the hardness are discussed.

I. Contribution of precipitates to hardness in the base alloy

The age-hardening responses of the base samples before (black line) and after (green line) the dissolution heat treatment are shown in Fig. 2.6(a). The red and blue areas represent the contribution of the clusters/GPB zones and S phases to hardness, respectively, with the values summarized in Table 2.2. It was found that the increase in hardness in the initial stage of aging was caused entirely by clusters/GPB zones; however, the GPB zones start to dissolve and transform to S phases so that the cluster/GPB zone contribution begins to decrease. The newly nucleated S phase is still small (see Fig. 2.4(b)) and not significantly different from the GPB zones. Therefore, the dissolved GPB zones and initial small S phases lead to a dynamic balance of the total hardness during the later period of the plateau, which also explains the presence of S phases in the base sample aged for 8 h. With further aging, the S phases begin to grow and increase the hardness until it reaches the peak value where the clusters/GPB zones and S phases contribute to approximately 40% and 60% of the total increase in

hardness, respectively. In the over-aging stage, the coarsening of the S phases finally results in a decrease in hardness, while the clusters/GPB zones still almost maintain a certain contribution to the hardness.

II. Contribution of precipitates to hardness in cold rolled alloys

The hardness contribution of the dislocations, clusters/GPB zones, and S phases in the base and CR samples aged at 443 K for various times are shown in Fig. 2.6(b). The white and orange areas in Fig. 2.6(b) represent the intrinsic hardness and the contribution from dislocations, respectively. Note that the red areas in the CR samples are mainly from the GPB zones because almost no clusters are formed during aging, as discussed earlier in section 2.3.2-II.

We assume that the contribution of the dislocation to hardness does not change during aging in the 3% and 7% CR samples, because no visible recovery is found in their aging responses, as shown in Fig. 2.2(a). In the 3% CR samples, only the GPB zones were formed after aging for 20 min, while both the GPB zones and S phases coexist in the peak-aged condition. Then, the GPB zones dissolve completely and transform into S phases with further aging. A similar phenomenon was observed in the 7% CR samples, but the S phases were formed after 20 min of aging and contributed more to the peak hardness. Recovery occurred in 25% CR samples. Because dislocation annihilation is significant at the beginning of aging and then weakens to a negligible level, we assume that the contribution of dislocations decreases during the first 20 min, where it tends to stabilize at a certain value. During the aging process, the GPB and S phases coexist at 20 min, and the GPB zones are completely transformed into S phases after 1 day. It was found that the higher the reduction rates, the earlier the S phases were formed. This indicates that dislocations can accelerate the formation of S phases. At the same time, the coarsening stages also advanced due to the dislocations. It is realized that the S phase contribution is lower in the largely deformed samples aged for 7 days, while the high hardness in heavily deformed samples is mainly attributed to the dislocations or the interaction between dislocations and precipitates.

2.3.5 Tensile test results and fracture surface observations

I. Tensile properties of the base and CR samples

The stress-strain curves of the base and CR samples aged at 443 K for various times are shown in Fig. 2.7(a). Their elongation to failure and ultimate tensile stress (UTS) are summarized in Fig. 2.7(b).

The AQ sample had the lowest yield strength (YS) and UTS, but the highest elongation rate. After 20 min of aging, both the YS and UTS increased significantly while the elongation decreased only slightly, owing to the formation of small and uniform clusters/GPB zones. For the sample aged for 12 days, which corresponds to the peak condition, most GPB zones will have transformed into S phases, resulting in a significant drop in the elongation rate, while the strength is further improved.

After 10% cold rolling was applied, the elongation rate decreased, but YS and UTS increased because of the work hardening effect. The 20 min aged CR sample shows an enhanced strength-plasticity combination (the same YS but both higher UTS and elongation rate) compared to the AR sample, which can be attributed to two reasons: first, a fraction of the dislocations are annihilated during the aging process, causing higher plasticity and greater work hardening tendency (it exhibits a higher increment of stress per strain than the AR sample); second, besides the annihilation of dislocations, solute atoms preferentially accumulate on the remaining dislocations to form GPB zones, a phenomenon which is responsible for the higher strength. With further aging of up to 7 days, the reduction in dislocation density is no longer obvious, and S phases will be formed. The S phases hinder the motion of dislocations, leading to shorter elongation but higher strength.

II. Fracture surfaces of the base and CR samples

The fracture surfaces of the base and CR samples aged at 443 K for different times are shown in Fig. 2.8. The fracture surfaces were consistent with the tensile test results. The fracture surfaces of both (a) AQ and (b) 20 min aged base sample contained a large amount of large and deep dimples, which are common in ductile fracture. The fracture surface of (c) the 12 day-aged base sample shows a quasi-cleavage fracture with some dimples, which indicates a more brittle failure mechanism and is consistent with the reduced elongation rate.

The fracture surface of (d) the AR sample shows a quasi-cleavage fracture with only a few dimples, and there are more dimples observed in (e) the 20 min aged CR sample. This indicates that the 20 min aged CR sample has better plasticity than the AR sample. The fracture surface of (f) the 7 days aged CR sample is a typical quasi-cleavage fracture, which means it is the most brittle sample.

2.4 Conclusions

The age-hardening behavior of Al-Mg-Cu alloy, aged with and without pre-deformation in the form of cold rolling, were investigated using hardness measurements, DSC, TEM, tensile testing, and fracture surface observations.

1. Rapid age hardening of the base alloy is absent in CR alloys. Instead, recovery was observed in the highly pre-deformed samples. The hardness peak advances with the increasing reduction rate. Aging at low temperatures delays the age-hardening behavior without changing the precipitation mechanism.

2. The near-absence of a cluster formation peak in the DSC curves of the CR alloys indicates that dislocations hinder the formation of clusters. The S phase formation peaks in the DSC curves of the CR alloys appeared at lower temperatures, indicating that dislocations accelerated the formation of S phases.

3. The first increase in hardness in the CR alloys is attributed to the GPB zones because both normal GPB zones and the GPBX zone were observed in the 20 min aged CR samples. Two types of S phases were detected in the CR samples aged for 1 day, suggesting that the second increase in hardness was caused by the S phase formation.

4. The S phases were formed in the later stages of the hardness plateau. The hardness is dynamically balanced by the dissolution of clusters/GPB zones and the formation of S phases.

5. The peak hardness in the base alloy is a combined result of clusters/GPB zones and S phases, and clusters/GPB zones are still stable even after long-term aging. However, the contribution of GPB zones was lower in the CR alloys, and all of them will transform into S phases after long-term aging.

6. When paint-baking (443 K for 20 min) was performed on the as-rolled samples, both the plasticity and strength increased because of the annihilation of dislocations and the formation of GPB zones.

2.5 References

[1] J.C. Williams, E.A. Starke, Progress in structural materials for aerospace systems, Acta Mater. 51 (2003) 5775–5799. https://doi.org/10.1016/j.actamat.2003.08.023.

[2] I.J. Polmear, Light Alloys: from Traditional Alloys to Nanocrystals, Butterworth-Heinemann/Elsevier, Oxford, 2006.

[3] T. Federighi, Quenched-in vacancies and rate of formation of zones in aluminum alloys, Acta Metall. 6 (1958) 379–381. https://doi.org/10.1016/0001-6160(58)90078-6.

[4] P.B. Hirsch, J. Silcox, R.E. Smallman, K.H. Westmacott, Dislocation loops in quenched aluminium, Philos. Mag. 3 (1958) 897–908. https://doi.org/10.1080/14786435808237028.

[5] Y.A. Bagaryatsk, Structural changes on aging Al-Cu-Mg alloys, Dokl. Akad. SSSR. 87 (1952).

[6] A. Charai, T. Walther, C. Alfonso, A.M. Zahra, C.Y. Zahra, Coexistence of clusters, GPB zones, S″-, S′- and S-phases in an Al-0.9% Cu-1.4% Mg alloy, Acta Mater. 48 (2000) 2751–2764. https://doi.org/10.1016/S1359-6454(99)00422-X.

[7] G. Sha, R.K.W. Marceau, X. Gao, B.C. Muddle, S.P. Ringer, Nanostructure of aluminium alloy 2024: Segregation, clustering and precipitation processes, Acta Mater. 59 (2011) 1659–1670. https://doi.org/10.1016/j.actamat.2010.11.033.

[8] M. Mihara, C.D. Marioara, S.J. Andersen, R. Holmestad, E. Kobayashi, T. Sato, Precipitation in an Al-Mg-Cu alloy and the effect of a low amount of Ag, Mater. Sci. Eng. A. 658 (2016) 91–98. https://doi.org/10.1016/j.msea.2016.01.087.

[9] X. Chen, C.D. Marioara, S.J. Andersen, J. Friis, A. Lervik, R. Holmestad, E. Kobayashi, Precipitation processes and structural evolutions of various GPB zones and two types of S phases in a cold-rolled Al-Mg-Cu alloy, Mater. Des.

199 (2021) 109425. https://doi.org/10.1016/j.matdes.2020.109425.

[10] L. Kovarik, S.A. Court, H.L. Fraser, M.J. Mills, GPB zones and composite GPB/GPBII zones in Al–Cu–Mg alloys, Acta Mater. 56 (2008) 4804–4815. https://doi.org/10.1016/j.actamat.2008.05.042.

[11] L. Kovarik, M.J. Mills, Structural relationship between one-dimensional crystals of Guinier–Preston–Bagaryatsky zones in Al–Cu–Mg alloys, Scr. Mater. 64 (2011) 999–1002. https://doi.org/10.1016/j.scriptamat.2011.01.033.

[12] L. Kovarik, M.J. Mills, Ab initio analysis of Guinier-Preston-Bagaryatsky zone nucleation in Al-Cu-Mg alloys, Acta Mater. 60 (2012) 3861–3872. https://doi.org/10.1016/j.actamat.2012.03.044.

[13] S.B. Wang, Z.R. Liu, S.L. Xia, J. Key, J.H. Chen, Tetragonal-prism-like Guinier–Preston–Bagaryatsky zones in an AlCuMg alloy, Mater. Charact. 132 (2017) 139–144. https://doi.org/10.1016/j.matchar.2017.08.014.

[14] A.K. Gupta, P. Gaunt, M.C. Chaturvedi, The crystallography and morphology of the S'-phase precipitate in an Al(CuMg) alloy, Philos. Mag. A Phys. Condens. Matter, Struct. Defects Mech. Prop. 55 (1987) 375–387. https://doi.org/10.1080/01418618708209875.

[15] F.J. Niu, J.H. Chen, S.Y. Duan, W.Q. Ming, J.B. Lu, C.L. Wu, Z. Le, The effect of pre-deformation on the precipitation behavior of AlCuMg(Si) alloys with low Cu/Mg ratios, J. Alloys Compd. 823 (2020). https://doi.org/10.1016/j.jallcom.2020.153831.

[16] V. Radmilovic, R. Kilaas, U. Dahmen, G.J. Shiflet, Structure and morphology of S-phase precipitates in aluminum, Acta Mater. 47 (1999) 3987–3997. https://doi.org/10.1016/S1359-6454(99)00259-1.

[17] S.C. Wang, M.J. Starink, Two types of S phase precipitates in Al-Cu-Mg alloys, Acta Mater. 55 (2007) 933–941. https://doi.org/10.1016/j.actamat.2006.09.015.

[18] M.J. Styles, C.R. Hutchinson, Y. Chen, A. Deschamps, T.J. Bastow, The coexistence of two S (Al 2CuMg) phases in Al-Cu-Mg alloys, Acta Mater. 60 (2012) 6940–6951. https://doi.org/10.1016/j.actamat.2012.08.044.

[19] P. Ratchev, B. Verlinden, P. De Smet, P. Van Houtte, Precipitation hardening of

anAl–4.2wt% Mg–0.6wt% Cu alloy, Acta Mater. 46 (1998) 3523–3533. https://doi.org/10.1016/S1359-6454(98)00033-0.

[20] P. Ratchev, B. Verlinden, P. De Smet, P. Van Houtte, Artificial Ageing of Al-Mg-Cu Alloys, Mater. Trans. JIM. 40 (1999) 34–41. https://doi.org/10.2320/matertrans1989.40.34.

[21] M. Mihara, E. Kobayashi, T. Sato, Rapid Age-Hardening Behavior of Al-Mg-Cu(-Ag) Alloys and Incubation Stage in the Low-Temperature Aging, Mater. Trans. 54 (2013) 1898–1904. https://doi.org/10.2320/matertrans.MAW201315.

[22] S.P. Ringer, S.K. Caraher, I.J. Polmear, cluster hardening in an aged Al-Cu-Mg alloy, Scr. Mater. 36 (1997) 517–521. https://doi.org/10.1016/S1359-6462(96)00415-0.

[23] S.P. Ringer, T. Sakurai, I.J. Polmear, Origins of hardening in aged Al-Cu-Mg-(Ag) alloys, Acta Mater. 45 (1997) 3731–3744. https://doi.org/10.1016/S1359-6454(97)00039-6.

[24] A.-M. Zahra, C.Y. Zahra, B. Verlinden, Comments on “Room-temperature precipitation in quenched Al–Cu–Mg alloys: a model for the reaction kinetics and yield-strength development,” Philos. Mag. Lett. 86 (2006) 235–242. https://doi.org/10.1080/09500830600678854.

[25] R.K. Gupta, R. Panda, A.K. Mukhopadhyay, V.A. Kumar, P. Sankaravelayutham, K.M. George, Studies on Thermo-mechanical Treatment of Al alloy AA2219, Met. Sci. Heat Treat. 57 (2015) 350–353. https://doi.org/10.1007/s11041-015-9888-0.

[26] A.K. Mukhopadhyay, R.K. Gupta, K.S. Prasad, P. Sankaravelayutham, Evolution of Tensile Properties in AA2219 Plates Due to Varying Modes and Percentages of Cold Work before Artificial Aging, J. Mater. Eng. Perform. 29 (2020) 5314–5321. https://doi.org/10.1007/s11665-020-04974-9.

[27] M.M.J. Treacy, Z dependence of electron scattering by single atoms into annular dark-field detectors, Microsc. Microanal. 17 (2011) 847–858. https://doi.org/10.1017/S1431927611012074.

[28] A. Serizawa, S. Hirosawa, T. Sato, Three-Dimensional Atom Probe Characterization of Nanoclusters Responsible for Multistep Aging Behavior of

an Al-Mg-Si Alloy, Metall. Mater. Trans. A. 39 (2008) 243–251. https://doi.org/10.1007/s11661-007-9438-5.

[29] M. Mihara, E. Kobayashi, T. Sato, Effect of trace addition of ag on the precipitation behavior of Al-Mg-Cu alloy, Eng. J. 19 (2015) 75–84. https://doi.org/10.4186/ej.2015.19.3.75.

[30] S.C. Wang, M.J. Starink, N. Gao, Precipitation hardening in Al–Cu–Mg alloys revisited, Scr. Mater. 54 (2006) 287–291. https://doi.org/10.1016/j.scriptamat.2005.09.010.

[31] V.A. Esin, L. Briez, M. Sennour, A. Köster, E. Gratiot, J. Crépin, Precipitation-hardness map for Al–Cu–Mg alloy (AA2024-T3), J. Alloys Compd. 854 (2021) 157164. https://doi.org/10.1016/j.jallcom.2020.157164.

[32] T.S. Parel, S.C. Wang, M.J. Starink, Hardening of an Al-Cu-Mg alloy containing Types I and II S phase precipitates, Mater. Des. 31 (2010) S2–S5. https://doi.org/10.1016/j.matdes.2009.12.048.

[33] X. Chen, C.D. Marioara, S.J. Andersen, J. Friis, A. Lervik, R. Holmestad, E. Kobayashi, Data on atomic structures of precipitates in an Al-Mg-Cu alloy studied by high resolution transmission electron microscopy and first-principles calculations, Data Br. 34 (2021) 106748. https://doi.org/10.1016/j.dib.2021.106748.

Table 2.1

Chemical composition of the investigated Al alloy in wt.% and at.%.

Element	Mg	Cu	Si	Fe	Al
wt.%	3.04	1.01	0.01	0.01	Bal.
at.%	3.38	0.43	0.01	0.005	Bal.

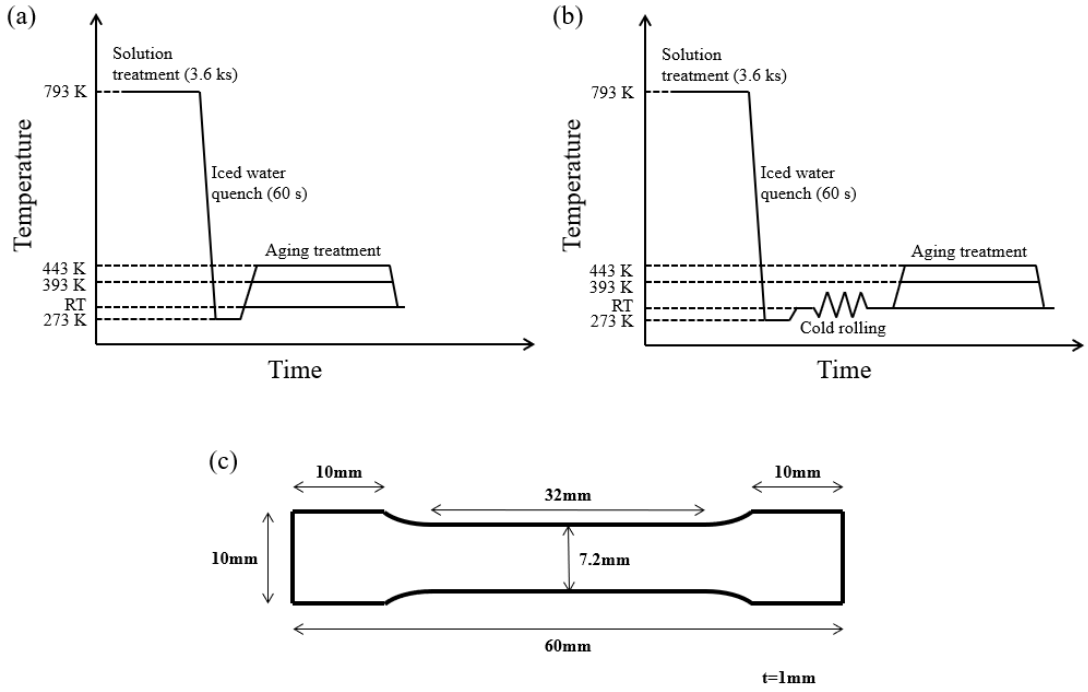

Fig. 2.1. Schematic of the heat treatment process with (a) standard procedure (no deformation) and (b) pre-deformation. (c) Sample geometry for tensile tests.

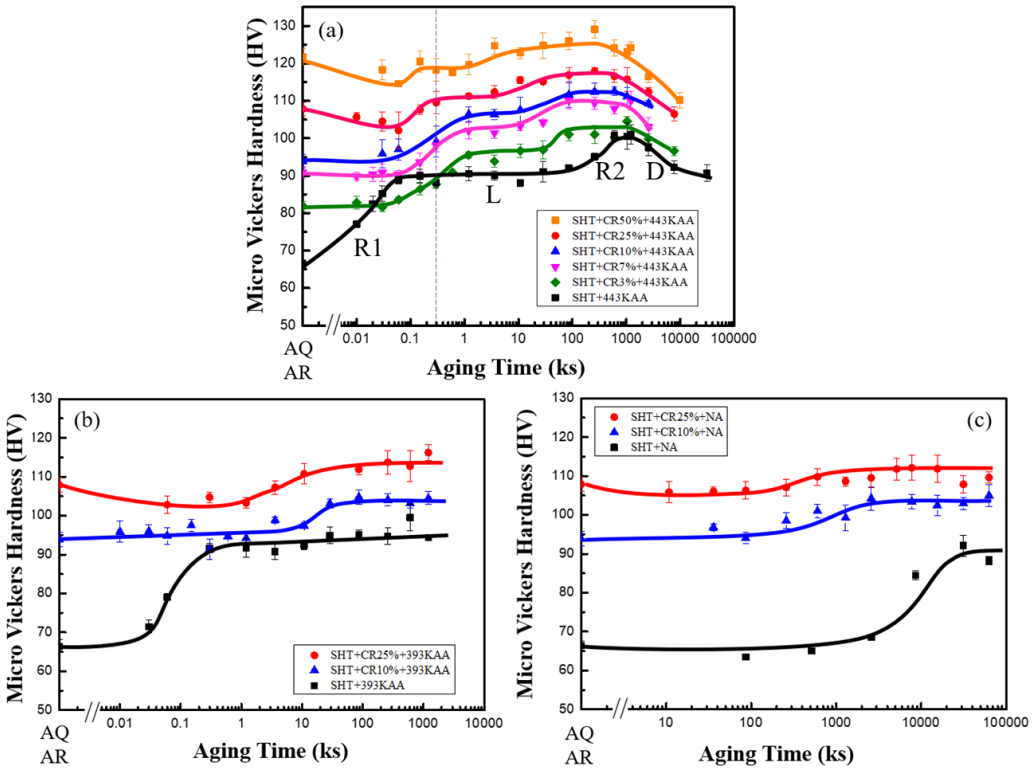

Fig. 2.2 Age-hardening behavior of the Al-3Mg-1Cu alloy at temperatures (a) 443 K, (b) 393 K, and (c) room temperature (293 K), for various reduction rates. The typical stages in the as-quenched sample are named first rise (R1), plateau level (L), second rise (R2), and decline (D). The labelling indicates the SHT time, CR reduction rate, and subsequent aging temperatures.

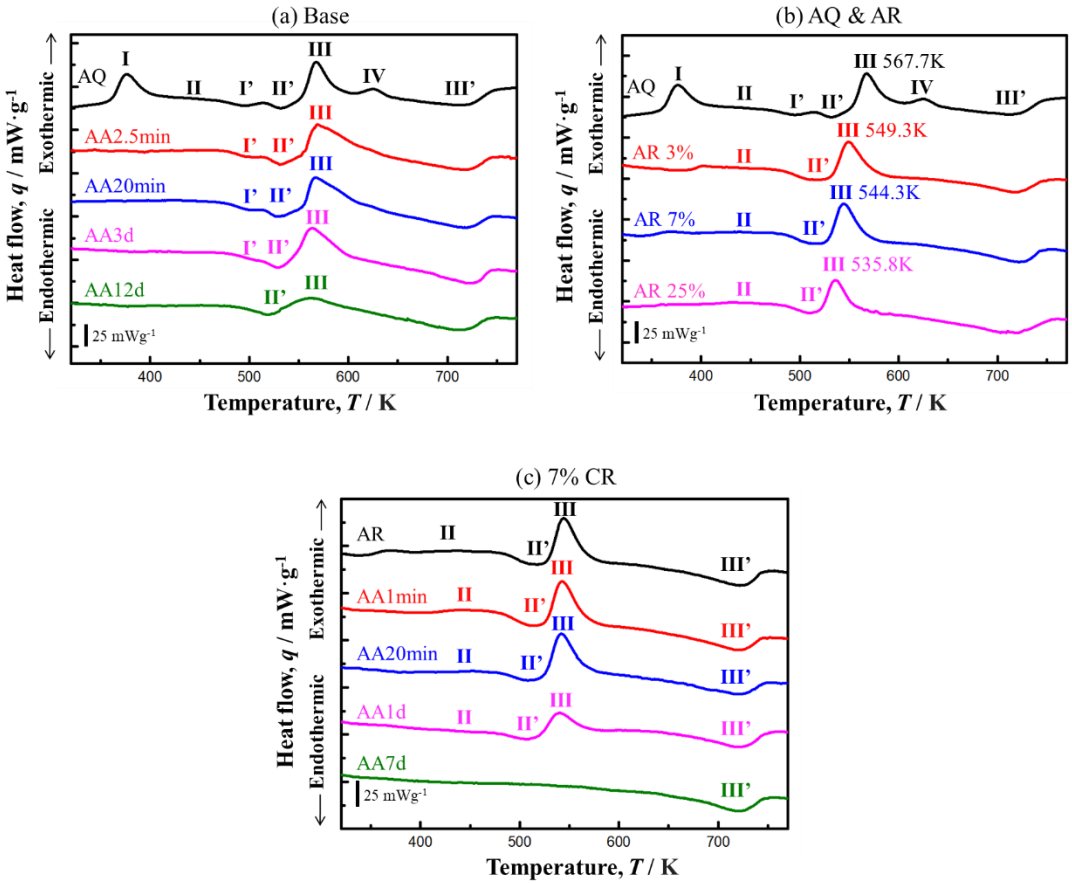

Fig. 2.3 DSC curves for (a) base alloy aged at 443 K, (b) AQ and AR alloy with various reduction rates, and (c) 7% CR alloy aged at 443 K.

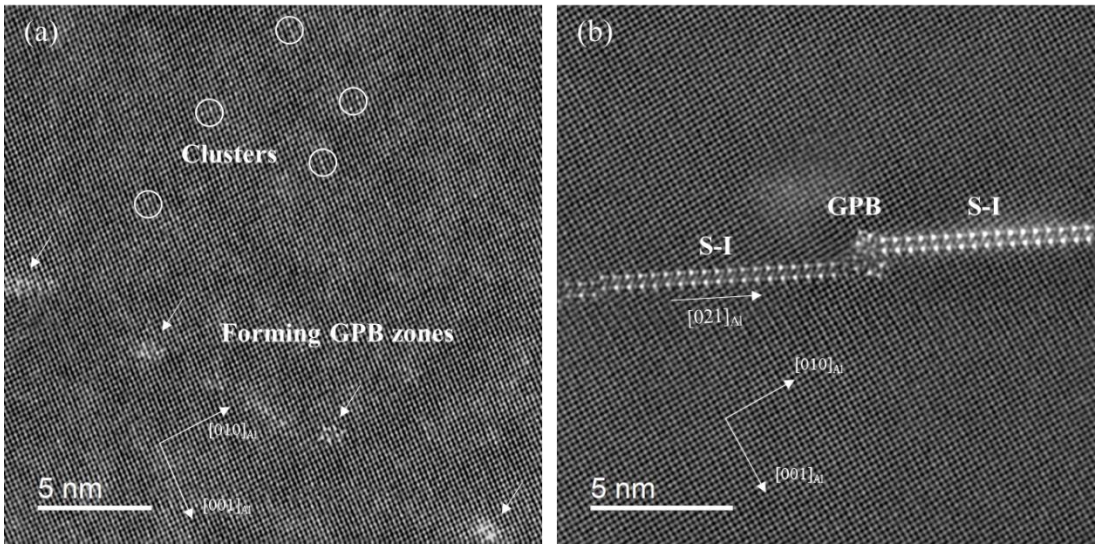

Fig. 2.4 FFT-filtered HAADF-STEM <100>Al oriented images of the base alloy aged at 443 K for (a) 1min, (b) 8 hr. (a) High density of clusters, some clusters are forming into GPB zones. (b) Two precipitates of the S-I phase revealed by their double Cu layers directed along a <210> Al direction, joined by a GPB zone in the center. Notice the rapid contrast variations in the matrix in (a) compared to (b), indicating the high number of clusters in (a).

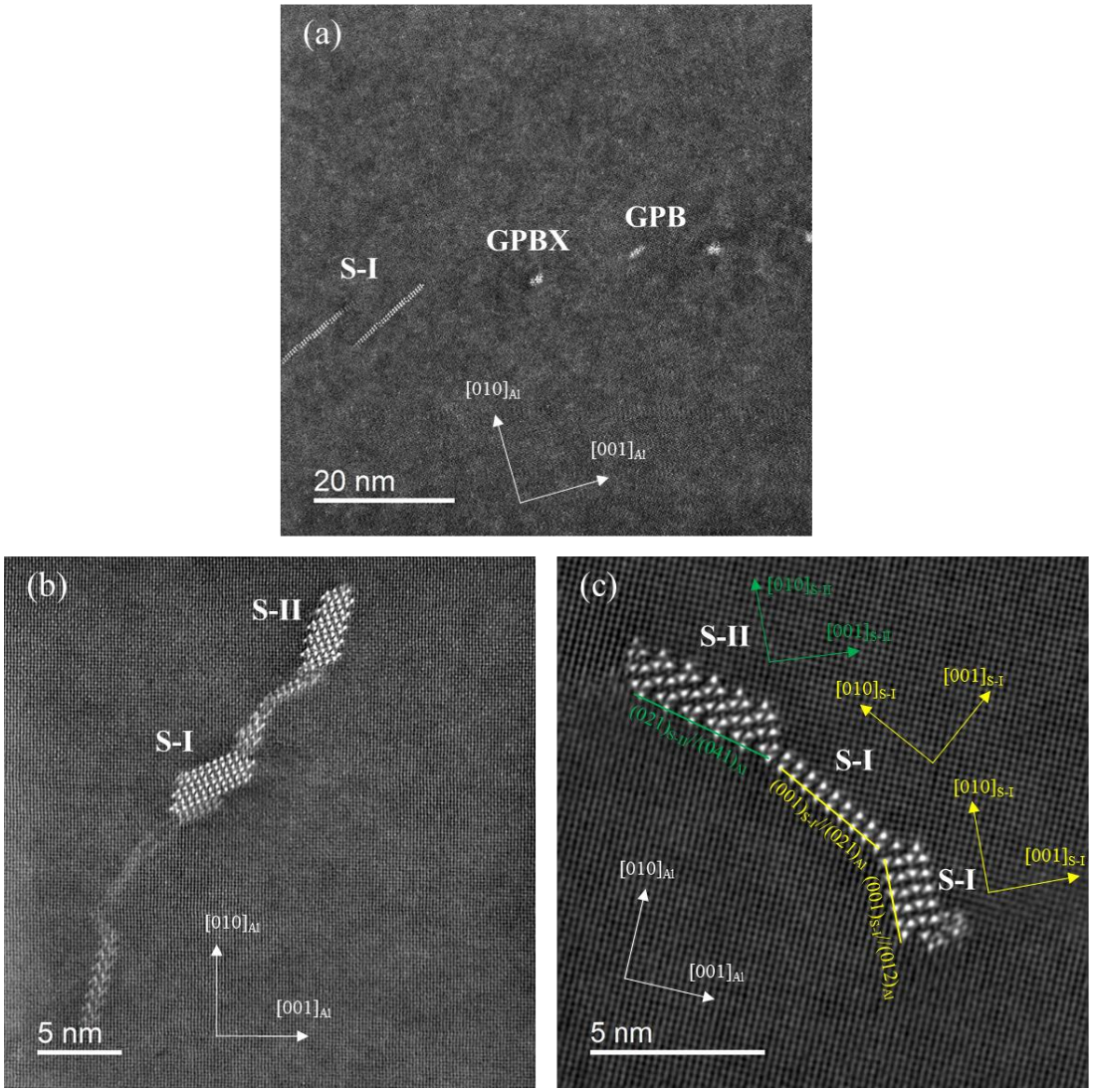

Fig. 2.5 FFT filtered HAADF-STEM <100>Al oriented images of the 7% CR sample aged at 443 K for (a) 20 min and (b–c) 1 day. (a) Normal GPB zones, a GPBX zone and thin S-I phases located along a dislocation. (b) S-I and S-II phases formed along a dislocation. (c) Intergrowth of S-I and S-II phases.

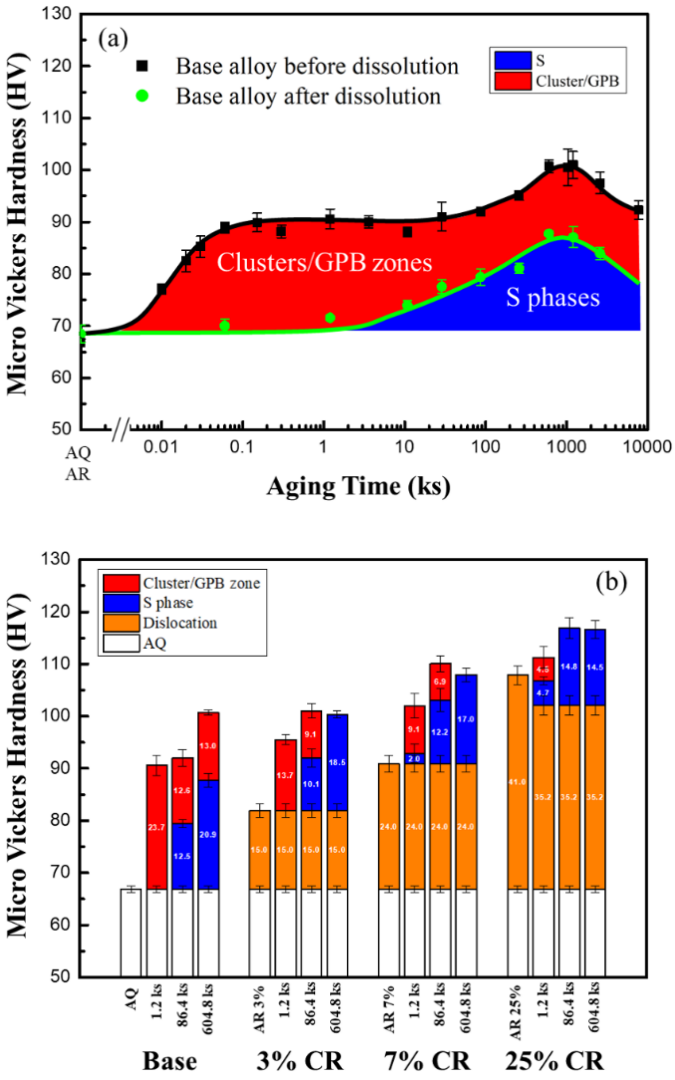

Fig. 2.6 (a) Hardness curves of aged base alloy before and after dissolution experiments. (b) Hardness contribution of dislocations and precipitates in both base and CR samples.

Table 2.2

Estimated hardness contribution of cluster/GPB zones and S phases in the base samples as function of aging time.

Aging time	1min	20min	3hr	8hr	1day	3day	7day	14day	30day
	0.06 ks	1.2 ks	10.8 ks	28.8 ks	86.4 ks	259.2 ks	604.8 ks	1209.6 ks	2592 ks
$\Delta HV_{cluster/GPB} = HV_{aged} - HV_{dissolved}$	22.0	23.7	14.1	13.5	12.6	14.0	13.0	13.9	13.5
$\Delta HV_{S} = HV_{dissolved} - HV_{AQ}$	-	-	7.1	10.7	12.5	14.2	20.9	20.2	17.1
$\Delta HV_{precipitates} = \Delta HV_{cluster/GPB} + \Delta HV_{S}$	22.0	23.7	21.2	24.2	25.2	28.3	33.9	34.1	30.6
$\Delta HV_{cluster/GPB} / \Delta HV_{precipitates}$ (%)	100.0	100.0	66.4	55.7	50.2	49.7	38.3	40.8	44.2
$\Delta HV_{S} / \Delta HV_{precipitates}$ (%)	0.0	0.0	33.6	44.3	49.8	50.3	61.7	59.2	55.8

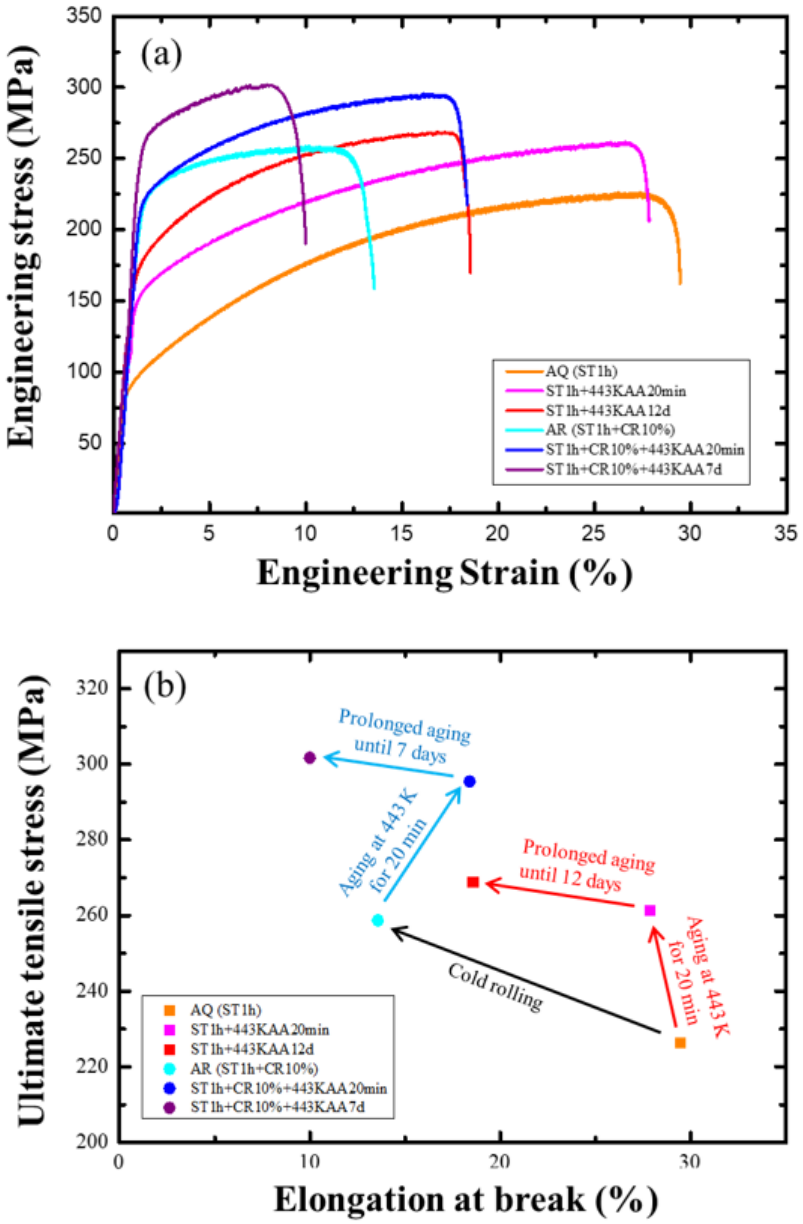

Fig. 2.7 (a) Engineering stress-strain curves for the base samples and 10% CR samples aged at 443 K for various times. (b) Summary of elongation at the break and ultimate tensile stress of both the base and 10% CR samples.

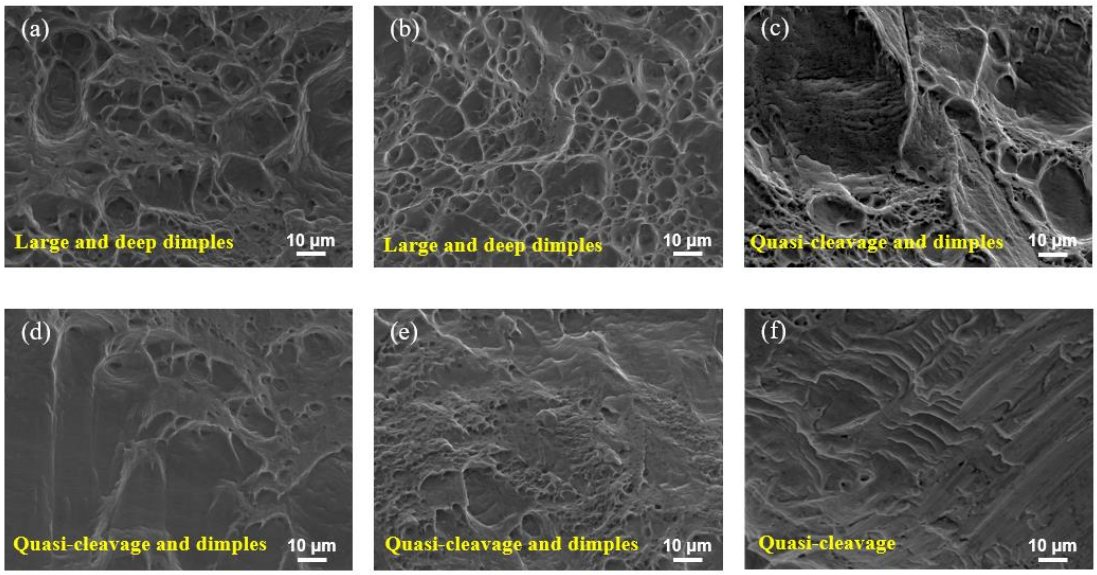

Fig. 2.8 Fracture surfaces of the base and 10% CR samples aged at 443 K for various times: (a) AQ (b) base, 20 min (c) base, 12 days (d) AR (e) CR, 20 min (f) CR, 7 days.

Supplementary Material

TEM images

Precipitate microstructure were investigated by a conventional TEM using a JEOL 3010 operated at 300 kV. Images were taken from a $<100>_{Al}$ direction. The selected area diffraction patterns (SADP) were taken inside of the grain.

Fig. S2.1 shows dark-field TEM image with SADP in the 3% CR samples aged at 443 K for 20 min. High density of dislocation loops (red arrowed) and lines (yellow arrowed) were discovered, the specific diffraction pattern of GPB zone was also confirmed.

The bright field TEM image of the precipitates and corresponding SADP for S phases in the 3% CR samples aged at 443 K for 12 days are shown in the Fig. S2.2. S phases elongated along three $<100>_{Al}$ directions (red framed) and formed on dislocations (green framed) were observed.

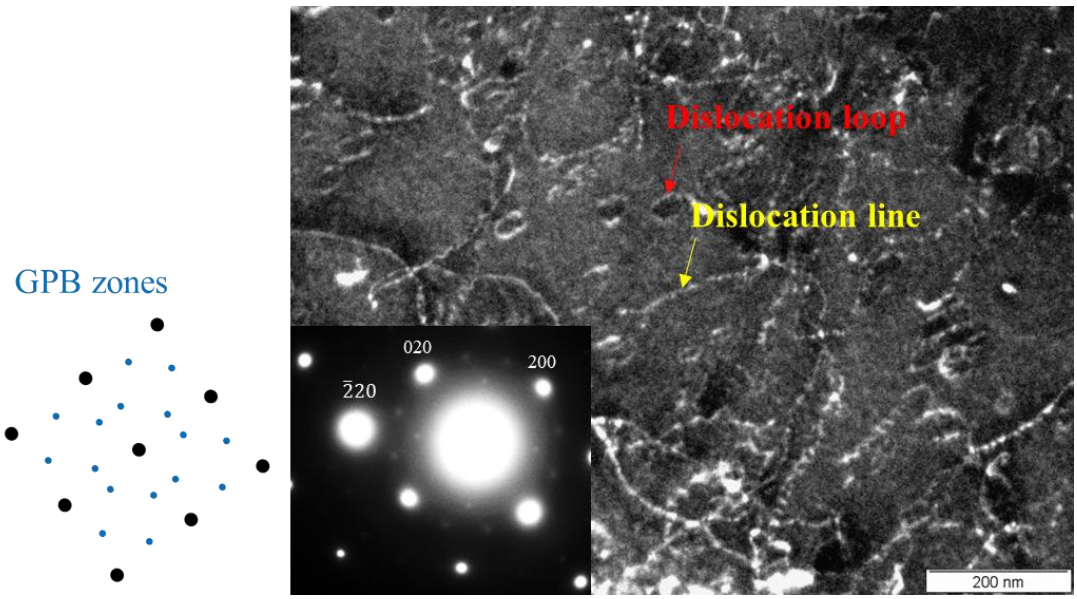

Fig. S2.1 Dark field TEM image taken along a $<001>_{Al}$ direction with corresponding selected area diffraction pattern for the 3% CR sample aged at 443 K for 20 min. Note that the diffraction spots on {110} positions are due to the surface layer artefact.

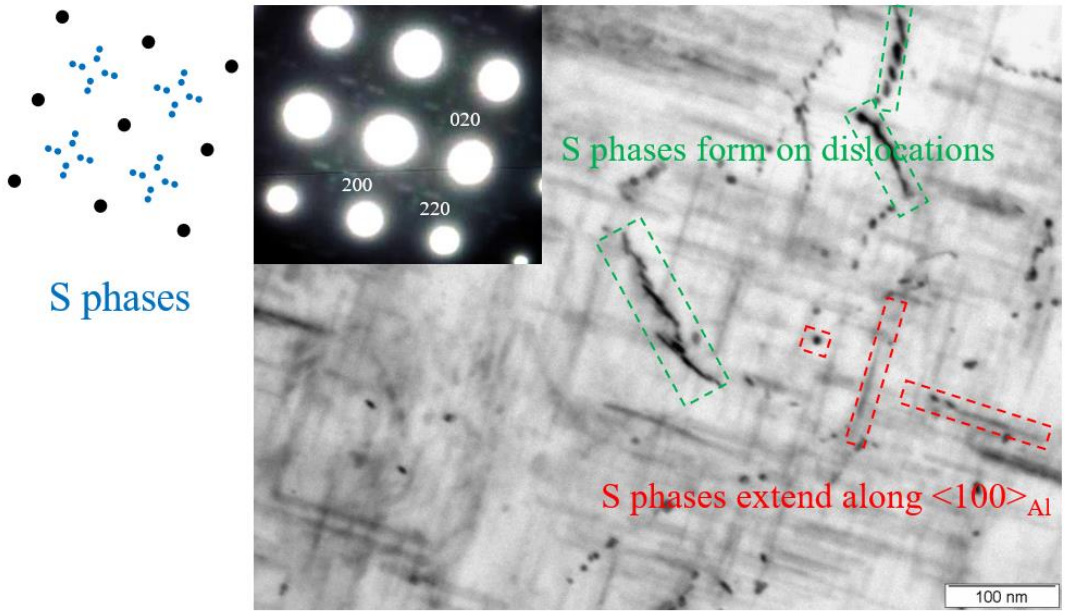

Fig. S2.2 Bright field TEM image taken along a $<001>_{Al}$ direction with corresponding selected area diffraction pattern for the 3% CR sample aged at 443 K for 12 days.

Chapter 3. Precipitation processes and structural evolutions of various GPB zones and two types of S phases in a cold-rolled Al-Mg-Cu alloy

3.1 Introduction

Al-Cu-Mg alloys are widely used in aerospace and automotive industries due to their well-balanced properties regarding high strength-to-weight ratio and good formability. The strength is ascribed to the high density of nanometer-sized precipitates forming during a heat treatment referred to as “aging”. The age-hardening process is mainly associated with solute clusters, Guinier–Preston–Bagaryatsky (GPB) zones, and S-phase precipitates (Al_2CuMg). Therefore, detailed knowledge about the precipitation process and the structural evolution of various precipitates is particularly interesting for gaining improved control of the mechanical properties.

In this paper, we focus on the Al-Mg-Cu alloy with a high Mg/Cu ratio. The generally accepted precipitation sequence which forms S phases in Al-Mg-Cu alloys is [1–9]:

SSSS → Cu/Mg clusters → GPB zones (→ S’ phases) → S phases (1)

“SSSS” refers to the supersaturated solid solution in the (α) Al matrix and “Cu/Mg nanoclusters” to the precursors of the GPB zones. The GPB zone is considered to be a short-range ordering of Cu and Mg solute atoms [1]. The S’ phase is a slightly strained version of the equilibrium S phase [10].

GPB zones have been investigated using various experimental techniques. Silcock predicted the rod-like morphology of GPB zones [11], which was confirmed by Ringer et al. [9] and Reich et al. [12] using transmission electron microscopy (TEM) and atom probe tomography (APT), respectively. Kovarik et al. identified the unique atomic structure of the commonly observed GPB zones [13–15]. Based on high-angle annular dark-field scanning TEM (HAADF STEM) imaging with the support of ab initio calculations, he showed that the GPB zones can be understood as agglomerations of rod-like structural units with sub-nanometer diameter. To categorize the various sizes, he denoted them as GPB^1 and GPB^2, etc. Starink and Wang proposed a Cu-Mg dimer

model, which is considered to be the simplest form of solute clusters [16]. Recently, tetragonal prism-like GPB-T zones were reported by Wang et al. [17], while the transformation process from the initial structures of atomistic building blocks to mature GPB structures was elucidated by Pan et al. [18].

In 1943, on the basis of X-ray diffraction (XRD) work, Perlitz and Westgren found the S phase had an orthorhombic crystal structure (Cmcm, a = 0.400 nm, b = 0.923 nm, c = 0.714 nm) and a formula unit of Al_2CuMg [19]. Since S' and S are basically variations of the Perlitz-Westgren (PW) model, with similar composition (Al_2CuMg), lattice parameters and even crystal structure, in the current work we consider them the same phase. Two variants of S phases with different crystallographic relationships with the Al matrix have later been reported, called "S-I" and "S-II" [20,21]. A noticeable difference concerns the main interface morphology: The S-I interface is straight, while S-II has a stepped interface [22], and they have a consistent relative rotation of about 5°. The structure of the S-I phase conforms to the PW model [23]. The crystal structure of the S-II phase has not yet been determined.

The most commonly observed lath-shaped S phase is of the S-I type, with an orientation relationship (OR) with the Al matrix satisfying [1,10]:

$$[100]_S//[100]_{Al},\ [010]_S//[02\bar{1}]_{Al},\ [001]_S//[012]_{Al}\quad \text{(OR1)}$$

Majimel et al. [24,25] proposed another orientation relationship for the S-II phase:

$$[100]_S//[100]_{Al},\ [010]_S//[05\bar{2}]_{Al},\ [001]_S//[025]_{Al}\quad \text{(OR2)}$$

Kovarik et al. reported coherent interfaces $\{021\}_S//\{014\}_{Al}$ (OR3) [26]. Winkelman et al. [22] and Sunde et al. [27] found they had a continuous (or near continuous) range of misorientation angles between two rational limits defined as $(001)_S//(021)_{Al}$ and $(0\bar{2}1)_S//(014)_{Al}$, about the $[100]_S//[100]_{Al}$ common axis. Wang [28] and Styles et al. [29] reported that the S-II phases grow at the expense of S-I phases and that the S-II phase is the more stable one of the two.

It is well known that microstructure containing GPB zones cause the formation of S phases during aging [3,6]. However, GPB zones and S phases are structurally different and have various types, while the relationships and the detailed structural evolution are still unclear. It is also known that S-I is lath-shaped and S-II is rod-shaped [22], but the mechanisms behind are not fully understood.

In this paper, we report a novel type of GPB zone forming in a cold-worked Al-Mg-Cu alloy, which we denote as “GPBX” (to signify an unknown type), we also find a new precipitation process related to it. Also, an atomic model for the S-II phase is proposed, supported by atomic-resolution HAADF-STEM in association with first-principles energy calculations. Then, the general evolution of precipitation and the structural connections between various GPB zones and S phases are discussed in detail. Furthermore, changes in the morphology of two types of S phases during aging were observed, and related growth mechanisms were proposed. Finally, the similar behavior of Cu and Si regarding the formation of precipitates has been discussed. We show how this explains the structural similarity/connection of precipitates in 2xxx and 6xxx Al alloys.

3.2 Experimental methods

3.2.1 Materials and heat treatments

Materials used in this paper were cast and homogenized at 773 K for 10 h. After this, the billets were rolled to sheets with 3 mm in thickness at 683 K. Finally, the sheets were cold rolled to 1.2 mm in thickness. The whole manufacturing process was carried out at Furukawa sky (now, UACJ Corporation). Table 3.1 gives the chemical composition of the investigated Al-Mg-Cu alloy.

Sheet-shaped samples of dimension 10 x 10 x 1.2 (in mm) were solution heat-treated in a salt bath at 793 K for 1 hour, followed by quenching in ice-water, where they were held for 1 min. After solution heat treatment (SHT), cold rolling (CR) was performed at room temperature for 7% reduction rates. The rolling ratio was determined by measuring the reduction in sheet thickness. Isothermal artificial aging was carried out in an oil bath at 443 K for up to 90 days. The as-quenched and as-rolled conditions are abbreviated as “AQ” and “AR” respectively.

3.2.2 Hardness measurements and differential scanning calorimetry (DSC)

The Vickers hardness was measured at room temperature, applying a load of 200 g for 15 s in a MATSUZAWA SERIES MMT-X Micro-hardness tester. A reported hardness value is the average of five out of a set of seven hardness data points (excluding the two extremal values).

Differential scanning calorimetry (DSC) was carried out under an argon atmosphere in a Rigaku DSC8230 instrument at a constant heating rate of 0.167 K/s. A 40 mg sample of pure Al (99.99 %) served as a reference. The temperature (range 223 to 773 K) was controlled using a liquid nitrogen controller.

3.2.3 Transmission electron microscopy

TEM specimens were prepared by first grinding the 1.2 mm thick sheet samples down to around 100 μm thickness, from which were punched 3 mm diameter discs. Subsequently, the discs were electropolished until perforation using a Struers TenuPol-5 machine. The electrolyte (1/3 nitric acid and 2/3 methanol) was kept between 243 K and 253 K during electropolishing. To reduce the amount of contamination, prior to the HAADF-STEM observations, all specimens were plasma cleaned for 3 minutes in a Fischione 1020 Plasma Cleaner.

Precipitate microstructure were investigated by high-resolution HAADF-STEM in a $<100>_{Al}$ orientation, as they are needles or plate-like extending in this direction. The instrument was a double Cs corrected JEOL ARM 200F operated at 200 kV. The convergence semi-angle was set to 28 mrad and the inner collection angle of the HAADF detector was 48 mrad.

In order to further improve the clarity, all of the HAADF-STEM images were filtered using a circular bandpass mask applied on the respective fast Fourier transform (FFT), removing all spatial frequencies that correspond to features in the real space smaller than 0.15nm, and an inverse FFT (IFFT) was performed on the masked area.

The HAADF-STEM technique utilizes the Z contrast arising from scattering from the core electrons of atoms. In column resolved images, a larger average atomic number Z of a column will scatter more, which pertains to a higher brightness in the scanned image [30]. With a limited number of atomic species, and under an assumption of fully occupied columns in a precipitate, structural models may be extracted and checked by DFT calculations. For the $<100>_{Al}$ orientation HAADF-STEM images in this work, the (projected) columns of highest contrast represent Cu atoms, while the columns of lowest contrast represent Mg atoms. In addition, it was demonstrated that the crystal structures of metastable precipitates in the Al-Mg-Cu and Al-Mg-Si(-Cu) systems are governed by certain construction rules [31]. According to these rules, every Al atom has 12 nearest neighbors, every Mg atom has 15 and every Si or Cu has 9. This allows

for the atomic overlay of precipitates imaged in cross-section in atomically resolved HAADF-STEM images, where every Al atom is surrounded by 4 atoms of opposite height, every Mg by 5 and every Si or Cu by 3 (making them triangular sites). Therefore, the identification of atomic columns in the HAADF STEM images was done based on these principles.

3.2.4 First-principles calculations

Formation enthalpies of the different phases were calculated with density functional theory (DFT) using the Vienna ab initio simulation package (VASP) [32,33]. The calculations were performed at zero Kelvin using the projector augmented wave method within the PBE (Perdew–Burke–Ernzerhof) generalized gradient approximation [34]. The plane-wave energy cut-off was 400 eV and a Monkhorst-Pack gamma-centered k-point mesh was used, with maximal k-point distances of 0.18 $Å^{-1}$ in each direction [35]. The electronic accuracy for self-consistent loops was set at 10^{-6} eV and the atomic positions were relaxed to a maximal force of 0.001 eV/Å between atoms using first-order Methfessel-Paxton for the smearing of partial occupation and a smearing factor (SIGMA) of 0.2. Separate calculations were performed for more accurate energies using the tetrahedron method with Blöchl correction for the smearing [36].

The formation enthalpy was calculated as described in Marioara et al. [37]. To allow for easier comparison, all structures were calculated using the same fixed Al lattice parameter of 4.0400 Å (relaxed with DFT). For each supercell size, separate reference calculations for the formation enthalpy were performed with a single solute in the corresponding Al supercell. This cancels out systematic errors arising from the k-point meshing but introduces a slightly overestimated strain contribution to the formation enthalpies (corresponding to the surrounding Al being infinitely hard). How much the strain contribution is overestimated was checked by fully relaxing the cell size of the structures with the largest absolute internal pressure in Fig. 3.4, providing a lower limit to the strain contribution (corresponding to the surrounding Al being infinitely soft). The real formation enthalpy is somewhere in between.

3.3 Results

3.3.1 Age-hardening behavior and DSC results

Fig. 3.1(a) shows the hardness as a function of aging time at 443 K for the non-deformed (AQ) and rolled (AR) samples. The hardness of the AQ sample (black line) is lower throughout the entire aging period. Fig 1(a) shows the typical four stages in these alloys: The first stage is characterized by a fast increase, where approximately 70% of the peak hardness is reached during the first 60 s. The second stage is characterized by a "plateau", where hardness changes little for about 1 day. During stage three the hardness increases again, reaching a peak after 12 days. During stage four over-aging takes place, causing the hardness to fall again.

The red curve in Fig. 3.1(a) shows that cold rolling results in an overall higher hardness. The first stage has a higher starting value, including a slower increase to a shorter, postponed second stage (plateau). From the plateau, it transcends to the peak hardness faster, but stays at maximum until about the same time as the non-deformed maximum, where after the over-aging sets in.

Fig. 3.1(b) gives the corresponding DSC curves. The AQ sample shows an initial peak at about 376 K, attributed to the formation of the clusters [7], which is absent for the AR samples. A second peak, occurring at about 568 K, is also present in the AR curves. This is attributed to the precipitation of S phases [8,38]. The second peak occurs earlier (at a lower temperature) for the deformed samples.

3.3.2 Microstructure

The effect of deformation on the precipitation process of high Cu/Mg ratio alloys has been documented elsewhere [39–43]. However, to our knowledge, the precipitation process in deformed Al-Mg-Cu alloys with low Cu/Mg ratios has not been investigated in detail. In order to clarify the microstructure of precipitates and the precipitation process in relation to deformation, the STEM experiments were mainly performed on the AR sample aged at 443 K for various times.

I. Various GPB zones

In this work, GPB^1, GPB^2 [13–15,18,44] and GPBX zones were observed in the AR sample aged at 443 K for 20 min.

HAADF-STEM images and atomic models of the various GPB zones are shown in Fig. 3.2. GPB zones are rod-shaped particles with their long axes parallel to the viewing direction $[100]_{Al}$. Thus, the HAADF-STEM images show the cross-sections of GPB zones, and each bright dot represents a projected atomic column parallel to the viewing direction, where the period of a column assumes that of the aluminum (i.e. a=4.05Å). The structure of GPB zones was first identified by Kovarik et al. [13–15], and the models in Fig. 3.2(d) and (e) are built based on their work.

The GPB^1 zone is the smallest type of stable GPB zone that can exist independently. The building block has 9 columns, with the central column consisting of interstitial atoms. It is essentially a stack of single Al unit cells in one $<100>_{Al}$ direction, with corners replaced by Mg, lateral face centers by Cu, and where the central column (top/bottom) is pushed a plane distance (2.025Å), so the atoms end up at "wrong" heights (in the unit cell centers) in respect to the FCC structure of Al. These interstitial atoms may contain Al, Mg, or Cu, where calculations show that Al and Cu are the most and least energetically preferred elements, respectively [18,45]. In Fig. 3.2(a), the high column contrasts indicate that the central column of the middle GPB^1 zone is rich in Cu, which means it could be a developing GPB^1 zone, where Cu atoms will be replaced by Mg and Al upon further aging. The more frequently observed GPB^2 zone is a 16-column unit ($Al_4Cu_6Mg_6$), which can be understood as the GPB^1 zone extending along the $<112>_{Al}$ direction with $<112>_{Al}/2$ length. The extension will be discussed in section 3.4.1-I. Note that the GPB^{1*} zone is the smallest GPB zone with only half a structure unit [14].

Pairs of such GPB zones generally connect along $<114>_{Al}/2$, as can be seen in Fig. 3.2(a) and (b). For instance, the $2GPB^2$ zone is composed of two $<114>_{Al}$-oriented GPB^2 zones. The main interface formed by two GPB^2 zones is parallel with a $\{210\}_{Al}$ plane, which is the common interface of the S-I phase and Al matrix. Moreover, the structure of the connecting part (marked by the purple line in Fig. 3.2(e)) between two GPB^2 zones is a structural part of the S phases, which will be discussed later. Note that the $<114>_{Al}$ and $<112>_{Al}$ mentioned above appear as $<014>_{Al}$ and $<012>_{Al}$ in the $(100)_{Al}$ plane of Fig. 3.2.

Fig. 3.2(c) and (f) show a previously unreported type of GPB zone, which we name "GPBX zone". Following the normal convention, the composition of the GPBX zone

can be estimated as $Al_2Cu_4Mg_4$. The input fractional coordinates of the atomic sites in the GPBX zone are shown in Table 3.2. A major difference with other GPB zones relates to a higher number of columns/atoms in the precipitate over the same cross-section than in the matrix. As an example, the rectangle in Fig. 3.2(f) comprising the GPBX zone, is fixed between lattice positions in the matrix. It contains 22 columns, compared to 20 in the matrix. In other words, each GPBX unit has acquired two additional columns. The two individual GPBX zones in Fig. 3.2(f) have separation approximately along $<114>_{Al}$ or $<113>_{Al}$, where $<114>_{Al}$ is related to S-II phases. We suggest that the GPBX zone is the GPB zone of closest structural relation with the S-II phase. This is discussed below (cf. section 3.4.1-II).

II. Two types of S phases

Fig. 3.3 shows two types of S precipitates observed in the AR samples aged at 443 K for 1 day. Most precipitates are associated with dislocation lines, as in Fig. 3.3(a). Fig. 3.3(b) and (c) are enlarged parts of Fig. 3.3(a) and depict examples of lath-like S-I and S-II precipitates with the smallest thickness. Their corresponding atomic models are shown in Fig. 3.3(d) and (e). These types of S phases were commonly observed in the current work. We find that columns/atoms in both structures follow the construction rules recently published [31]. The white overlaid rectangles in Fig. 3.3(b) and (c) mark the supercells used for DFT calculations. The input fractional coordinates of the atomic positions in the supercells containing the S-I and S-II phases are also shown in Table 3.2. Small S phases will coarsen during aging. Corresponding examples of S-I and S-II are given in Fig. 3.3(f) and (g), respectively.

The S-I phase in Fig. 3.3(f) has the a-axis parallel to the viewing direction, while b- and c- axes point in two mutually perpendicular $<012>_{Al}$ directions in the plane. The S-I phase has a lath shape morphology, with the flat (main) interface $(001)_{S\text{-}I}$ common with $(0\bar{1}2)_{Al}$. The angle between $[010]_{S\text{-}I}$ and $[010]_{Al}$ was estimated as 26.6°. The reason for the scattered columns at the $(010)_{S\text{-}I}//(021)_{Al}$ interface is likely caused by the poor coherency of the interfaces: Assuming the structure of S-I phase accords with the PW model, the plane spacings $d(010)_{S\text{-}I}$ and $d(001)_{S\text{-}I}$ would be 0.923 and 0.714 nm, respectively, whereas $d(021)_{Al}$ is 0.9055 nm. This gives a mismatch between $(001)_{S\text{-}I}$ and $(0\bar{1}2)_{Al}$ planes about 1.9% (implying coherency). In comparison, the $(010)_{S\text{-}I}//(021)_{Al}$ interface has a mismatch of 21.1%.

The S-II phase in Fig. 3.3(g) has a much coarser, rod-shaped cross-section. Again, the a-axis is parallel to the viewing direction $[100]_{Al}$. The figure shows the S-II phase has an interface relation $(021)_{S\text{-}II}//(041)_{Al}$, verifying OR3 [26]. It also exhibits a typical stepped interface, marked with the jagged red line. This type of interface can be formed when the interface loses coherence and grows along $[010]_{S\text{-}II}$ until a new match is found. Distinct heights and widths of steps can lead to different interfaces previously reported in other publications [20,26,28]. Here, the angle between $[010]_{S\text{-}II}$ and $[010]_{Al}$ was estimated as 21.8°, which satisfies OR2. Given in Table 3.2, the supercell of the S-II phase has the dimensions a = 19.21 Å, b = 4.05 Å, c = 16.70 Å, and monoclinic angle β = 94.4°. Thus, the S-II phase can be described as a monoclinic structure with space group C2/m (No.12) rather than orthorhombic, as assumed for the S-I phase. The relationship between two types of S phases will be explained in the discussion part.

3.3.3 DFT calculations

The results from the DFT refinements/calculations are shown schematically in Fig. 3.4 (average formation enthalpy per solute atom versus pressure), with the numerical values listed in reference [46]. According to the calculations, the following conclusions can be drawn:

(1) By comparing Mg4Cu5-GPB^{1}and Mg4Cu4-GPB^1, it is again confirmed that Al is more energetically preferred than Cu on the interstitial position of GPB^1 zones. (2) As normal GPB zones grow (GPB^1- GPB^2- 2GPB^2, blue points), the formation enthalpy continues to decrease. Even without relaxation, there is almost no misfit pressure in normal GPB zones, since they still follow the atomic arrangement of the Al matrix. If relaxation is performed, experience tells the formation enthalpy is expected to drop slightly. (3) GPBX zones (pink triangles) have large pressures, partly because they contain extra atoms compared to the Al matrix. After relaxation, the energies of GPBX zones (red triangles) are comparable to those of normal GPB zones. Thus, we expect and also observe the GPBX zones together with the normal GPB zones. (4) The $<114>_{Al}$-oriented 2GPBX zone is more stable than the $<113>_{Al}$-oriented one, which supports the observation that most GPBX zones are found to be $<114>_{Al}$-oriented. (5) The S-I and S-II phases have almost the same formation enthalpy. There is no obvious preferred order for formation.

Note that the GPBX zones and S-II phases generally appear at dislocation. However, the influence of dislocations has not been considered in the calculated models, which may be one reason for the large pressures of GPBX zones and S-II phases. Forming at a dislocation indicates an advantage, thus we expect their actual formation enthalpies to be even lower.

3.4 Discussion

3.4.1 Precipitation mechanisms of S phases

The Specific transformation mechanisms leading to the S phase will be discussed in this section. Taken together with the mechanism of S phase (S-I phase) formation from GPS zones earlier proposed by Wang and Liu et al. [47,48] in Al alloys with high Cu/Mg ratio, we believe the current work can clarify the mechanisms of S phase formation across the entire Al-Cu-Mg system.

I. Suggested formation path from normal GPB zones to S-I phase

Fig. 3.5 shows HAADF-STEM images of GPB zones and typical S-I phases in the $[100]_{Al}$ orientation, where their main interface typically projects along a $<021>_{Al}$ direction. In this paper, normally observed GPB^1, GPB^2, GPB^3 and GPB^4 zones, etc. are collectively referred to as "GPB^n zones" (n = 1, 2, 3…) with corresponding composition $Al_{3n-2}Cu_{2n+2}Mg_{2n+2}$. Examples of GPB^1 can be found in Fig. 3.2(a), of GPB^2 in Fig. 3.2(a, b), of GPB^3 in Fig. 3.5(b), and of GPB^4 in Fig. 3.5(c).

Fig. 3.5(a) shows a small S-I phase consisting of two parallel Cu layers. Fig. 3.5(b) and (c) show that GPB^n zones and the S-I phase have a common main interface, which projects to a line along $<021>_{Al}$. This strongly suggests that GPB^n can nucleate next to the S-I and keep the elongation direction unchanged when it transforms to S-I.

In order to understand the transformation mechanism from a small GPB^n zone to a mature S-I phase, a schematic diagram suggesting the structural evolution is given in Fig. 3.6(a). It consists of 3 parts emphasizing: (1) the growth of a GPB zone (Fig. 3.6(a1-4)), (2) the transformation from a GPB zone to an S-I phase (Fig. 3.6(a4-6)), and (3) the growth of an S-I phase (Fig. 3.6(a6-9)). We find these phases are most conveniently discussed in terms of the common 3-fold substructural part, called "triangle" in the following discussion, their projected shape in the $<100>_{Al}$ orientation shown here. In the figure, it is recognized by blue lines, drawn between the three nearest

columns (with atoms on the same neighbor $\{100\}_{Al}$ plane) around a Cu column. Thus, the lines connect two Al columns and one Mg column (or one Al and two Mg on the edge triangle), where one Al column is still "anchored" in the aluminum, i.e. still part of the FCC. The length of these columns can vary but must be the same for all atoms in a precipitate (because of the growth rules). The columns will usually be referred to as "atoms" in the following.

(1) The GPB zone develops on a $\{021\}_{Al}$ plane, necessarily by capturing solute atoms from the matrix [13]. The growth from a GPB^n zone to a GPB^{n+1} zone can be accomplished by introducing two triangles plus an interstitial Al (marked "+") in between. An example (growth of GPB^3 to GPB^4) is given in Fig. 3.6(a2-4): Here, the internal Cu and Mg atoms at the top short end of the GPB^3 zone (Fig. 3.6(a3)) swap positions with outside Al atoms (small arrows), which together with external pairs of Mg and Cu in the FCC adds two Cu-centered triangular structures, meaning growth. In this case, no vacancies are produced.

(2) A structural transformation path from the GPB^4 zone to the S-I phase (main part) will, however, generate vacancies. The mechanism is suggested in Fig. 3.6(a5-6). It can be understood as a shift of the (left-hand side) main interface atoms, where the Cu atoms end up "interstitially" as the centers of new triangles, while Mg atoms swap positions with Al atoms. The Cu interstitials imply a higher packing in the precipitates relative to the FCC, effectively creating vacancies by the abandoned Cu-positions. A similar vacancy generating mechanism has been suggested previously [48]. This allows the vacancies to be replaced by Al atoms and diffuse into the matrix.

The transformation of the edge also produces a vacancy. It involves the three (internal) top solute atoms in Fig. 3.6(a4-5)) of the GPB^4 zone, but is slightly different: The top Cu atom ("1") forms a new triangle, initiated by a similar displacement to an interstitial position. An Mg atom ("2") occupies the position left by the Cu atom. A second Mg atom ("3") exchanges position with the nearest Al atom on the right-hand side to the vertex of the new triangle.

We can generalize the transformation in the following way: a GPB^n zone containing $2(n+1)$ Cu (and Mg) atoms will upon transformation add $(n+1)$ atoms to the S-I phase, since exactly half of Cu (and Mg) atoms participate in the structural transformation. Also, it implies a number $(n+1)$ of vacancies are created.

(3) The growth of the S phase can be viewed as two separate events: width and thickness growth along $[010]_{S\text{-}I}$ and $[001]_{S\text{-}I}$, respectively. Width growth involves the acquisition of solute atoms at the short end of the projection, extending the S-I structure along $<021>_{Al}$ (cf. Fig. 3.6(a7,8)). Thickness growth is accomplished by nucleation of GPB zones and further transformation to S-I phase (cf. Fig. 3.6(a9)). The mechanisms of these will be explained in later sections.

The model in Fig. 3.6(a9) corresponds to Fig. 3.5(b). The interface structure between the GPB^3 zone and the S-I phase is outlined by the purple dashed ellipse. The same structure exists in Fig. 3.2(c), as the joining part of two GPB^2 zones. It is speculated that this interface structure can serve as the geometric constraint of two adjacent precipitates (GPB^n & GPB^n, GPB^n & S-I, or S-I & S-I) and keep constant during the whole transformation process.

Thus, we conclude that GPB^n zones can act as nucleation points and transform into S-I phases during aging.

II. Suggested formation path from GPBX zone to S-II phase

The GPBX zone, discovered in this work, is found to be a key to understand the S-II phase formation, by serving as an interphase structure between GPB zones and S-II. The HAADF image in Fig. 3.7 shows S precipitates and GPBX zones decorating a dislocation. The GPBX zone unit is represented by brown rhombs. The S phases are delimited by the white stippled ellipses.

The figure shows that GPBX zones tend to be separated by $<114>_{Al}/2$ ($<014>_{Al}/2$ in projection), which coincides with the elongated direction of the cross-section of the S-II phase. Note also that a GPB^{1*} zone makes up the upper edge of the S-II phase cross-section. This phenomenon is common in S phases near dislocations, and can also be seen in Figs. 3 and 9. The dashed red lines in the S-II structure demarcate the expected structure of the S-II phase. Also, the lower part of S-II forms a half GPBX unit. This connects with the lower left series of GPBX units through the common $<114>_{Al}/2$ separation. As may be noticed from Fig. 3.7, the four Cu-positions in a GPBX zone may be viewed as nearest neighbors pushed outwards relative to the matrix positions, where two Al atoms are added. This matches the fraction of extra atoms in the S phases. These observations indicate a structural relationship between GPBX zones and S-II phases.

Suggested transformations related to the GPBX zone are shown in Fig. 3.6(b). The GPBX zone has the same solute amount (4 Cu and 4 Mg) as the GPB^1 zone. There is insufficient evidence for a structural transition between GPB^1 and GPBX. However, we find it likely that the GPBX zone could transform from the GPB^1 zone by the same rules as was applied to the edge part of GPB^n zones above. Thus, equivalent sites "1" (Cu), "2" (Mg), and "3" (Mg) are used in Fig. 3.6(b2-3).

The structural unit of a GPBX zone is indicated by a brown rhombus in Fig. 3.6(b3). It can be viewed as two Cu-triangles shared by the short diagonal, brown dashed line. (Every Cu-vertex is also a center in a "blue" triangle, as explained above.) The S-II structure can be obtained by splitting the Cu-triangles and adding a pair of Cu into the structure (cf. Fig. 3.6(b4)), while the specific orange parallelogram structure will be formed (cf. Fig. 3.6(b5)). The mechanism of S-II phase formation is basically the same as that of S-II phase width growth (see below).

The width growth process of the S-II phase can be divided into two steps: (1) In the first step (Fig. 3.6(b6)), the upper Cu atom swaps position with its nearest neighbor Al atom. Furthermore, the 4 Al atoms in the front of the extension become replaced by 2 Cu and 2 Mg atoms from the matrix. This destroys the edge structure (the half GPBX structure), while forming a GPB^{1*} zone. This initial step yields the structure shown in Fig. 3.6(b7), which is identical to the S-II structure demarcated in Fig. 3.7. Note that the central Al atom of the GPB^{1*} zone also moves into an interstitial position. (2) For the second step (Fig. 3.6(b8)), the external Cu atom on the upper right side changes position and forms a new Cu-centered triangle together with the interstitial Al atom and the "single" Mg atom (not paired with Cu). At this point, the edge structure of the S-II phase has obtained the half GPBX structure again, having completed one cycle of S-II width growth.

GPBX zones can nucleate next to the S-II phase, which can aid its thickness growth (cf. Fig. 3.6(b10)). This is similar to the thickness growth of S-I phases through GPB zone nucleation and transformation. The nucleation of additional GPBX zones follows the $<014>_{Al}$ direction as shown in Fig. 3.7, but there is no structural constraint between GPBX zones and S-II phases.

III. Effects of dislocations on the precipitation processes

It is well known that dislocations promote precipitation, such as by reducing the formation energy of precipitates and promoting solute atom diffusion along dislocation lines. Fig. 3.6(c) shows atoms are separated by a dislocation, the right-hand side purple atoms are on the extra half-plane, or it can be understood as there is a stacking fault on the right-hand side. As a result, the atom arrangement near the dislocation line will be changed, and generate special positions with 3 and 5 nearest atoms on opposite height preferred by Cu and Mg atoms, respectively, which can help the nucleation of certain precipitates.

GPB^n zones and S-I phases are generally observed both in the bulk of the Al matrix or near dislocations. In the current work, most GPBX zones and S-II phases were observed in connection with dislocations. Even if S-II phases would require dislocations to form, they will also be observed in undeformed materials, because there will always be a certain amount of intrinsic dislocations, and loops caused by quenching. We believe that both dislocation loops and lines can promote the S-II phase formation by changing the atomic arrangement and generating local stress, but what differs regarding their precipitation promoting abilities is still unclear and worth further study. So far, our observations indicate that there is only one available precipitation process in dislocation-free regions (leading to S-I phases only), while both S-I and S-II phases can form in regions with dislocations. In addition, DSC results indicate that the formation of clusters is strongly limited by the high density of dislocations in cold-rolled samples.

Taking the above discussion into account, the precipitation sequences in the current Al-3Mg-1Cu alloy can be summarized as follows:

(In the Al matrix) SSSS → Cu/Mg clusters → GPB^n zones → S-I phases

(At dislocations) SSSS → GPB^n zones → S-I phases
(At dislocations) SSSS → GPBX zones → S-II phases

These experiments have shown that dislocations can induce the formation of S-II phases. This can be important: It is likely that S-II and S-I phases have different influences on some properties (mechanical or corrosion properties). By applying strain to the material, it suggests the precipitate type and some desired properties can be obtained (locally or globally) without changing the composition. This could provide an

opportunity for advanced product design in a wide range of potential applications. The respective properties of S-I and S-II are worth investigating further.

IV. Overview of the precipitation processes

The possible precipitation processes regarding the S-I and S-II phases are summarized in Fig. 3.8. For simplicity, only Cu atoms are considered.

Fig. 3.8(a) illustrates how adding a Cu-pair in a GPB^n zone produces a GPB^{n+1} zone (plate with cross-section along the $<120>_{Al}$ direction). The structural similarity means the GPB^n zone will, at some point/size go through a structural transformation to a S-I phase (with the displacement of a single Cu layer). In order to extend the thickness of this S-I plate along $[001]_{S\text{-}I}$, it is clearly of advantage that a GPB^n zone initially forms on the S-I main plane, subsequently transforming to S-I phase. A second possible route starts with a GPB^n to $2GPB^n$ zone formation (thickness growth), and a subsequent transformation to S-I phase. For this route, the structural constraints (purple dashed central parallelogram) remain constant. The Cu atoms in GPB^n zones can be classified by their different functions: The Cu atoms on structural constraints are immobile (red circles), while the Cu atoms far from structural constraints (orange circles) will shift position (blue circles). Due to the displacements, the orientation relationship between the two particles changes from $<041>_{Al}$ to $<021>_{Al}$ (cf. Fig. 3.8(a)). This indicates that GPB^n zones transform to S-I rather than S-II.

The growth of the S-I phase along the $[001]_{S\text{-}I}$ direction requires that this process (comprised in the big rectangle in Fig. 3.8(a)) is repeated, with two layers of Cu added for each cycle. The bottom part of Fig. 3.8(a) shows that when multiple GPB^n zones nucleate simultaneously since the Cu atoms on the central GPB^n zone are fixed by structural constraints, this prevents transformation to S-I phase. Thus, a maximum of two GPB^n zones can nucleate at the same time to complete the transformation.

Fig. 3.8(b) shows that the GPBX zone can grow to S-II phase by adding rows of Cu atoms. The number of nucleated GPBX zones along the $<041>_{Al}$ direction (thickness growth) is not limited (cf. Fig. 3.7), since there is no structural constraint between the GPBX zone and the S-II phase. The growth direction of the GPBX zone is not necessarily along the $<052>_{Al}$ direction (OR2), which will be discussed in the next section.

Note that any S phase can be obtained by the growth modes discussed above.

3.4.2 The associations and differences between two types of S phases

It can be seen that S-I and S-II phases have the same composition (Al_2CuMg). As shown above, they have distinct interfaces with the Al matrix due to their different formation mechanisms. This is not surprising since their structures also differ: S-I and S-II have orthorhombic and monoclinic structures, respectively.

I. The coexistence and misorientation angles of the two types of S phase

Using DSC, Wang and Starink [28] observed two exothermic peaks at approximately 543 and 573 K, which they interpreted to correspond to the formation of S-I and S-II phases, respectively. They also concluded that the two types form sequentially rather than independently nucleating and coexisting.

In our present work, the two S types were found to coexist (cf. Fig. 3.9) but no particular transformation relationships were found. Also, the DSC curves in Fig. 3.1(b) show only one exothermic peak attributable to S, which is normal in Al-Mg-Cu alloys [7,8].

Fig. 3.9(a) shows the two S types. A Burger's loop around the particle yields vector $\vec{b}$, showing a dislocation. The precise location is not indicated but is located at the S-II part. The GPB^2 zone on the left-hand side of the S-II phase has a growth direction along $[02\bar{1}]_{Al}$. The angle between $[010]_{Al}$ and $[010]_{S\text{-}II}$ was found to vary from 21.5 to 25.1°, increasing as it approaches the GPB^2 zone.

The S-I phase is orthorhombic with unit axes fixed along two $<021>_{Al}$ directions. The S-II phase is monoclinic, with unit axes that vary slightly in projection. S-II is found mainly at dislocation lines. The angular variation is in the direction of the Burgers vector, which indicates it is caused by the dislocation and the accompanying strain field.

It should be noted that even if the $[010]_{S\text{-}II}$ direction rotates, the $\{021\}_{S\text{-}II}//\{041\}_{Al}$ interface (OR3) is relatively unchanged. If the misorientation angles between the two types of S phases are measured by $\{001\}_{S\text{-}I}//\{021\}_{Al}$ and $\{021\}_{S\text{-}II}//\{041\}_{Al}$ interfaces, then angles between two S phases should be stable at certain values rather than ranges. For example, the angle between the two types of interfaces corresponding to the S-I and S-II phases in Fig. 3.9(a) is constant at 12.5°, exactly the angle between $[0\bar{2}1]_{Al}$ and $[0\bar{4}1]_{Al}$ directions.

II. On the morphology of the two types of S phases

The main growth direction of both S-types is along their common a-axis: $[100]_S//[100]_{Al}$, where periodicity (4.05Å) equals that of aluminum. The cross-sections have different orientations and aspect ratios. Aspect ratios have been estimated elsewhere [22], and it has been reported that the S-I phase is lath-shaped while the S-II phase is rod-shaped [29]. The morphology can be determined by observing the projected shape along the main extension, i.e. their b-c cross-sections in the $(100)_{Al}$ plane, which here means along the a-axis for both types.

For S-I, the b-axis, $[010]_{S\text{-}I}$ defines the main extension of the cross-section. This is reflected in a small mismatch in lattice plane distances of $(001)_{S\text{-}I}$ and $(021)_{Al}$. In terms of thickness, growth is not preferred because of a larger lattice mismatch with the Al matrix, and the special growth mechanism of the S-I phase along $[001]_{S\text{-}I}$ revealed in section 3.4.1-IV: For thickness growth, a new GPB^n zone can nucleate only after the former GPB^n zone has transformed into the S-I phase. Therefore, S-I phases generally have the lath shape morphology with a significant width and a limited thickness.

For the S-II phase, the dimensions of $d(010)_{S\text{-}II}$ and $d(001)_{S\text{-}II}$ were estimated as 0.912 and 0.694 nm, respectively, and labeled "$b_{S\text{-}II}$" and "$c_{S\text{-}II}$" in Fig. 3.9(a). The mismatch between $(021)_{S\text{-}II}$ and $(041)_{Al}$ planes is on the order of 0.5% (~coherent). Compared to the S-I phase, the coarsening of the plate/lath thickness of the S-II phase is easier because of low mismatch and the ease of nucleating more GPBX zones.

As shown in Fig. 3.9, GPB zones (GPB^{1*}, GPBX, and GPB^2 zones) thrive on the edge of S phases. This reduces the interfacial strain. As explained, the S-II phase has structural flexibility, as the $[010]_{S\text{-}II}$ is observed to rotate towards the $[021]_{Al}$ direction, which could facilitate nucleation of the GPB^n zone on the side and structural transformation to the S-I phase. The structural flexibility of S-II phase and the nucleation and transformation of GPB^n zones seem to provide the possibility for the mixed structure of two types S phase. The mixed structure is apparent in images earlier reported [22,27].

The diffusion rate of solutes along dislocations is faster than in the matrix [49]. In addition, the dislocation strain field provides more opportunities for the nucleation of precipitates. These are reasons for the S phases forming preferentially along dislocation lines and the reason the extension of S phases follows the dislocation lines, as seen in

Fig. 3.9(b) and (c). The direction of the trace influences the type, variant, and morphology of the S phases formed. Fig. 3.9(b) and (c) demonstrate that when the trace is near $<021>_{Al}$ or $<041>_{Al}$, S-I or S-II is mainly formed, respectively. Initially, both types of S take on a plate/lath shape. As the aging progresses, the S-I plates get wider and longer, maintaining a lath shape (cf. Fig. 3.3(f)) because of the rules governing growth (cf. Fig. 3.8(a)), while the S-II phase (cf. Fig. 3.3(g)) grows less restrained along the $[010]_{S\text{-}II}$ direction (width growth), achieving a rod shape.

3.4.3 Structural relationship between precipitates in Al-Mg-Cu and Al-Mg-Si alloy systems

Fig. 3.10(a) and (b) show the structure of the GPB^1 zone and the β'' phase, respectively. The GPB^1 zone is present in 2xxx (Al-Cu-Mg) series Al alloys, while the β'' phase is the metastable precipitate commonly found in the peak hardness conditions in 6xxx (Al-Mg-Si) series Al alloys [45,50,51]. The β'' phase is composed of periodically arranged β''- "eyes" (the molecules marked by black, stippled circles). The β''-eye and the GPB^1 zone are isostructural, with 8 solute atoms surrounding an interstitial Al atom. The main difference is in composition, which is $AlMg_4Si_4$ and $AlMg_4Cu_4$, respectively. They can be viewed as arbitrarily long groups of $<100>_{Al}$ FCC columns. Additionally, columns of Cu and Si are reported to follow similar arrangement principles [31], and the similarity of atomic models of clusters in these alloy systems has been confirmed [52]. It is reasonable to expect that Si and Cu replace each other in many cases.

The U2 phase is another metastable precipitate in the 6xxx Al series [53]. The structure of the U2 phase shown in Fig. 3.10(d) can be obtained by arranging the newly discovered GPBX structures (marked by orange rhombus) periodically. Because of the high degree of structural similarity between the precipitates in 2xxx and 6xxx, one can speculate that the GPBX unit with Cu replaced by Si might be found in the 6xxx series as the nucleus for the U2 phase. A reason this would have escaped observation is the poorer Z-contrast of Si as compared to Cu in HAADF-STEM images.

A complex of S-I and E phases is shown in Fig. 3.10(e). The E phase [54] was reported in Al-Mg-Si-(Cu) alloys, with a part of the atomic structure (delimited by green dashed lines) shown in Fig. 3.10(f). Interestingly, a pair of Si atoms within the structure of the E phase (Fig. 3.10(e)) seems to occupy similar positions in the S phase (due to

lower contrast). We conclude that the small amount (0.01 at%) of Si atoms in the current material can aid formation of E phase, indicating the complex structure is more energetically favorable. This supports that Cu and Si are interchangeable in many positions of the precipitates. With a higher amount of Si, more E phase would likely be observed in addition to S phase. This can be an important point for future alloy design.

The precipitation can be viewed as a two-stage process. The first stage is the nucleation at the beginning of aging, from supersaturated solid solution, where the solutes aggregate on the FCC Al matrix, forming small clusters. Their structures can be described in terms of simple arrangement rules the solute atoms take, which are energy minimizing operations linked with strain minimization [31]: Relative to Al, Mg is large, and Si and Cu are small atoms. This creates similar options for reducing strain and energy, thus similar arrangements rules. The exception is that Si has strong directional bonds, and likes to stay in a hexagonal network, something which is not important for Cu.

The second process is the growth stage, where the initially formed nucleus will grow and transform toward the precipitate structure. The type, amount, and structure of precipitates are mainly determined by the phase stability related to the composition. This infers that the 2xxx and 6xxx series Al alloys may have similar structures of the nuclei but different precipitate phases. This phase hybridization can give new possibilities to strengthen the alloy [55,56]. Future designs of alloys should consider the distribution of the different types of precipitates, to achieve the desired alloy properties.

3.5 Conclusions

In this work, we find that GBP zones and S phases are structurally related, and suggest detailed transformation paths from the former to the latter. The main findings are as follows:

1. In addition to the earlier reported GPB^n zones such as GPB^1, GPB^2, etc. a new type of GPB zone named “GPBX” was discovered, which has a higher atomic density than the Al matrix. GPBX zones usually form along dislocation lines and arrange along the $<041>_{Al}$ direction.

2. Two types of S phases were found with distinct ORs with the Al matrix. The crystal structure of S-I phase is orthorhombic as previously reported. The crystal structure of the S-II phase has been determined as monoclinic.

3. The precipitation process in the Al-3Mg-1Cu alloy is suggested as:

(In the Al matrix) SSSS → Cu/Mg clusters → GPB^n zones → S-I phases

(At dislocations) SSSS → GPB^n zones → S-I phases
SSSS → GPBX zones → S-II phases

GPB^n zones can only transform to S-I phases. GPBX zones and S-II phases mainly precipitate near dislocation lines.

4. The two types of S phases can coexist and nucleate close to one another. The S-II phase can shift slightly to ingratiate the strain field nearby, which leads to a range of misorientation angles between the two types of S phases. S-I phases have lath shape morphology, while S-II phases first grow along the dislocation line to become lath-like and further coarsen to rod-shaped precipitates.

5. GPB zones in Al-Mg-Cu alloys were found to be based on molecules/units isostructural to what build the β'' and U2 precipitates in Al-Mg-Si alloys, indicating that Cu and Si occupy similar atomic positions in the precipitates of the two alloy systems. The complex mixed structures of S and E phases are also confirmed. This provides possibilities for alloy designs, i.e. adjusting the alloy composition to obtain desired precipitated phase structure ideal for properties/products.

3.6 References

[1] Y.A. Bagaryatsk, Structural changes on aging Al-Cu-Mg alloys, Dokl. Akad. SSSR. 87 (1952) 397 and 559.

[2] M. Mihara, C.D. Marioara, S.J. Andersen, R. Holmestad, E. Kobayashi, T. Sato, Precipitation in an Al-Mg-Cu alloy and the effect of a low amount of Ag, Mater. Sci. Eng. A. 658 (2016) 91–98. https://doi.org/10.1016/j.msea.2016.01.087.

[3] S.P. Ringer, K. Hono, I.J. Polmear, T. Sakurai, Precipitation processes during the early stages of ageing in Al-Cu-Mg alloys, Appl. Surf. Sci. 94–95 (1996) 253–260. https://doi.org/10.1016/0169-4332(95)00383-5.

[4] S.P. Ringer, S.K. Caraher, I.J. Polmear, cluster hardening in an aged Al-Cu-Mg alloy, Scr. Mater. 36 (1997) 517–521. https://doi.org/10.1016/S1359-6462(96)00415-0.

[5] M.J. Starink, A. Cerezo, J.L. Yan, N. Gao, Reply to the comments on "Room-temperature precipitation in quenched Al-Cu-Mg alloys: A model for the reaction kinetics and yield-strength development," Philos. Mag. Lett. 86 (2006) 243–252. https://doi.org/10.1080/09500830600678888.

[6] G. Sha, R.K.W. Marceau, X. Gao, B.C. Muddle, S.P. Ringer, Nanostructure of aluminium alloy 2024: Segregation, clustering and precipitation processes, Acta Mater. 59 (2011) 1659–1670. https://doi.org/10.1016/j.actamat.2010.11.033.

[7] A. Charai, T. Walther, C. Alfonso, A.M. Zahra, C.Y. Zahra, Coexistence of clusters, GPB zones, S″-, S′- and S-phases in an Al-0.9% Cu-1.4% Mg alloy, Acta Mater. 48 (2000) 2751–2764. https://doi.org/10.1016/S1359-6454(99)00422-X.

[8] S.C. Wang, M.J. Starink, N. Gao, Precipitation hardening in Al–Cu–Mg alloys revisited, Scr. Mater. 54 (2006) 287–291. https://doi.org/10.1016/j.scriptamat.2005.09.010.

[9] S.P. Ringer, T. Sakurai, I.J. Polmear, Origins of hardening in aged Al-Cu-Mg-(Ag) alloys, Acta Mater. 45 (1997) 3731–3744. https://doi.org/10.1016/S1359-6454(97)00039-6.

[10] A.K. Gupta, P. Gaunt, M.C. Chaturvedi, The crystallography and morphology of the S'-phase precipitate in an Al(CuMg) alloy, Philos. Mag. A Phys. Condens. Matter, Struct. Defects Mech. Prop. 55 (1987) 375–387. https://doi.org/10.1080/01418618708209875.

[11] J.M. Silcock, The structural ageing characteristics of Al-Cu-Mg alloys with copper-magnesium weight ratios of 7-1 and 2.2-1, J. Inst. Met. 89 (1961) 203–210.

[12] L. Reich, S.P. Ringer, K. Hono, Origin of the initial rapid age hardening in an Al-1.7 at.% Mg-1.1 at.% Cu alloy, Philos. Mag. Lett. 79 (1999) 639–648. https://doi.org/10.1080/095008399176689.

[13] L. Kovarik, S.A. Court, H.L. Fraser, M.J. Mills, GPB zones and composite GPB/GPBII zones in Al–Cu–Mg alloys, Acta Mater. 56 (2008) 4804–4815. https://doi.org/10.1016/j.actamat.2008.05.042.

[14] L. Kovarik, M.J. Mills, Structural relationship between one-dimensional crystals of Guinier–Preston–Bagaryatsky zones in Al–Cu–Mg alloys, Scr. Mater. 64 (2011) 999–1002. https://doi.org/10.1016/j.scriptamat.2011.01.033.

[15] L. Kovarik, M.J. Mills, Ab initio analysis of Guinier-Preston-Bagaryatsky zone nucleation in Al-Cu-Mg alloys, Acta Mater. 60 (2012) 3861–3872. https://doi.org/10.1016/j.actamat.2012.03.044.

[16] M.J. Starink, S.C. Wang, The thermodynamics of and strengthening due to co-clusters: General theory and application to the case of Al-Cu-Mg alloys, Acta Mater. 57 (2009) 2376–2389. https://doi.org/10.1016/j.actamat.2009.01.021.

[17] S.B. Wang, Z.R. Liu, S.L. Xia, J. Key, J.H. Chen, Tetragonal-prism-like Guinier–Preston–Bagaryatsky zones in an AlCuMg alloy, Mater. Charact. 132 (2017) 139–144. https://doi.org/10.1016/j.matchar.2017.08.014.

[18] C. Pan, Y. Yang, S. Wang, Y. Liu, S. Hu, Z. Wang, P. Shen, Atomistic building blocks of one-dimensional Guinier–Preston–Bagaryatsky zones in Al-Cu-Mg alloys, Mater. Des. 187 (2020) 108393. https://doi.org/10.1016/j.matdes.2019.108393.

[19] H. Perlitz, A. Westgren, The crystal structure of Al2CuMg, Ark. Kemi Miner. Geol. 16B (1943) 13.

[20] V. Radmilovic, R. Kilaas, U. Dahmen, G.J. Shiflet, Structure and morphology of S-phase precipitates in aluminum, Acta Mater. 47 (1999) 3987–3997. https://doi.org/10.1016/S1359-6454(99)00259-1.

[21] C.B. Zhang, W. Sun, H.Q. Ye, Investigation of the crystallography and morphology of the s' precipitate in an Al(Cumg) alloy by hrem, Philos. Mag. Lett. 59 (1989) 265–271. https://doi.org/10.1080/09500838908206354.

[22] G.B. Winkelman, K. Raviprasad, B.C. Muddle, Orientation relationships and lattice matching for the S phase in Al-Cu-Mg alloys, Acta Mater. 55 (2007) 3213–3228. https://doi.org/10.1016/j.actamat.2007.01.011.

[23] Z.R. Liu, J.H. Chen, S.B. Wang, D.W. Yuan, M.J. Yin, C.L. Wu, The structure and the properties of S-phase in AlCuMg alloys, Acta Mater. 59 (2011) 7396–7405. https://doi.org/10.1016/j.actamat.2011.08.009.

[24] J. Majimel, G. Molénat, F. Danoix, D. Blavette, G. Lapasset, M.J. Casanove, A study of the hardening precipitation in a 2650 aluminium alloy for aeronautics, Mater. Sci. Forum. 396–402 (2002) 1025–1030. https://doi.org/10.4028/www.scientific.net/msf.396-402.1025.

[25] J. Majimel, G. Molenat, F. Danoix, O. Thuillier, D. Blavette, G. Lapasset, M.J. Casanove, High-resolution transmission electron microscopy and tomographic atom probe studies of the hardening precipitation in an Al-Cu-Mg alloy, Philos. Mag. 84 (2004) 3263–3280. https://doi.org/10.1080/14786430412331283983.

[26] L. Kovarik, M.K. Miller, S.A. Court, M.J. Mills, Origin of the modified orientation relationship for S(S'')-phase in Al-Mg-Cu alloys, Acta Mater. 54 (2006) 1731–1740. https://doi.org/10.1016/j.actamat.2005.11.045.

[27] J.K. Sunde, D.N. Johnstone, S. Wenner, A.T.J. van Helvoort, P.A. Midgley, R. Holmestad, Crystallographic relationships of T-/S-phase aggregates in an Al–Cu–Mg–Ag alloy, Acta Mater. 166 (2019) 587–596. https://doi.org/10.1016/j.actamat.2018.12.036.

[28] S.C. Wang, M.J. Starink, Two types of S phase precipitates in Al-Cu-Mg alloys, Acta Mater. 55 (2007) 933–941. https://doi.org/10.1016/j.actamat.2006.09.015.

[29] M.J. Styles, C.R. Hutchinson, Y. Chen, A. Deschamps, T.J. Bastow, The coexistence of two S (Al 2CuMg) phases in Al-Cu-Mg alloys, Acta Mater. 60 (2012) 6940–6951. https://doi.org/10.1016/j.actamat.2012.08.044.

[30] M.M.J. Treacy, Z dependence of electron scattering by single atoms into annular dark-field detectors, Microsc. Microanal. 17 (2011) 847–858. https://doi.org/10.1017/S1431927611012074.

[31] S.J. Andersen, C.D. Marioara, J. Friis, R. Bjørge, Q. Du, I.G. Ringdalen, S. Wenner, E.A. Mørtsell, R. Holmestad, T. Saito, J. Røyset, O. Reiso, Directionality and column arrangement principles of precipitates in Al-Mg-Si-(Cu) and Al-Mg-Cu linked to line defect in Al, Mater. Sci. Forum. 877 (2017) 461–470. https://doi.org/10.4028/www.scientific.net/MSF.877.461.

[32] G. Kresse, J. Hafner, Ab initio molecular dynamics for liquid metals, Phys. Rev. B. 47 (1993) 558–561. https://doi.org/10.1103/PhysRevB.47.558.

[33] G. Kresse, J. Furthmüller, Efficiency of ab-initio total energy calculations for metals and semiconductors using a plane-wave basis set, Comput. Mater. Sci. 6 (1996) 15–50. https://doi.org/10.1016/0927-0256(96)00008-0.

[34] J.P. Perdew, K. Burke, M. Ernzerhof, Generalized Gradient Approximation Made Simple, Phys. Rev. Lett. 77 (1996) 3865–3868. https://doi.org/10.1103/PhysRevLett.77.3865.

[35] H.J. Monkhorst, J.D. Pack, Special points for Brillouin-zone integrations, Phys. Rev. B. 13 (1976) 5188–5192. https://doi.org/10.1103/PhysRevB.13.5188.

[36] P.E. Blöchl, Projector augmented-wave method, Phys. Rev. B. 50 (1994) 17953–17979. https://doi.org/10.1103/PhysRevB.50.17953.

[37] C.D. Marioara, W. Lefebvre, S.J. Andersen, J. Friis, Atomic structure of hardening precipitates in an Al–Mg–Zn–Cu alloy determined by HAADF-STEM and first-principles calculations: relation to η-MgZn2, J. Mater. Sci. 48 (2013) 3638–3651. https://doi.org/10.1007/s10853-013-7158-3.

[38] V.A. Esin, L. Briez, M. Sennour, A. Köster, E. Gratiot, J. Crépin, Precipitation-hardness map for Al–Cu–Mg alloy (AA2024-T3), J. Alloys Compd. 854 (2021) 157164. https://doi.org/10.1016/j.jallcom.2020.157164.

[39] F.J. Niu, J.H. Chen, S.Y. Duan, W.Q. Ming, J.B. Lu, C.L. Wu, Z. Le, The effect of pre-deformation on the precipitation behavior of AlCuMg(Si) alloys with low Cu/Mg ratios, J. Alloys Compd. 823 (2020). https://doi.org/10.1016/j.jallcom.2020.153831.

[40] Y.L. Zhao, Z.Q. Yang, Z. Zhang, G.Y. Su, X.L. Ma, Double-peak age strengthening of cold-worked 2024 aluminum alloy, Acta Mater. 61 (2013) 1624–1638. https://doi.org/10.1016/j.actamat.2012.11.039.

[41] Z. Feng, X. Luo, Y. Chen, N. Chen, G. Wu, Surface severe plastic deformation induced solute and precipitate redistribution in an Al-Cu-Mg alloy, J. Alloys Compd. 773 (2019) 585–596. https://doi.org/10.1016/j.jallcom.2018.09.226.

[42] J.L. García-Hernández, C.G. Garay-Reyes, I.K. Gómez-Barraza, M.A. Ruiz-Esparza-Rodríguez, E.J. Gutiérrez-Castañeda, I. Estrada-Guel, M.C. Maldonado-Orozco, R. Martínez-Sánchez, Influence of plastic deformation and Cu/Mg ratio on the strengthening mechanisms and precipitation behavior of AA2024 aluminum alloys, J. Mater. Res. Technol. 8 (2019) 5471–5475. https://doi.org/10.1016/j.jmrt.2019.09.015.

[43] Z. Wang, M. Chen, H. Jiang, H. Li, S. Li, Effect of artificial ageing on strength and ductility of an Al-Cu-Mg-Mn alloy subjected to solutionizing and room-temperature rolling, Mater. Charact. 165 (2020) 110383. https://doi.org/10.1016/j.matchar.2020.110383.

[44] Y. Liu, F. Teng, F.H. Cao, Z.X. Yin, Y. Jiang, S.B. Wang, P.K. Shen, Defective GP-zones and their evolution in an Al-Cu-Mg alloy during high-temperature aging, J. Alloys Compd. 774 (2019) 988–996. https://doi.org/10.1016/j.jallcom.2018.10.061.

[45] S.J. Andersen, C.D. Marioara, J. Friis, S. Wenner, R. Holmestad, Precipitates in aluminium alloys, Adv. Phys. X. 3 (2018) 790–814. https://doi.org/10.1080/23746149.2018.1479984.

[46] X. Chen, C.D. Marioara, S.J. Andersen, J. Friis, A. Lervik, R. Holmestad, E. Kobayashi, Data on first-principles calculations of various precipitates and microstructure characterizations in an Al-Mg-Cu alloy [Unpublished manuscript], Data Br. (2021).

[47] S.B. Wang, J.H. Chen, M.J. Yin, Z.R. Liu, D.W. Yuan, J.Z. Liu, C.H. Liu, C.L. Wu, Double-atomic-wall-based dynamic precipitates of the early-stage S-phase in AlCuMg alloys, Acta Mater. 60 (2012) 6573–6580. https://doi.org/10.1016/j.actamat.2012.08.023.

[48] Y. Liu, X. Han, S. Wang, B. Wei, W. Li, Subtle atomistic processes of S-phase formation in Al-Cu-Mg alloys, J. Alloys Compd. 838 (2020) 155677. https://doi.org/10.1016/j.jallcom.2020.155677.

[49] P.G. Shewmon, Diffusion in Solids, McGraw-Hill, New York, 1963.

[50] H.W. Zandbergen, Structure Determination of Mg5Si6 Particles in Al by Dynamic Electron Diffraction Studies, Science. 277 (1997) 1221–1225. https://doi.org/10.1126/science.277.5330.1221.

[51] T. Saito, E.A. Mørtsell, S. Wenner, C.D. Marioara, S.J. Andersen, J. Friis, K. Matsuda, R. Holmestad, Atomic Structures of Precipitates in Al–Mg–Si Alloys with Small Additions of Other Elements, Adv. Eng. Mater. 20 (2018) 1–18. https://doi.org/10.1002/adem.201800125.

[52] K. Matsuda, A. Kawai, K. Watanabe, S. Lee, C.D. Marioara, S. Wenner, K. Nishimura, T. Matsuzaki, N. Nunomura, T. Sato, R. Holmestad, S. Ikeno, Effect of

copper on fine precipitates at the early stage of aging in Al-Mg-X (X=Si, Ge, Zn) alloys, Keikinzoku/Journal Japan Inst. Light Met. 67 (2017) 186–192. https://doi.org/10.2464/jilm.67.186.

[53] S.J. Andersen, C.D. Marioara, A. Frøseth, R. Vissers, H.W. Zandbergen, Crystal structure of the orthorhombic U2-Al4Mg4 Si4 precipitate in the Al-Mg-Si alloy system and its relation to the β′ and β″ phases, Mater. Sci. Eng. A. 390 (2005) 127–138. https://doi.org/10.1016/j.msea.2004.09.019.

[54] E. Thronsen, C.D. Marioara, J.K. Sunde, K. Minakuchi, T. Katsumi, I. Erga, S.J. Andersen, J. Friis, K. Marthinsen, K. Matsuda, R. Holmestad, The effect of heavy deformation on the precipitation in an Al-1.3Cu-1.0Mg-0.4Si wt.% alloy, Mater. Des. 186 (2020) 108–203. https://doi.org/10.1016/j.matdes.2019.108203.

[55] M. Gazizov, C.D. Marioara, J. Friis, S. Wenner, R. Holmestad, R. Kaibyshev, Unique hybrid precipitate structures forming in an Al–Cu–Mg–Si alloy, J. Alloys Compd. 826 (2020) 153977. https://doi.org/10.1016/j.jallcom.2020.153977.

[56] M. Gazizov, C.D. Marioara, J. Friis, S. Wenner, R. Holmestad, R. Kaibyshev, Precipitation behavior in an Al–Cu–Mg–Si alloy during ageing, Mater. Sci. Eng. A. 767 (2019) 138369. https://doi.org/10.1016/j.msea.2019.138369.

Table 3.1. Chemical composition of the investigated Al alloy in mass and atomic percent.

Element	Mg	Cu	Si	Fe	Al
wt.%	3.04	1.01	0.01	0.01	Bal.
at.%	3.38	0.43	0.01	0.005	Bal.

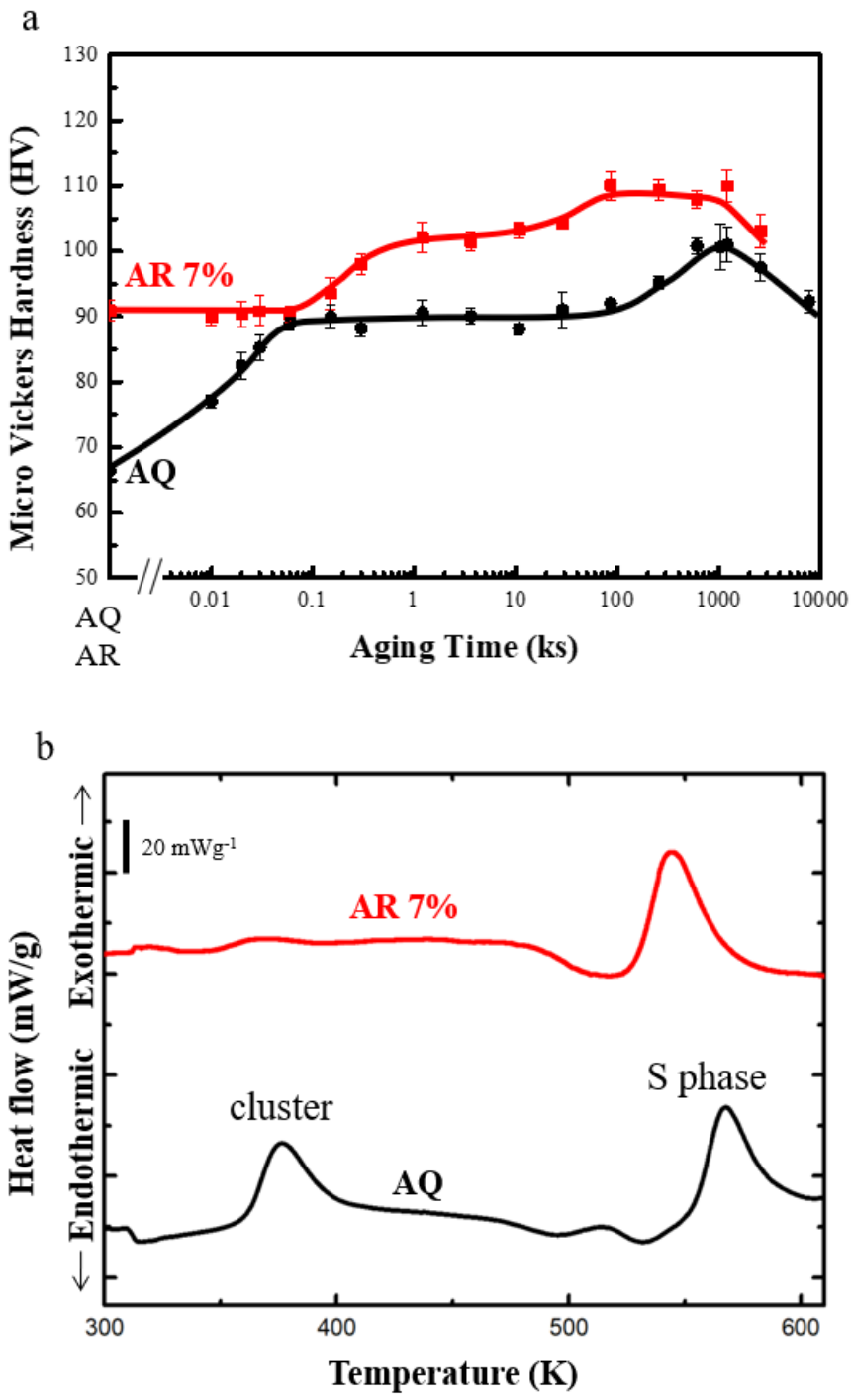

Fig. 3.1. (a) The age-hardening curves at 443 K for the as-quenched (AQ) and as-rolled (AR) Al-3Mg-1Cu samples. (b) DSC curves of the AQ and AR samples.

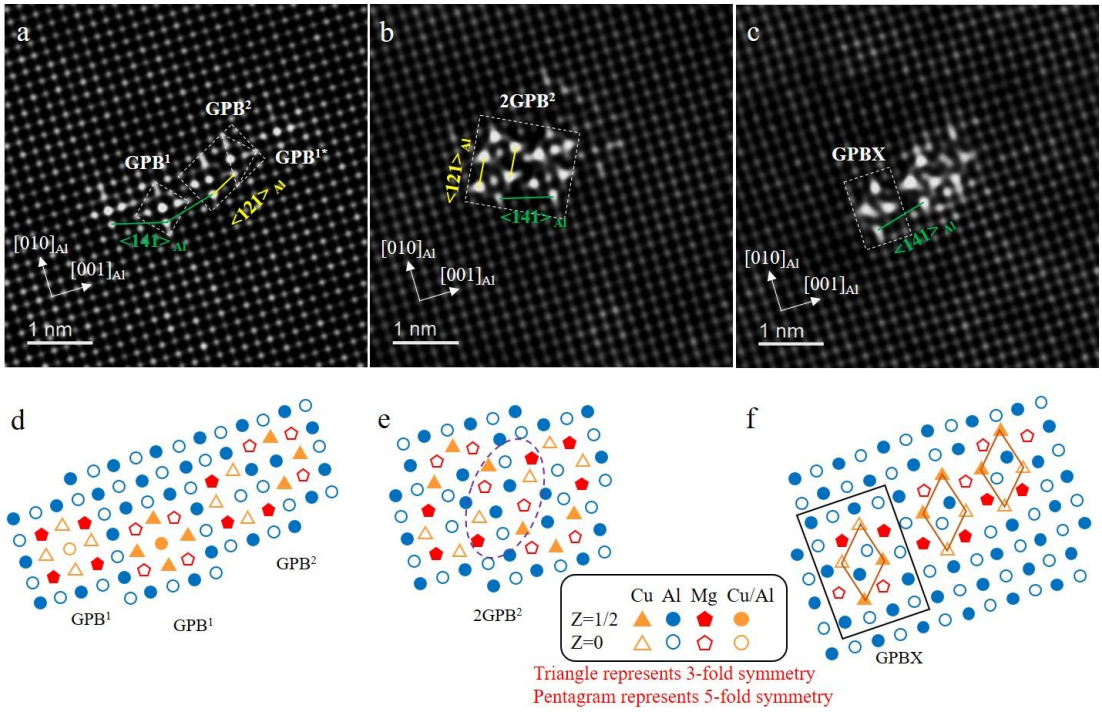

Fig. 3.2. HAADF-STEM images of the AR sample aged at 443K for 20 min (a-c) and the corresponding atomic structures of GPB zones (d-f). (a)(d) GPB^1 and GPB^2 zones, (b)(e) $2GPB^2$ zone, (c)(f) GPBX zones.

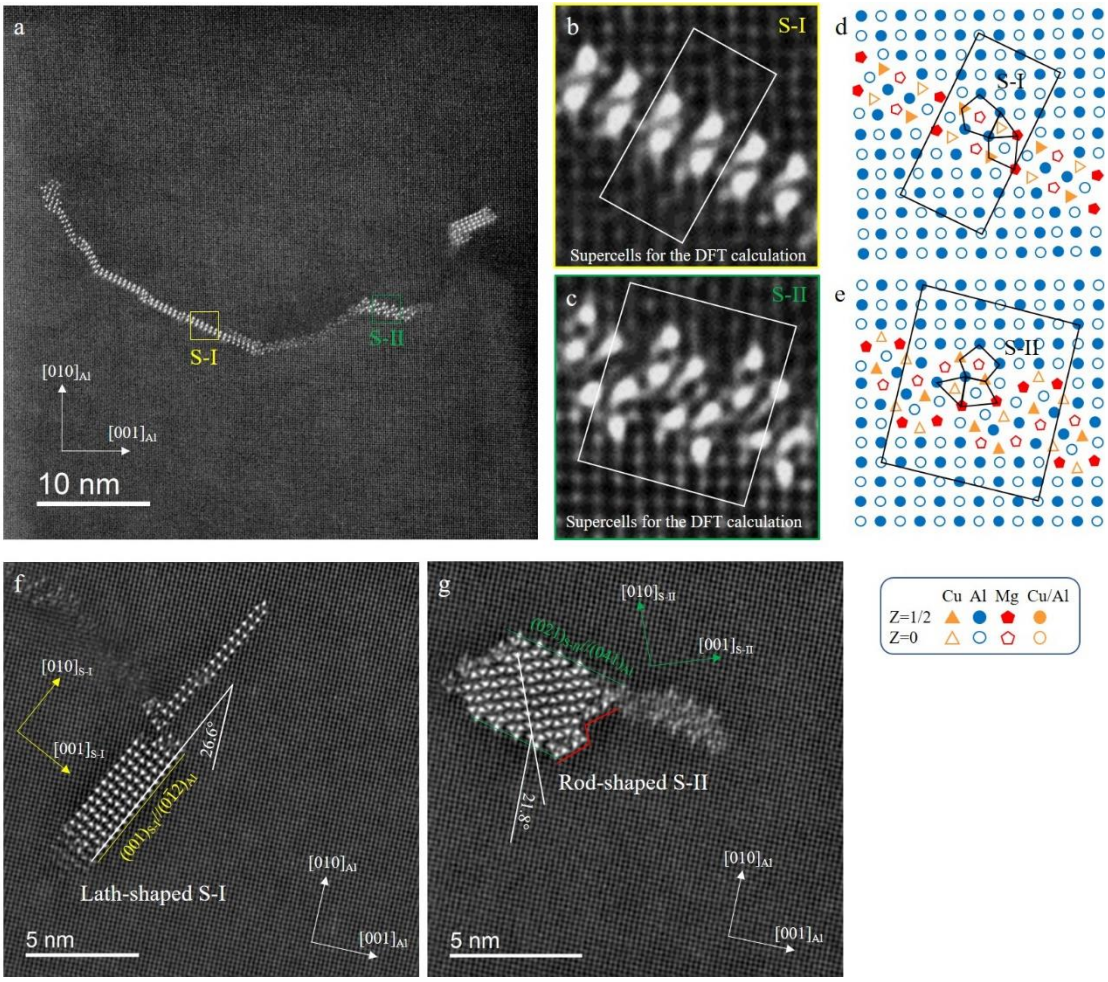

Fig. 3.3. HAADF-STEM images and atomic models of two types of S phase formed on dislocation lines in the AR sample aged at 443 K for 1 day. (a) Overview: The two phases on the same dislocation. (b) and (c): Magnified images of the precipitates in (a), superposed with the supercells for the DFT calculations. (d) and (e): Corresponding atomic models of the S-I and S-II phase. (f) and (g) Examples of coarser precipitates.

Table 3.2. The input coordinates for the atomic models for the supercells containing the GPBX zone, the S-I, and S-II phases. GPBX is described as a bulk phase, the two others are embedded in the matrix (cf. Fig. 3.2(b) and (c)), given with surrounding layers of aluminum.

	GPBX zone			**S-I phase**			**S-II phase**		
	a = 6.75 Å, b = 4.05 Å, c = 7.94 Å α = 90.0°, β = 90.0°, γ = 90.0°			a = 18.85 Å, b = 4.05 Å, c = 9.06 Å α = 90.0°, β = 90.0°, γ = 90.0°			a = 19.21 Å, b = 4.05 Å, c = 16.70 Å α = 90.0°, β = 94.4°, γ = 90.0°		
Atoms	**x**	**y**	**z**	**x**	**y**	**z**	**x**	**y**	**z**
Al	0.139	0.25	0.068	0	0	0	0	0	0
Al				0	0.5	0.5	0.0253	0	0.3846
Al				0.048	0	0.3	0.0513	0	0.7692
Al				0.2402	0.5	0	0.0769	0	0.1538
Al				0.096	0.5	0.1	0.1026	0	0.5385
Al				0.1922	0	0.2	0.1279	0	0.9231
Al				0.1441	0.5	0.4	0.1538	0	0.3077
Al				0.2882	0.5	0.3	0.1795	0	0.6923
Al				0.3363	0	0.1	0.2051	0	0.0769
Al				0.488	0	0.141	0.3077	0	0.6154
Al							0.369	0	0.87
Al							0.42	0	0.718
Al							0.43	0	0.475
Mg	0.034	0.25	0.673	0.396	0	0.391	0.2415	0	0.459
Mg							0.292	0	0.245
Mg							0.47	0	0.1
Cu	0.261	0.25	0.38	0.411	0.5	0.18	0.235	0	0.839
Cu							0.3333	0	0.017
Cu							0.447	0	0.32

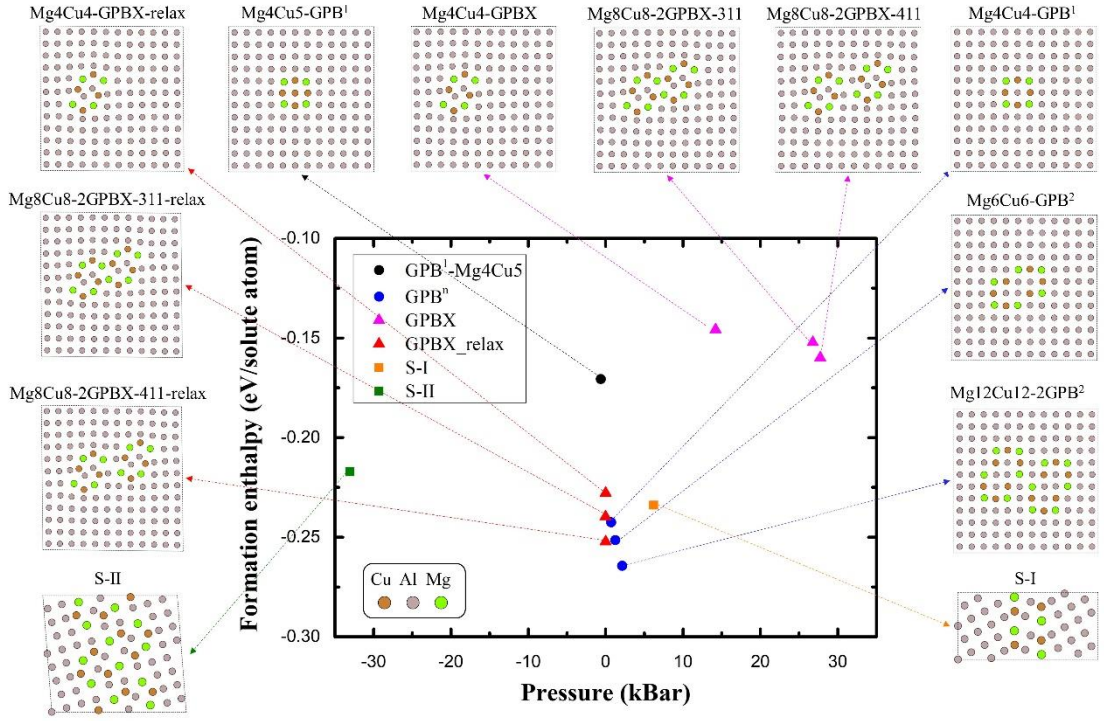

Fig. 3.4. Calculated formation enthalpy per solute atom for GPB zones and S phases embedded in the Al matrix, plotted against pressure. All models are shown in $<001>_{Al}$ orientation. GPB zones are embedded in 6 x 6 x 1 Al cells and are continuous needles in the viewing direction.

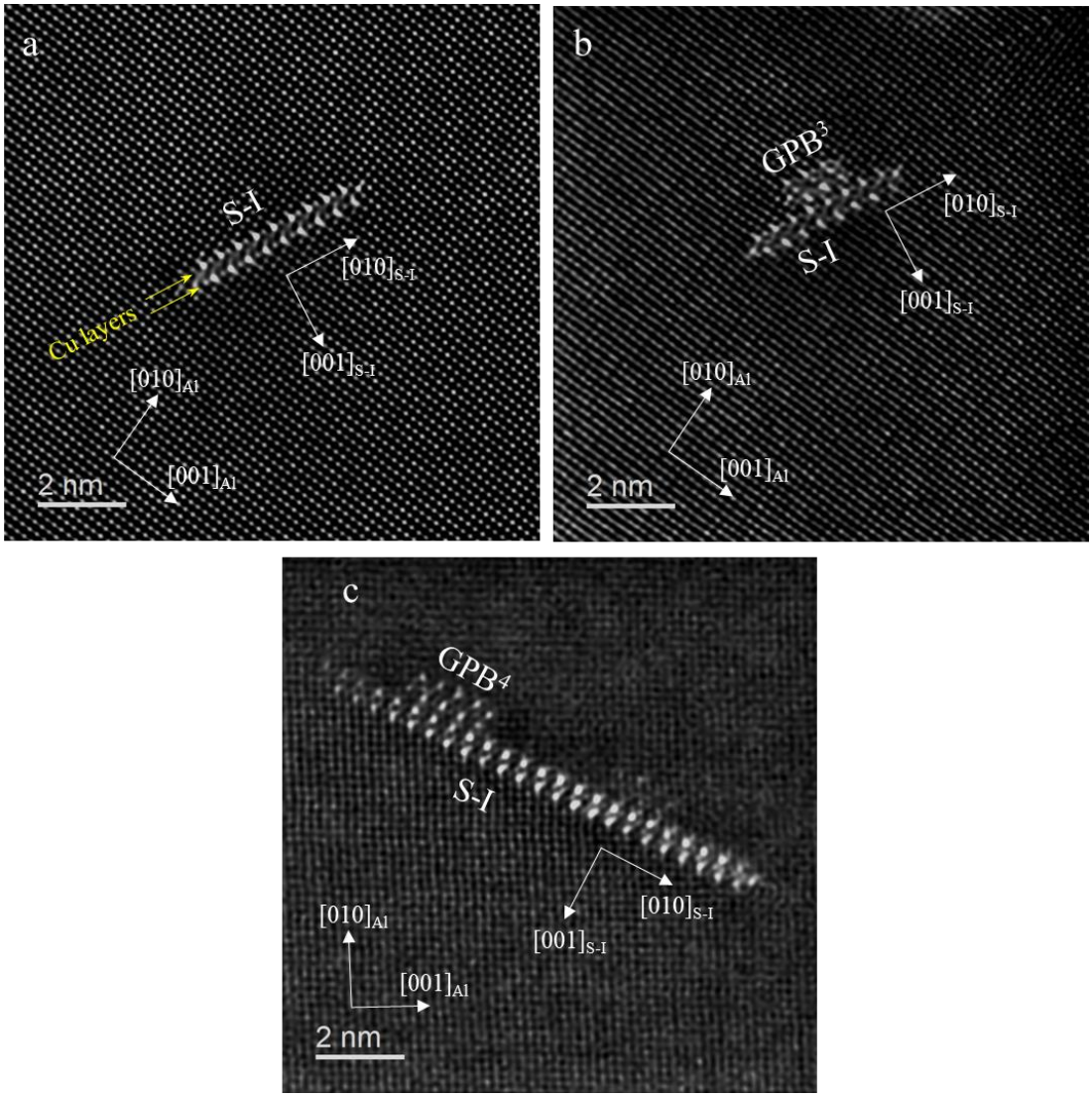

Fig. 3.5. HAADF-STEM images of (a)(b) non-deformed samples aged for 8 hours and (c) AR samples aged for 1 day at 443 K. (a) $<021>_{Al}$ orientated S-I phase. (b) S-I phase with GPB^3 zone on side, growing along $[010]_{S-I}$. (c) S-I phase and GPB^4 zone, which can be considered as the elongated version of (b).

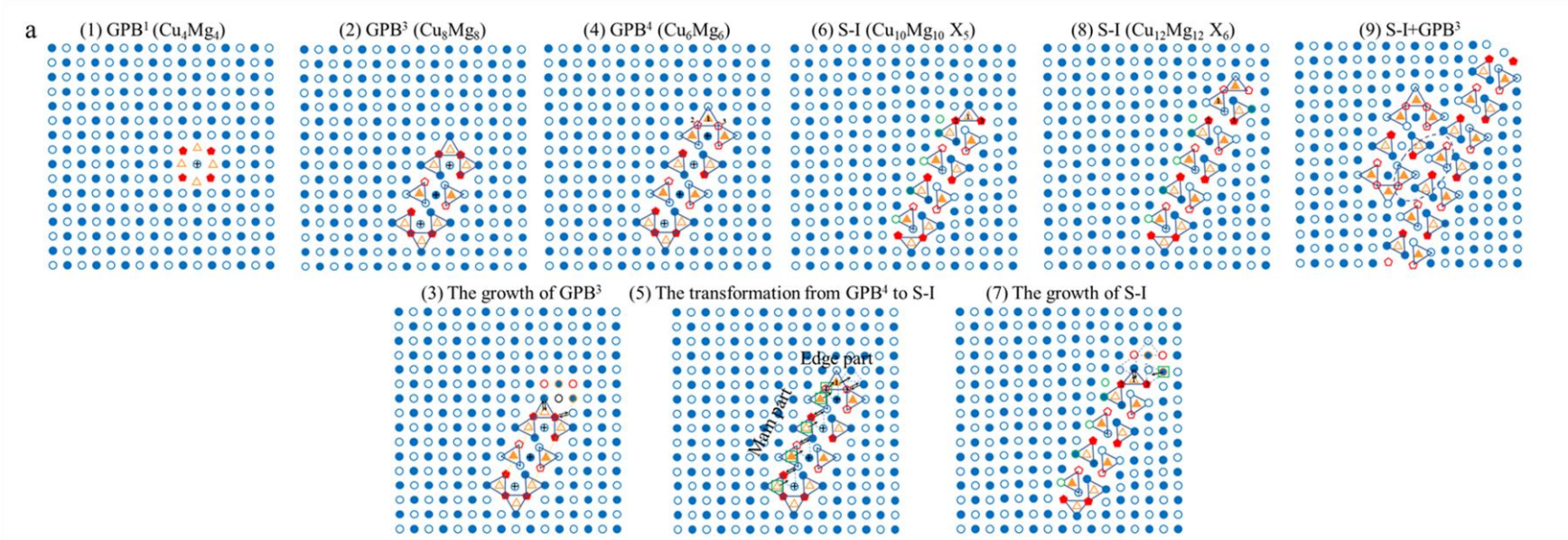

Fig. 3.6. Schematics showing GPB-zones embedded in the matrix, and suggested atomic displacement steps regarding their structural evolution and transformation to S phases. (a) GPBn zone growth, transformation to S-I phase, and S-I phase growth. (b) GPBX zone and S-II phase formation as well as the S-II phase growth. (c) Dislocations attracting Cu and Mg by generating preferred positions. In (a) and (b), the upper rows show various precipitate structures, the lower rows show the transformation or growth processes between different structures. The components of each structure are also noted, where “Xn” means the number of generated vacancies.

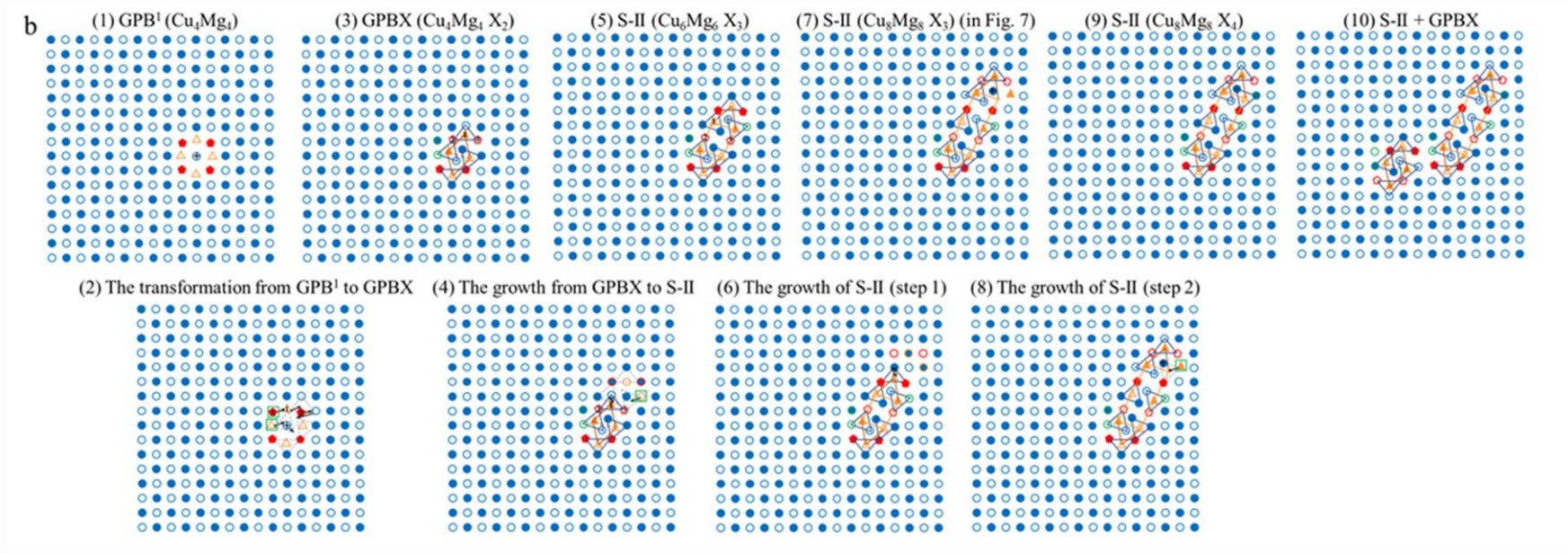

Fig. 3.6. Schematics showing GPB-zones embedded in the matrix, and suggested atomic displacement steps regarding their structural evolution and transformation to S phases. (a) GPBn zone growth, transformation to S-I phase, and S-I phase growth. (b) GPBX zone and S-II phase formation as well as the S-II phase growth. (c) Dislocations attracting Cu and Mg by generating preferred positions. In (a) and (b), the upper rows show various precipitate structures, the lower rows show the transformation or growth processes between different structures. The components of each structure are also noted, where “Xn” means the number of generated vacancies.

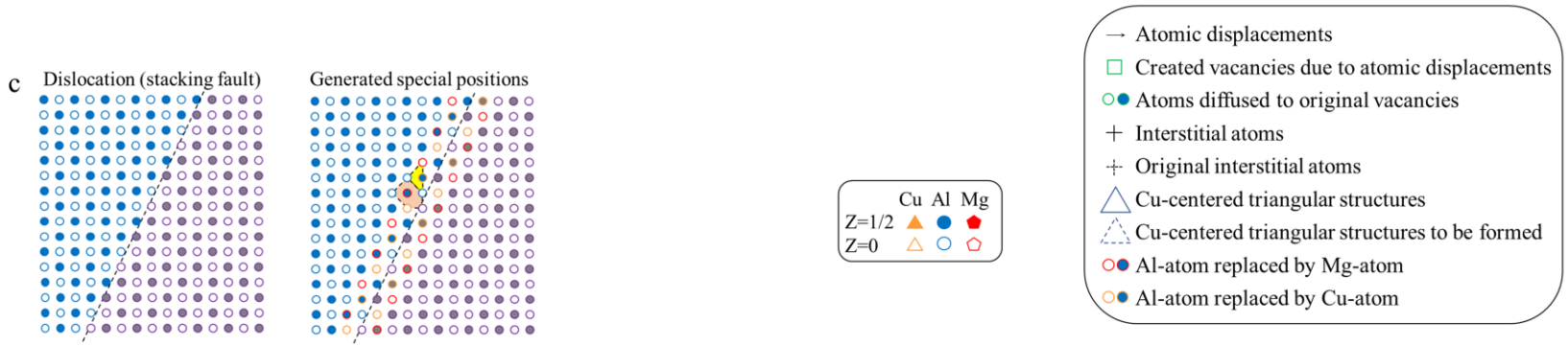

Fig. 3.6. Schematics showing GPB-zones embedded in the matrix, and suggested atomic displacement steps regarding their structural evolution and transformation to S phases. (a) GPBn zone growth, transformation to S-I phase, and S-I phase growth. (b) GPBX zone and S-II phase formation as well as the S-II phase growth. (c) Dislocations attracting Cu and Mg by generating preferred positions. In (a) and (b), the upper rows show various precipitate structures, the lower rows show the transformation or growth processes between different structures. The components of each structure are also noted, where “Xn” means the number of generated vacancies.

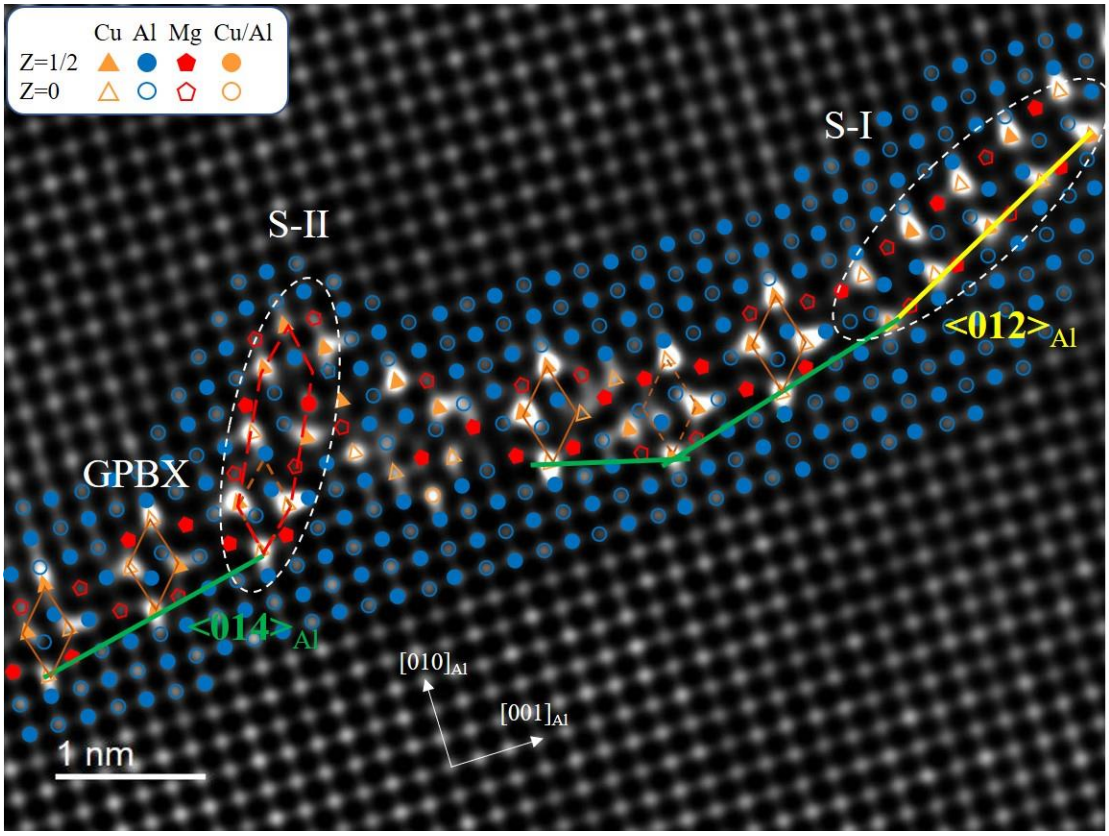

Fig. 3.7. HAADF-STEM image in $[100]_{Al}$ orientation, with atomic overlay of precipitates along dislocation line in the AR samples aged for 20 min at 443 K revealing periodic nucleation of GPBX zones along $<114>_{Al}$ and two types of S phases.

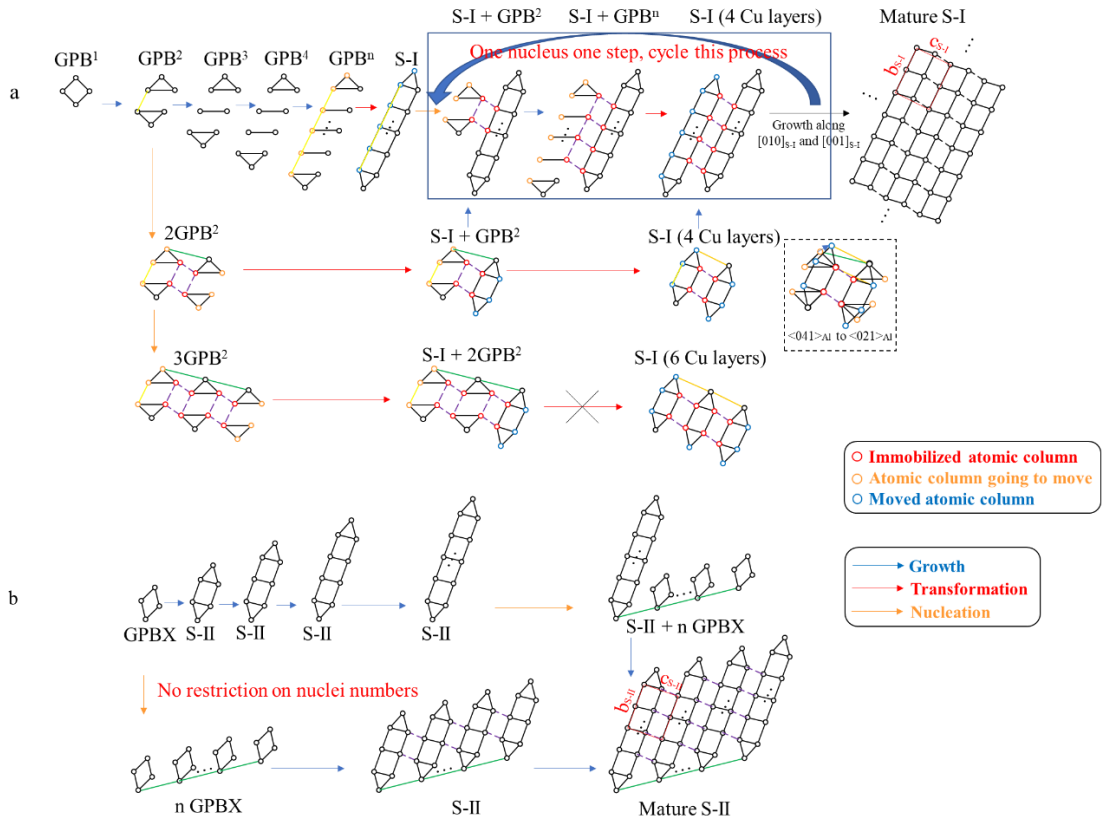

Fig. 3.8. Simplified schematics of the precipitation processes, showing the formation and growth of (a) S-I and (b) S-II phases in a <100>$_{Al}$ projection, in terms of the Cu-columns only. (a) The precipitation process from GPB^1 zone to mature S-I phase. (b) The precipitation process from GPBX zone to mature S-II phase.

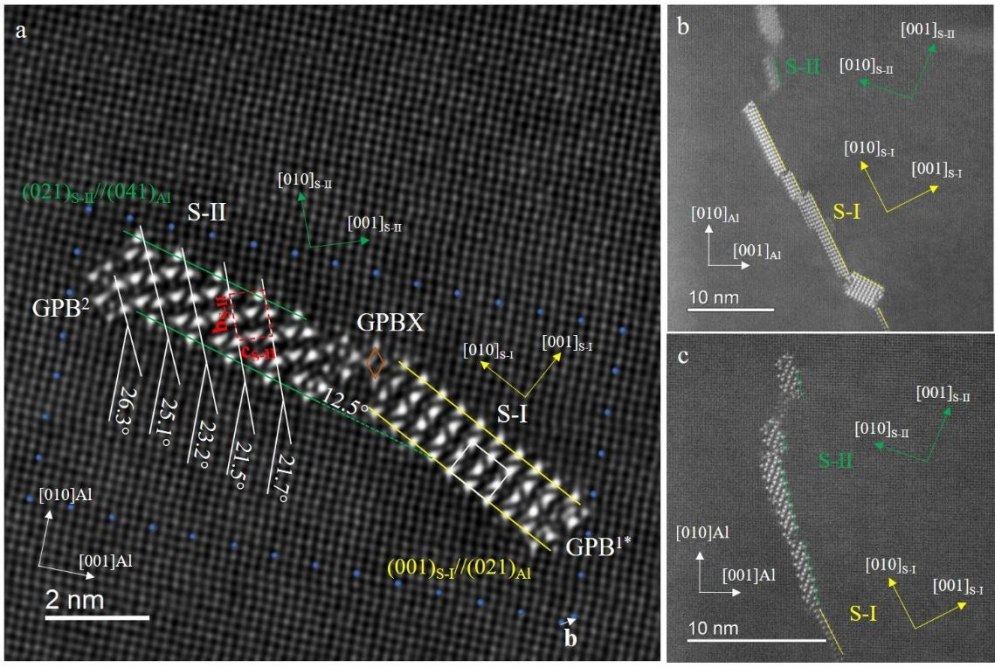

Fig. 3.9. HAADF-STEM images with two types of S phases coexisting on dislocations in the AR sample aged at 443 K for 1 day. (a) Close-up showing S-II structure deforms by increasing rotation of the $[010]_{S\text{-}II}$ direction towards left end (where a dislocation is located). A Burger's loop reveals there is a dislocation ($\vec{b}$). (b) Disconnected S-I precipitates on dislocation line, with parallel cross-sections along $[010]_{S\text{-}II}//<021>_{Al}$. (c) S-II on dislocation with cross-section elongations near $<041>_{Al}$.

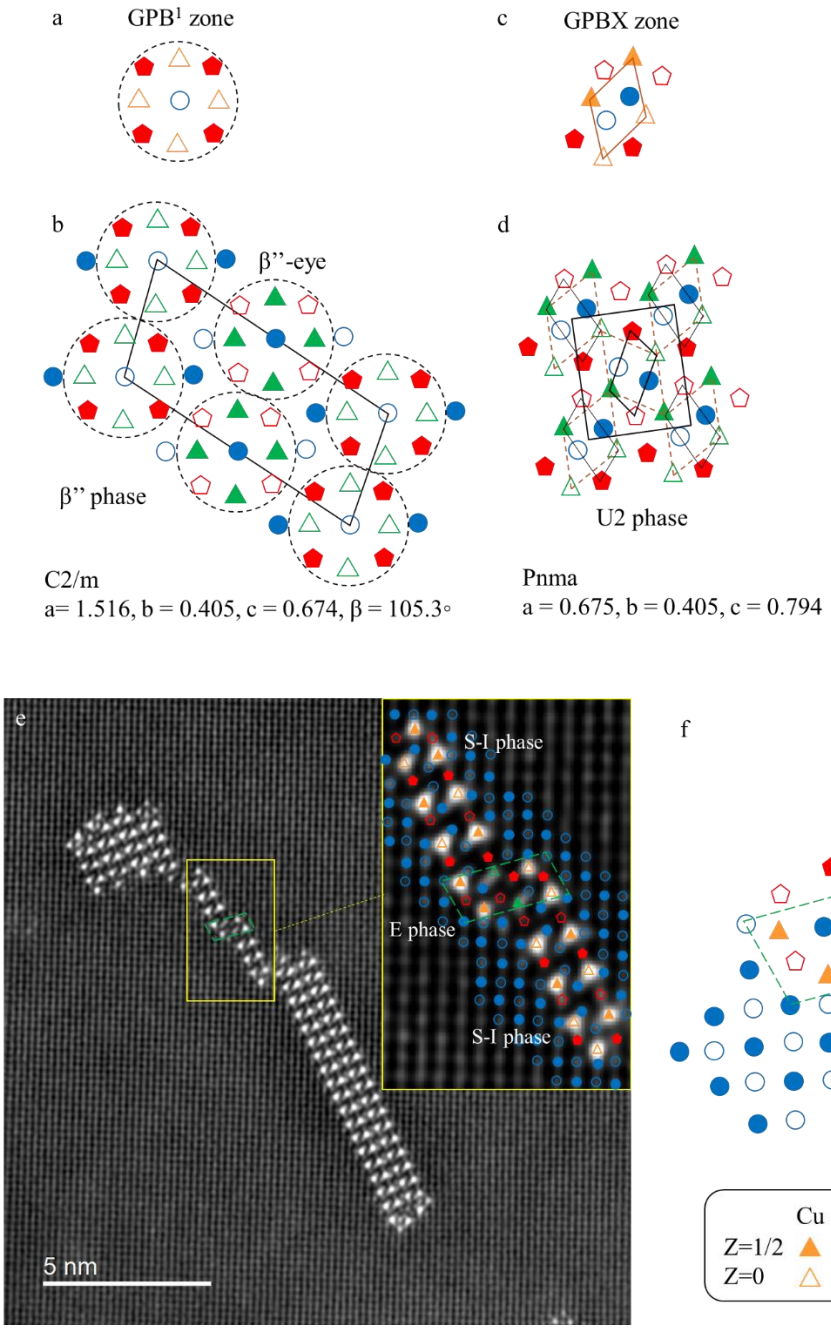

Fig. 3.10. Atomic models (a-d, f) and HAADF-STEM image (e) of selected precipitates. (a) GPB[1] zone, (b) β'' phase, (c) GPBX zone, (d) U2 phase, and (f) E phase. (e) HAADF-STEM image of S-I and E phases in the AR sample aged at 443 K for 1 day, with the partial atomic overlay.

Chapter 4. Enhanced mechanical properties in an Al-Mg-Cu alloy processed by the combination of cyclic deformation and aging heat treatment

4.1 Introduction

The most common strengthening method for heat-treatable aluminum alloys is aging heat treatment, during which fine precipitates providing lattice strain around them are formed to hinder the movement of dislocations, thus increasing the strength. Al-Mg-Cu alloys have been extensively studied owing to their rapid age-hardening behavior [1–6]. The general precipitation sequence for S phases in Al-Mg-Cu alloys is [7–16]:

SSSS → Cu/Mg clusters → GPB zones → S' phases → S phases (1)

SSSS refers to a supersaturated solid solution obtained by solution heat treatment (SHT) followed by quenching. Supersaturated solute atoms tend to precipitate from the Al matrix into equilibrium S phases during aging. Cu/Mg nanoclusters form within 1 min by aging at 443 K and contribute approximately 65% of the total increase in hardness [5,6]. The Guinier–Preston–Bagaryatsky (GPB) zone is considered to be a short-range ordering of Cu and Mg solute atoms. There are many types of GPB zones. In addition to normal GPB zones such as GPB^1 and GPB^2, novel GPB zones with different structures have also been reported [17–22]. The S' phase is considered to be the cause of the peak hardness and a slightly strained version of the equilibrium S phase [23]. In this work, the S' and S phases were not distinguished, because S' and S have similar lattice parameters and the same composition as Al_2CuMg [24]. The S phases are classified into orthorhombic lath-shaped S-I phase and monoclinic rod-shaped S-II phase [17,25–27].

Another common strengthening method is introducing dislocations through plastic deformation to induce a work-hardening effect [28–36]. The hardness of Al-Mg-Cu alloy could be increased from 66.4 to 121.8 HV by 50% of deformation during cold rolling [6]. The introduced dislocations significantly promoted the subsequent aging process; however, almost no clusters were generated during the deformation. Recently,

Sun et al. proposed a cyclic strengthening (CS) method by applying alternating stress to induce back-and-forth dislocation movement at room temperature (RT) [37]. This method can achieve both work-hardening and precipitation-strengthening by introducing dislocations and promoting cluster formation. Furthermore, it was pointed out that CS could improve the fatigue properties of Al alloys [38]. Moreover, the CS effect was also observed even in non-heat-treatable Al-Mg alloys [39]. These advantages have made CS a topic of great significance.

The rapid formation of clusters characterizes the aforementioned Al-Mg-Cu alloy; therefore, the CS effect is expected to be significant and can be completed in a very short time. Moreover, the precipitation process of this alloy is simple and clear, and strain-induced dissolution of GPB zones does not occur during deformation [40]. These characteristics make the alloy suitable for systematic research on how cyclic deformation and aging correlate and interact, deepening the understanding of the strengthening mechanism.

In this study, the CS effects in Al–Mg–Cu alloys with and without pre-aging were studied. The aging behaviors and strengthening mechanisms of the cyclically strengthened samples with and without pre-aging were also investigated. Finally, through the combination of cyclic deformation and aging, we achieved higher strength than that obtained by cyclic deformation or aging alone.

4.2 Experimental methods

Table 4.1 lists the chemical compositions of the investigated high-purity Al-Mg-Cu alloy. The material was supplied by the UACJ Corporation. The specimens were machined from the extruded bars to the shape shown in Fig. 4.1(a). The specimens were solution-heat-treated in a salt bath at 793 K for 1 h, followed by quenching in water at room temperature, where they were held for 1 min. These steps were to obtain a uniform supersaturated solid solution as the basis for subsequent experiments. The as-quenched condition is abbreviated as “AQ”. The AQ samples were subjected to cyclic deformation and aging heat treatment, as shown in Figs. 4.1(b-f). The samples were named according to their distinct processing history. For clarity, the cyclically-strengthened sample is called “CS”; the artificially aged sample is called “AA”; artificial aging (pre-aging) followed by cyclic deformation is called “AA+CS”; cyclic deformation followed by subsequent artificial aging is called “CS+AA”; and cyclic

deformation between two artificial aging treatments (pre-aging and subsequent aging) is called “AA+CS+AA”. Note that all the artificial aging treatments were completed at 443 K, except for aging at RT, 343 K, and 393 K, as shown in Fig. 4.6(c).

Isothermal aging was performed in an oil bath at different temperatures for various durations. The peak-aged (PA) condition at 443 K was determined to be aging for 14 d, as shown in Fig. S4.1 (Supplementary Material). Cyclic plastic deformation was conducted at room temperature using a Shimazu Servopulser EHF-EA5 using fully reversed tension-compression cycles (a strain ratio of R = -1) with a sinusoidal waveform. After the preliminary tests to fix the deformation parameters, 500 cycles, a frequency of 1 Hz, and a strain amplitude of 5.5×10^{-3} were selected as the standard conditions. The details of the cyclic deformation are provided in the Supplementary Material.

The Vickers hardness was measured at RT by applying a load of 200 g for 15 s in a MATSUZAWA SERIES MMT-X microhardness tester. The reported hardness values were the average of five out of seven hardness data points, excluding the two extremal values.

An Autograph AG-X plus tester manufactured by Shimadzu was used for uniaxial tensile experiments. The tests were conducted at RT at a strain rate of 1.39×10^{-3} s^{-1}. The direction of the tensile test was parallel to the cyclic deformation direction. At least three tensile specimens were tested for each condition, yielding reproducible results. The average values and errors were calculated from the results.

Differential scanning calorimetry (DSC) was performed under argon flow in a Rigaku DSC8230 instrument at a constant heating rate of 0.167 K/s. A 40 mg sample of Al (99.999 % of purity) was used as a reference. The temperature was controlled from 223 K to 773 K using a liquid nitrogen controller.

Specimens for transmission electron microscopy (TEM) were obtained from the gauge sections of the specimens shown in Fig. 4.1(a). Most of the specimens (blue) were cut perpendicular to the cyclic deformation/tensile test direction, except for one sample (orange, shown in Fig. 4.8(d)), which was cut parallel to the direction. The cut specimens were first ground to a thickness of approximately 100 μm, from which they were punched into disks 3 mm in diameter. Subsequently, the disks were electropolished using a Struers TenuPol-5 machine until perforation. The electrolyte

(1/3 nitric acid and 2/3 methanol) was maintained between 243 and 253 K during electropolishing, with an applied potential of 20 V. The microstructure (before the tensile test) was investigated using a JEM-2100F microscope operating at 200 kV. The electron beam was parallel to the $<001>_{Al}$ direction.

4.3 Results

4.3.1 Peak aging and cyclic strengthening

The stress-strain curves of the AQ, PA, and CS samples are shown in Fig. 4.2(a). Compared with AQ samples, the ultimate tensile strength (UTS) of PA and CS samples increased from 241.2 to 311.6 and 327.6 MPa, respectively, indicating that precipitation strengthening and cyclic strengthening were both effective strengthening methods. However, their elongation decreased from 59.7% to 35.7% and 43.4%, respectively. The CS samples had both higher strength and ductility than PA samples. Furthermore, CS only required approximately 10 min (which could be further shortened, as discussed in the Supplementary Material) at RT, while PA required 443 K aging for 14 days. In short, CS is a method that can significantly reduce time and energy consumption to achieve good mechanical properties.

The DSC results are shown in Fig. 4.2(b). Exothermic peaks I, II, and III refer to the formation of clusters, GPB zones, and S phases, respectively, while endothermic peaks I', II', and III' refer to their dissolution [6,41,42]. Note that peak II was always obscured; therefore, the formation of GPB zones was difficult to track by DSC. Taking the DSC curve of the AQ samples as a benchmark for comparison, the area of peak III in the PA samples became smaller, meaning that the S phases were partially formed. In the CS samples, the area of peak I decreased, and peak III appeared at a lower temperature without a significant area change, indicating that the clusters have been partially formed and the subsequent aging process to form S phases would be accelerated. The process is discussed in detail later. The presence of S phases significantly reduces the ductility of materials [6]. Therefore, the absence of S phases in the CS samples resulted in a better ductility than that of the PA samples.

TEM was used to investigate why the strength of the CS samples was higher than that of the PA samples. A large number of dislocation lines (Fig. 4.3(a)) and loops (amplified in Fig. 4.3(b)) introduced by cyclic plastic deformation in the CS samples

were observed by bright-field scanning transmission electron microscopy (BF-STEM). No characteristic diffraction spots of GPB zones or S phases were found in Fig. 4.3(c). What was observed in high-resolution TEM (HRTEM, Fig. 4.3(d)) was thought to be nanoclusters; they were only the aggregate of solute atoms without a specific structure. In summary, the strength of CS was due to the contribution of clusters and dislocation lines and loops, consistent with a previous report [37].

4.3.2 Cyclic strengthening effect of pre-aged samples

Pre-aging was applied to the AQ samples to obtain precipitates and study their influence on the subsequent cyclic deformation. Pre-agings for 20 min and 14 d were selected because the clusters or GPB zones and S phases were formed, respectively. The tensile test results for the samples before and after cyclic strengthening are shown in Fig. 4.4(a). An increase in strength and decrease in ductility were observed in both the 20minAA and PA samples after CS.

The DSC curves are shown in Fig. 4.4(b). Peak III of the 20minAA+CS (CS on the 20 min pre-aged sample) and PA+CS samples appeared at lower temperatures than those of the 20minAA and PA samples, implying that CS could still promote subsequent precipitation, even though precipitates have been partially formed during pre-aging. The corresponding aging behaviors are discussed later.

BF-STEM images of the pre-aged CS samples are shown in Fig. 4.5. Dislocation lines and fine dislocation loops in the 20minAA+CS samples, as shown in Fig. 4.5(a), and the existence of GPB zones was confirmed by the selected area diffraction pattern (SADP), as indicated by the white arrows. The S phases elongated along the $<001>_{Al}$ direction, and dislocation lines and loops were observed in the PA+CS samples, as shown in Fig. 4.5(b). Many dislocation lines were tangled on the S phase, as shown in Fig. 4.5(c).

From the above results, it can be inferred that: (1) solute atoms in a supersaturated solid solution aggregate to form clusters or even transform into precipitates during pre-aging. Therefore, CS hardly brings about precipitation strengthening because no solute atoms remain to form new clusters after pre-aging. (2) The dislocation density in materials remains low even after pre-aging; therefore, the subsequent CS can still introduce a large number of dislocations to cause the work-hardening effect.

4.3.3 Aging behavior of cyclically-strengthened samples

The aging behaviors of AQ and CS samples aged at 443 K are shown in Fig. 4.6(a). The black hardness change curve for the AQ sample is typical for Al-Mg-Cu alloys [1]. Rapid age-hardening appeared first, followed by a long plateau in which the hardness remained constant. Finally, the second hardening occurred until the peak. The CS sample had a higher starting hardness than the AQ sample because of the cyclic strengthening effect discussed earlier. Its hardness decreased at the beginning of aging and then reached a plateau after aging for approximately 20 min. With further aging, the hardness increased until it reached its peak. It took 3 d to reach the hardness peak in the CS samples, much shorter than the 14 d required for AQ samples, consistent with the DSC results shown in Fig. 4.2(b). Moreover, the hardness of the CS samples was significantly higher than that of the AQ samples throughout the aging process.

From the DSC results shown in Fig. 4.6(b), it can be seen that after aging for 20 min (CS+20minAA), peak III did not change, indicating that no S phases had been formed yet. After 3 days of aging (CS+3dAA), peak III almost disappeared, implying that S phases were formed.

The aging behavior of the CS samples aged at various temperatures is shown in Fig. 4.6(c). The aging curve at 443 K showed a clear hardness peak. The hardness change slowed as the aging temperature decreased. Aging curves at 393 and 343 K remained in the incubation stage to form S phases after six months of aging. For natural aging (at RT), there was no significant recovery, and the hardness was maintained at a high level.

The BF-STEM and HRTEM images of the CS samples aged at 443 K for various durations are shown in Fig. 4.7. The high density of dislocations was significantly recovered after 20 min of aging, as shown in Fig. 4.7(a), compared with Fig. 4.3(a). Some GPB zones (verified by the SADP) were observed near the dislocation line, as shown in Fig. 4.7(b). After aging for 3 d, the dislocation density was further reduced, and fine S phases were formed (Fig. 4.7(c)). In addition, both types of S phases were found to form preferentially along dislocation lines and loops, as shown in Figs. 4.7(d) and (e), supporting the theory that monoclinic S-II phases mainly form along or near dislocations [17].

It is worth mentioning that the S phases in the CS+3dAA samples were not uniformly precipitated along the three $<001>_{Al}$ directions but predominantly along the

$[001]_{Al}$ direction. Also, the characteristic diffraction spots of the S phases seen in the SADP were along a single direction. This phenomenon could be related to the effect of the introduced dislocations on the nucleation of precipitates.

4.3.4 Aging behavior of cyclically-strengthened samples with 20 min pre-aging

The aging behavior of the CS samples pre-aged for 20 min at 443 K is indicated by the green line in Fig. 4.6(a). The 20minAA+CS sample had high hardness. Significant recovery appeared at the beginning of aging, causing the hardness to drop to a plateau. Hardening then occurred, leading to a hardness peak at 3 d of aging. From the DSC results shown in Fig. 4.6(b), it can be seen that peak III, representing S phase formation, disappeared after aging for 3 d, indicating that the S phases had precipitated and were responsible for hardening. The final over-aging stage, caused by the coarsening of the S phases, was observed after 3 d.

Many dislocation lines and fine loops were observed in the 20minAA+CS samples by BF-STEM, as shown in Fig. 4.8(a). In Fig. 4.8(b), GPB zones (confirmed by SADP) were found near the dislocation line, similar to that observed in Fig. 4.7(b). After aging for 3 d, the recovery of dislocations and the formation of S phases were observed, as shown in Fig. 4.8(c). Interestingly, even though GPB zones were generated during pre-aging before CS, S phases evolved from GPB zones still formed preferentially along dislocation lines and loops, as shown in Figs. 4.8 (e) and (f), respectively. Moreover, similar to the CS+3dAA samples, the S phases in the 20minAA+CS+3dAA samples also precipitated predominantly along the $[001]_{Al}$ direction, not uniformly along the three $<001>_{Al}$ directions. The observation along the $[001]_{Al}$ direction, as shown in Fig. 4.8(d), confirmed the anisotropic precipitation of the S phases. Almost all the S phases were elongated along the observation direction. These results indicate that CS can affect the transformation process from the GPB zones to S phases.

4.4 Discussion

4.4.1 Comparison between CS and 20minAA+CS samples

The aging behaviors of the CS and 20minAA+CS samples at 443 K are shown in Fig. 4.6(a). The engineering stress-strain curves of the CS and 20minAA+CS samples aged at 443 K for various durations are shown in Fig. 4.9. The 20minAA+CS sample had a higher strength (also hardness) than the CS sample. However, both samples

showed similar aging behaviors of recovering first and reaching a hardness peak after 3 d. Their stress-strain curves coincided after aging for 20 min and 3 d at 443 K.

Vacancies can be generated by dragging dislocation jogs and are critical in stabilizing the Cu/Mg cluster, which explains the formation of clusters in CS samples [37,43,44]. These clusters can normally grow into GPB zones and further transform into S phases during subsequent aging, as shown in Fig. 4.7. Combined with the results, the stress-strain curves of the CS and 20minAA+CS samples were similar after aging for 20 min and 3 d. It is known that the contribution of the clusters to the strength and the S phase-forming process is similar whether the clusters are generated during cyclic deformation or aging.

The work-hardening rate and true stress were calculated to elucidate the different strengths of the CS and 20minAA+CS samples, as shown in Fig. 4.9(c). When more dislocations are introduced into the material before the tensile test, the work-hardening effect decreases during the tensile test; thus, the corresponding curve shifts to the down right side along the black dashed line. When more clusters or GPB zones are formed, the true stress increases without changing the work-hardening rate; therefore, the curve just shifts to the right side with higher true stress values [45,46]. As seen in Fig. 4.9(c), the curve of the 20minAA+CS sample could be obtained by shifting the curve of the CS samples directly to the right, that is, their difference lies in the contribution of clusters/GPB zones rather than dislocations. In other words, the work hardening effects caused by cyclic deformation in the CS and 20minAA+CS samples were similar, while the precipitation strengthening effects caused by clusters and GPB zones were different. In the CS samples, not all solute atoms participated in the formation of clusters. However, in the 20minAA+CS samples, all solute atoms had been used to form clusters, and clusters had grown into GPB zones, as confirmed from the diffraction pattern of GPB zones in Fig. 4.8(a). Note that the clusters and GPB zones had similar strengthening effects, which was the reason for the first half of the plateau [6]. The number of solute atoms involved in precipitation was distinct in the CS and 20minAA+CS samples. Therefore, the strength difference between the two samples was due to the 20minAA+CS having greater precipitation strengthening effect than in the CS samples.

These explanations are supported by atom probe tomography data from a recently published study [47]. The cluster volume fraction can be calculated by multiplying the cluster number density by the average cluster volume using the cluster analysis results for an Al-Mg-Si alloy provided in Table 2 in [47]. The cluster volume fractions in the CS and CS+2h aging samples were calculated to be 2.2% and 3.9%, respectively. More clusters were formed during subsequent aging, proving that cyclic deformation was not sufficient to stimulate all solute atoms to form clusters, at least under RT. Cyclic deformation at high temperatures might increase the amount of cluster formation, a research topic worth studying.

In the subsequent aging process, the CS and 20minAA+CS samples exhibited a similar mechanical property evolution. The strength decreased, and the ductility increased at the beginning of aging. Dislocations recovered and new clusters/GPB zones by residual solute atoms formed during the subsequent aging of the CS sample. The diffraction pattern of the GPB zones in Fig. 4.7(a) confirmed that all the solute atoms were involved in precipitation. Only the recovery of dislocations occurred during the subsequent aging of the 20minAA+CS sample. There were no microstructural changes because the clusters/GPB zones were completely formed. Therefore, after aging for 20 min, both samples contained completely formed clusters/GPB zones and unrecovered residual dislocations, leading to similar mechanical properties. With further aging for 3 d, the precipitation process from clusters/GPB zones to S phases occurred in both samples; thus, their mechanical properties remained consistent with increased strength and decreased ductility.

4.4.3 Summary of various strengthening methods

The mechanical properties obtained using the various methods are summarized in Fig. 4.10, and the specific elongation and UTS values are listed in Table 4.2. The strengthening curve obtained by the traditional aging heat treatment alone is shown as a red curve. As the aging progresses, the strength of materials continued to increase until reaching a maximum of 311.6 MPa after 14 d. The elongation decreased significantly when S phases were formed (aged for 7 and 14 d). Further aging (over-aging) led to a decreased strength due to the coarsening of the S phases.

Undoubtedly, cyclic plastic deformation resulted in work-hardening. Cyclic deformation on the AQ sample promoted the partial formation of clusters to obtain

precipitation strengthening. When the sample was first pre-aged for 20 min or longer, the clusters/GPB zones were completely formed [6]. Although subsequent cyclic deformation could accelerate the precipitation process, a few minutes at RT was far from sufficient to make substantial changes in hardness because it took a long time for S phases to form even at 443 K. Therefore, the additional precipitation strengthening effect could be ignored, and only the work hardening effect should be considered during the cyclic deformation of pre-aged samples. The 20minAA+CS sample had both dislocations and completely formed clusters/GPB zones, resulting in excellent mechanical properties. Dislocations and S phases were observed in the PA+CS sample; thus, its strength was slightly higher, and its elongation was much lower than that of the 20minAA+CS sample.

Recovery and precipitation occurred during the aging afterward, whether the CS samples were pre-aged for 20 min or not. The change in the mechanical properties during aging is indicated by the red dotted line in Fig. 4.10. First, the mechanical properties of the CS and 20minAA+CS samples shifted to lower strength but higher elongation due to recovery. However, because some dislocations remained, the points representing the CS+20minAA and 20minAA+CS+20minAA samples were still on the upper left side of the 20minAA samples. With further aging for up to 3 d, clusters/GPB zones have formed into S phases, and the mechanical properties moved to a higher strength but lower ductility side, similar to what happens during traditional aging. Aging after CS had a greater slope of strengthening than that of traditional aging heat treatment, although their strengthening mechanism were both through the S phase formation. The S phases formed during aging after CS were finer than those formed during traditional aging (see Fig. 4.5(b) and Fig. 4.7(c)), which explains why the strength could be increased more in the CS+AA samples while sacrificing a certain amount of ductility.

Enhanced mechanical properties can be obtained by combining cyclic deformation and artificial aging. Several points were connected to draw a green line, as shown in Fig. 4.10. The green line shows a new mechanical property limit with strength that far exceeds the limit of traditional aging (red line). Arbitrary properties on the green line can be achieved by controlling cyclic deformation and artificial aging treatments. If high strength is required, pre-aging can be applied first to acquire clusters/GPB zones or S phases, and then cyclic deformation can be conducted to introduce dislocations; if

a balanced mechanical property is preferred, the 20minAA+CS samples possessing a combination of dislocations and clusters/GPB zones can be chosen, and the ductility can be improved by further short-time aging, causing dislocation annihilation.

4.5 Conclusions

The mechanical properties and microstructure of the samples under various conditions were investigated, and the following conclusions were drawn.

1. The cyclically-strengthened sample had better strength and ductility than the peak-aged sample; the difference was attributed to the dislocation lines, loops, and clusters introduced or formed during cyclic deformation. Cyclic deformation could be completed within 10 min at room temperature, while peak aging at 443 K required 14 d.

2. For pre-aged samples with completely formed clusters/GPB zones or S phases, the subsequent cyclic deformation caused work hardening effects.

3. During the aging of the cyclically-strengthened samples, recovery occurred in the initial stage and took less time to reach a higher hardness peak than that of traditional aging.

4. Combining cyclic deformation and aging significantly enhanced the mechanical properties of the materials. The balance between strength and ductility could be customized by adjusting the processing methods.

4.6 References

[1] M. Mihara, E. Kobayashi, T. Sato, Rapid age-hardening behavior of Al-Mg-Cu (-Ag) alloys and incubation stage in the low-temperature aging, Mater. Trans. 54 (2013) 1898–1904. https://doi.org/10.2320/matertrans.MAW201315.

[2] S.P. Ringer, S.K. Caraher, I.J. Polmear, cluster hardening in an aged Al-Cu-Mg alloy, Scr. Mater. 36 (1997) 517–521. https://doi.org/10.1016/S1359-6462(96)00415-0.

[3] Y. Nagai, M. Murayama, Z. Tang, T. Nonaka, K. Hono, M. Hasegawa, Role of vacancy-solute complex in the initial rapid age hardening in an Al-Cu-Mg alloy,

Acta Mater. 49 (2001) 913–920. https://doi.org/10.1016/S1359-6454(00)00348-7.

[4] L. Reich, S.P. Ringer, K. Hono, Origin of the initial rapid age hardening in an Al-1.7 at.% Mg-1.1 at.% Cu alloy, Philos. Mag. Lett. 79 (1999) 639–648. https://doi.org/10.1080/095008399176689.

[5] R.K.W. Marceau, G. Sha, R. Ferragut, A. Dupasquier, S.P. Ringer, Solute clustering in Al-Cu-Mg alloys during the early stages of elevated temperature ageing, Acta Mater. 58 (2010) 4923–4939. https://doi.org/10.1016/j.actamat.2010.05.020.

[6] X. Chen, D. Kim, M. O, C.D. Marioara, S.J. Andersen, A. Lervik, R. Holmestad, E. Kobayashi, Effect of pre-deformation on age-hardening behaviors in an Al-Mg-Cu alloy, Mater. Sci. Eng. A. 820 (2021) 141557. https://doi.org/10.1016/j.msea.2021.141557.

[7] Y.A. Bagaryatsk, Structural changes on aging Al-Cu-Mg alloys, Dokl. Akad. SSSR. 87 (1952).

[8] S.P. Ringer, K. Hono, I.J. Polmear, T. Sakurai, Precipitation processes during the early stages of ageing in Al-Cu-Mg alloys, Appl. Surf. Sci. 94–95 (1996) 253–260. https://doi.org/10.1016/0169-4332(95)00383-5.

[9] S.P. Ringer, T. Sakurai, I.J. Polmear, Origins of hardening in aged Al-Cu-Mg-(Ag) alloys, Acta Mater. 45 (1997) 3731–3744. https://doi.org/10.1016/S1359-6454(97)00039-6.

[10] A. Charai, T. Walther, C. Alfonso, A.M. Zahra, C.Y. Zahra, Coexistence of clusters, GPB zones, S″-, S′- and S-phases in an Al-0.9% Cu-1.4% Mg alloy, Acta Mater. 48 (2000) 2751–2764. https://doi.org/10.1016/S1359-6454(99)00422-X.

[11] G. Sha, R.K.W. Marceau, X. Gao, B.C. Muddle, S.P. Ringer, Nanostructure of aluminium alloy 2024: Segregation, clustering and precipitation processes, Acta Mater. 59 (2011) 1659–1670. https://doi.org/10.1016/j.actamat.2010.11.033.

[12] M. Mihara, C.D. Marioara, S.J. Andersen, R. Holmestad, E. Kobayashi, T. Sato, Precipitation in an Al-Mg-Cu alloy and the effect of a low amount of Ag, Mater. Sci. Eng. A. 658 (2016) 91–98. https://doi.org/10.1016/j.msea.2016.01.087.

[13] F.J. Niu, J.H. Chen, S.Y. Duan, W.Q. Ming, J.B. Lu, C.L. Wu, Z. Le, The effect of pre-deformation on the precipitation behavior of AlCuMg(Si) alloys with low Cu/Mg ratios, J. Alloys Compd. 823 (2020). https://doi.org/10.1016/j.jallcom.2020.153831.

[14] P. Ratchev, B. Verlinden, P. De Smet, P. Van Houtte, Precipitation hardening of anAl–4.2wt% Mg–0.6wt% Cu alloy, Acta Mater. 46 (1998) 3523–3533. https://doi.org/10.1016/S1359-6454(98)00033-0.

[15] C. Zhu, K. Lv, B. Chen, On the S-phase precipitates in 2024 aluminum alloy: An atomic-scale investigation using high-angle annular dark-field scanning transmission electron microscopy, J. Mater. Res. 35 (2020) 1582–1589. https://doi.org/10.1557/jmr.2020.74.

[16] Z. Chen, S. Li, Reinterpretation of precipitation behavior in an aged AlMgCu alloy, J. Mater. Sci. 49 (2014) 7659–7668. https://doi.org/10.1007/s10853-014-8474-y.

[17] X. Chen, C.D. Marioara, S.J. Andersen, J. Friis, A. Lervik, R. Holmestad, E. Kobayashi, Precipitation processes and structural evolutions of various GPB zones and two types of S phases in a cold-rolled Al-Mg-Cu alloy, Mater. Des. 199 (2021) 109425. https://doi.org/10.1016/j.matdes.2020.109425.

[18] L. Kovarik, S.A. Court, H.L. Fraser, M.J. Mills, GPB zones and composite GPB/GPBII zones in Al–Cu–Mg alloys, Acta Mater. 56 (2008) 4804–4815. https://doi.org/10.1016/j.actamat.2008.05.042.

[19] L. Kovarik, M.J. Mills, Structural relationship between one-dimensional crystals of Guinier–Preston–Bagaryatsky zones in Al–Cu–Mg alloys, Scr. Mater. 64 (2011) 999–1002. https://doi.org/10.1016/j.scriptamat.2011.01.033.

[20] L. Kovarik, M.J. Mills, Ab initio analysis of Guinier-Preston-Bagaryatsky zone nucleation in Al-Cu-Mg alloys, Acta Mater. 60 (2012) 3861–3872. https://doi.org/10.1016/j.actamat.2012.03.044.

[21] S.B. Wang, Z.R. Liu, S.L. Xia, J. Key, J.H. Chen, Tetragonal-prism-like Guinier–Preston–Bagaryatsky zones in an AlCuMg alloy, Mater. Charact. 132 (2017) 139–144. https://doi.org/10.1016/j.matchar.2017.08.014.

[22] X. Chen, C.D. Marioara, S.J. Andersen, J. Friis, A. Lervik, R. Holmestad, E. Kobayashi, Data on atomic structures of precipitates in an Al-Mg-Cu alloy studied by high resolution transmission electron microscopy and first-principles calculations, Data Br. 34 (2021) 106748. https://doi.org/10.1016/j.dib.2021.106748.

[23] A.K. Gupta, P. Gaunt, M.C. Chaturvedi, The crystallography and morphology of the S'-phase precipitate in an Al(CuMg) alloy, Philos. Mag. A Phys. Condens. Matter, Struct. Defects Mech. Prop. 55 (1987) 375–387. https://doi.org/10.1080/01418618708209875.

[24] H. Perlitz, A. Westgren, The crystal structure of Al2CuMg, Ark. Kemi Miner. Geol. 16B (1943) 13.

[25] V. Radmilovic, R. Kilaas, U. Dahmen, G.J. Shiflet, Structure and morphology of S-phase precipitates in aluminum, Acta Mater. 47 (1999) 3987–3997. https://doi.org/10.1016/S1359-6454(99)00259-1.

[26] C.B. Zhang, W. Sun, H.Q. Ye, Investigation of the crystallography and morphology of the s' precipitate in an Al(Cumg) alloy by hrem, Philos. Mag. Lett. 59 (1989) 265–271. https://doi.org/10.1080/09500838908206354.

[27] S.C. Wang, M.J. Starink, Two types of S phase precipitates in Al-Cu-Mg alloys, Acta Mater. 55 (2007) 933–941. https://doi.org/10.1016/j.actamat.2006.09.015.

[28] D. Chu, J.W. Morris, The influence of microstructure on work hardening in aluminum, Acta Mater. 44 (1996) 2599–2610. https://doi.org/10.1016/1359-6454(95)00403-3.

[29] R. Kapoor, J.K. Chakravartty, Deformation behavior of an ultrafine-grained Al–Mg alloy produced by equal-channel angular pressing, Acta Mater. 55 (2007) 5408–5418. https://doi.org/10.1016/j.actamat.2007.05.049.

[30] S. Zhang, W. Hu, R. Berghammer, G. Gottstein, Microstructure evolution and deformation behavior of ultrafine-grained Al–Zn–Mg alloys with fine η′ precipitates, Acta Mater. 58 (2010) 6695–6705. https://doi.org/10.1016/j.actamat.2010.08.034.

[31] E.F. Prados, V.L. Sordi, M. Ferrante, The effect of Al2Cu precipitates on the microstructural evolution, tensile strength, ductility and work-hardening

behaviour of a Al–4wt.% Cu alloy processed by equal-channel angular pressing, Acta Mater. 61 (2013) 115–125. https://doi.org/10.1016/j.actamat.2012.09.038.

[32] R.K. Islamgaliev, N.F. Yunusova, I.N. Sabirov, A.V. Sergueeva, R.Z. Valiev, Deformation behavior of nanostructured aluminum alloy processed by severe plastic deformation, Mater. Sci. Eng. A. 319–321 (2001) 877–881. https://doi.org/10.1016/S0921-5093(01)01052-8.

[33] K. Yoshida, A. Ishii, Y. Tadano, Work-hardening behavior of polycrystalline aluminum alloy under multiaxial stress paths, Int. J. Plast. 53 (2014) 17–39. https://doi.org/10.1016/j.ijplas.2013.07.003.

[34] W.Z. Han, Y. Chen, A. Vinogradov, C.R. Hutchinson, Dynamic precipitation during cyclic deformation of an underaged Al-Cu alloy, Mater. Sci. Eng. A. 528 (2011) 7410–7416. https://doi.org/10.1016/j.msea.2011.06.037.

[35] C.R. Hutchinson, F. de Geuser, A. Deschamps, Dynamic room temperature precipitation during cyclic deformation of an Al-Zn-Mg-Cu alloy, in: ICAA13 Pittsburgh, Springer International Publishing, Cham, 2012: pp. 1101–1106. https://doi.org/10.1007/978-3-319-48761-8_165.

[36] X. Chen, E.A. Mørtsell, J.K. Sunde, M. O, C.D. Marioara, R. Holmestad, E. Kobayashi, Enhanced Mechanical Properties in 6082 Aluminum Alloy Processed by Cyclic Deformation, Metals. 11 (2021) 1735. https://doi.org/10.3390/met11111735.

[37] W. Sun, Y. Zhu, R. Marceau, L. Wang, Q. Zhang, X. Gao, C. Hutchinson, Precipitation strengthening of aluminum alloys by room-temperature cyclic plasticity, Science. 363 (2019) 972–975. https://doi.org/10.1126/science.aav7086.

[38] Q. Zhang, Y. Zhu, X. Gao, Y. Wu, C. Hutchinson, Training high-strength aluminum alloys to withstand fatigue, Nat. Commun. 11 (2020) 5198. https://doi.org/10.1038/s41467-020-19071-7.

[39] S. Wenwen, Y. Zhu, R.K.W. Marceau, L. Jiang, L. Wang, X. Gao, Q. Zhang, C. Hutchinson, A Pronounced Hardening Response in Non-Heat-Treatable Al-Mg Based 5xxx Aluminum Alloys, SSRN Electron. J. (2019) 1–7. https://doi.org/10.2139/ssrn.3532190.

[40] C.R. Hutchinson, P.T. Loo, T.J. Bastow, A.J. Hill, J. da Costa Teixeira, Quantifying the strain-induced dissolution of precipitates in Al alloy microstructures using nuclear magnetic resonance, Acta Mater. 57 (2009) 5645–5653. https://doi.org/10.1016/j.actamat.2009.07.060.

[41] V.A. Esin, L. Briez, M. Sennour, A. Köster, E. Gratiot, J. Crépin, Precipitation-hardness map for Al–Cu–Mg alloy (AA2024-T3), J. Alloys Compd. 854 (2021) 157164. https://doi.org/10.1016/j.jallcom.2020.157164.

[42] S.C. Wang, M.J. Starink, N. Gao, Precipitation hardening in Al–Cu–Mg alloys revisited, Scr. Mater. 54 (2006) 287–291. https://doi.org/10.1016/j.scriptamat.2005.09.010.

[43] J. Huang, K. Xu, Y.M. Fan, J.F. Wang, J.C. Zhang, G.Q. Ren, Dislocation luminescence in GaN single crystals under nanoindentation, Nanoscale Res. Lett. 9 (2014) 649. https://doi.org/10.1186/1556-276X-9-649.

[44] J. Peng, S. Bahl, A. Shyam, J.A. Haynes, D. Shin, Solute-vacancy clustering in aluminum, Acta Mater. 196 (2020) 747–758. https://doi.org/10.1016/j.actamat.2020.06.062.

[45] S. Medrano, C.W. Sinclair, Transient strain age hardening of Al–Mg alloys, Materialia. 12 (2020). https://doi.org/10.1016/j.mtla.2020.100796.

[46] S. Medrano, H. Zhao, B. Gault, F. De Geuser, C.W. Sinclair, A model to unravel the beneficial contributions of trace Cu in wrought Al–Mg alloys, Acta Mater. 208 (2021) 116734. https://doi.org/10.1016/j.actamat.2021.116734.

[47] L. Shi, K. Baker, R. Young, J. Kang, J. Liang, B. Shalchi-Amirkhiz, B. Langelier, Y. Brechet, C. Hutchinson, H. Zurob, The effect of chemical patterning induced by cyclic plasticity on the formation of precipitates during aging of an Al–Mg–Si alloy, Mater. Sci. Eng. A. 815 (2021) 141265. https://doi.org/10.1016/j.msea.2021.141265.

Table 4.1

Chemical composition of the investigated Al alloy in mass and atomic percent.

Element	Mg	Cu	Si	Fe	Al
wt.%	2.97	1.00	0.01	0.01	Bal.
at.%	3.31	0.43	0.01	0.005	Bal.

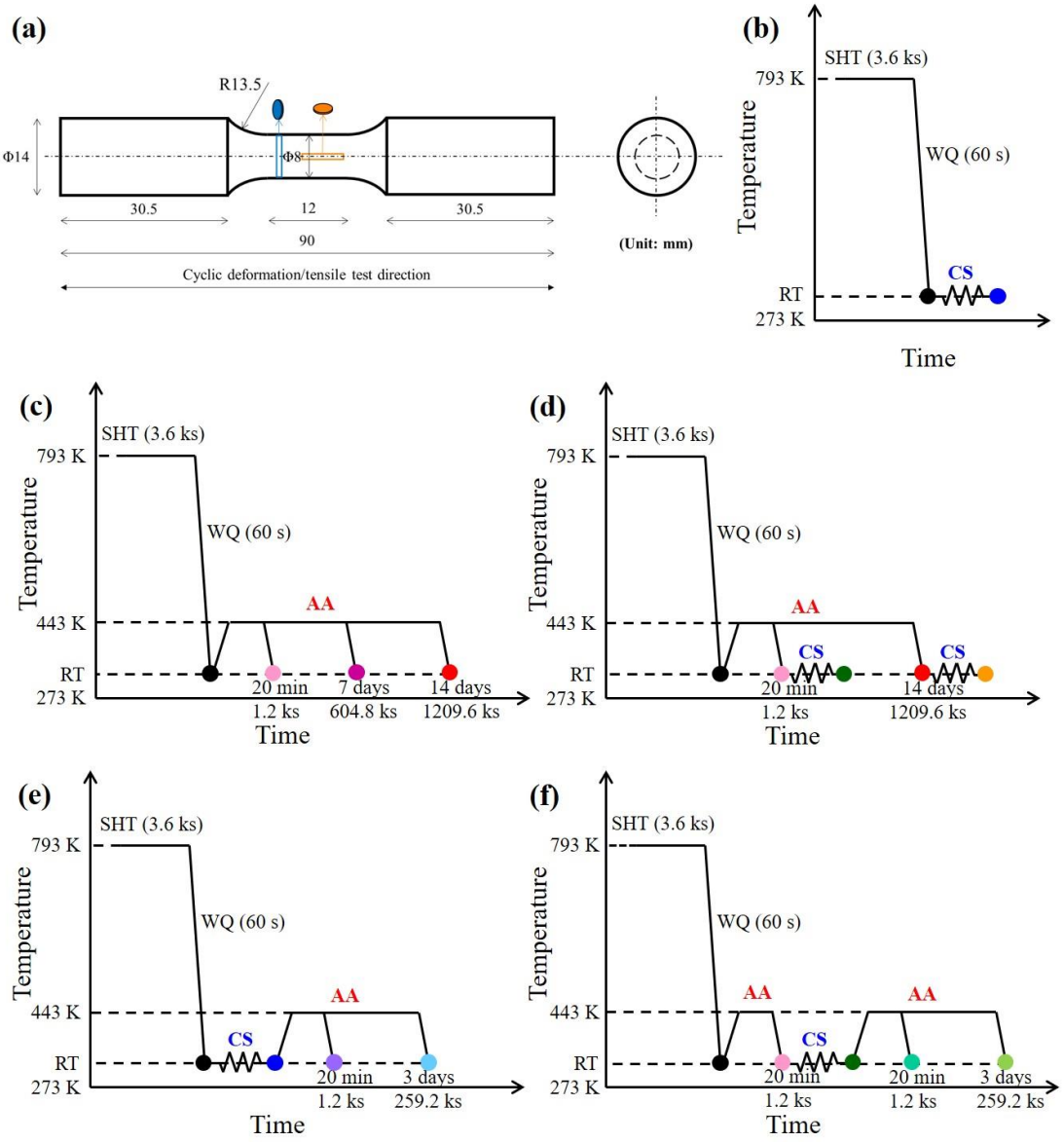

Fig. 4.1 (a) Specimen geometry. (b-f) Schematic of the cyclic deformation and heat treatment process. (b) Cyclically-strengthened (CS) samples, (c) artificially aged (AA) samples, (d) AA then CS (AA+CS) samples, (e) CS then AA (CS+AA) samples, (f) AA, CS, then AA (AA+CS+AA) samples.

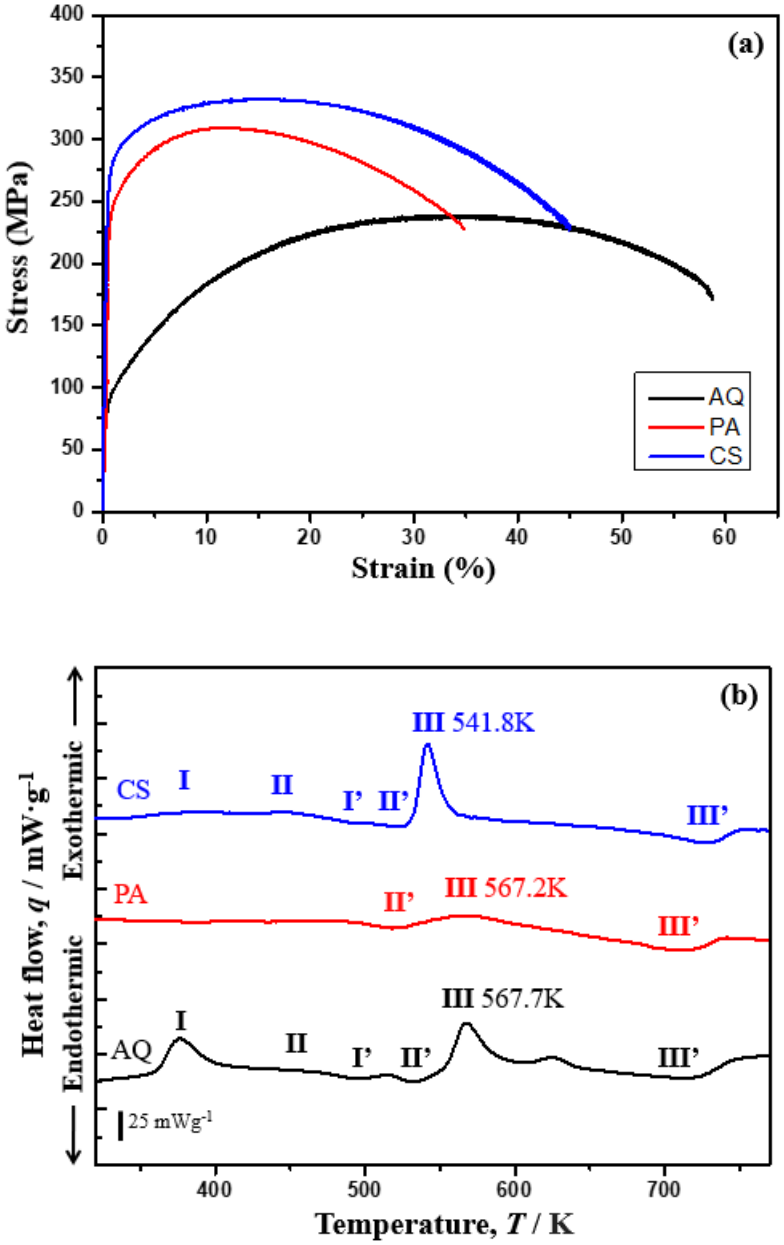

Fig. 4.2 (a) Engineering stress-strain curves and (b) DSC curves of the AQ, PA, and CS samples.

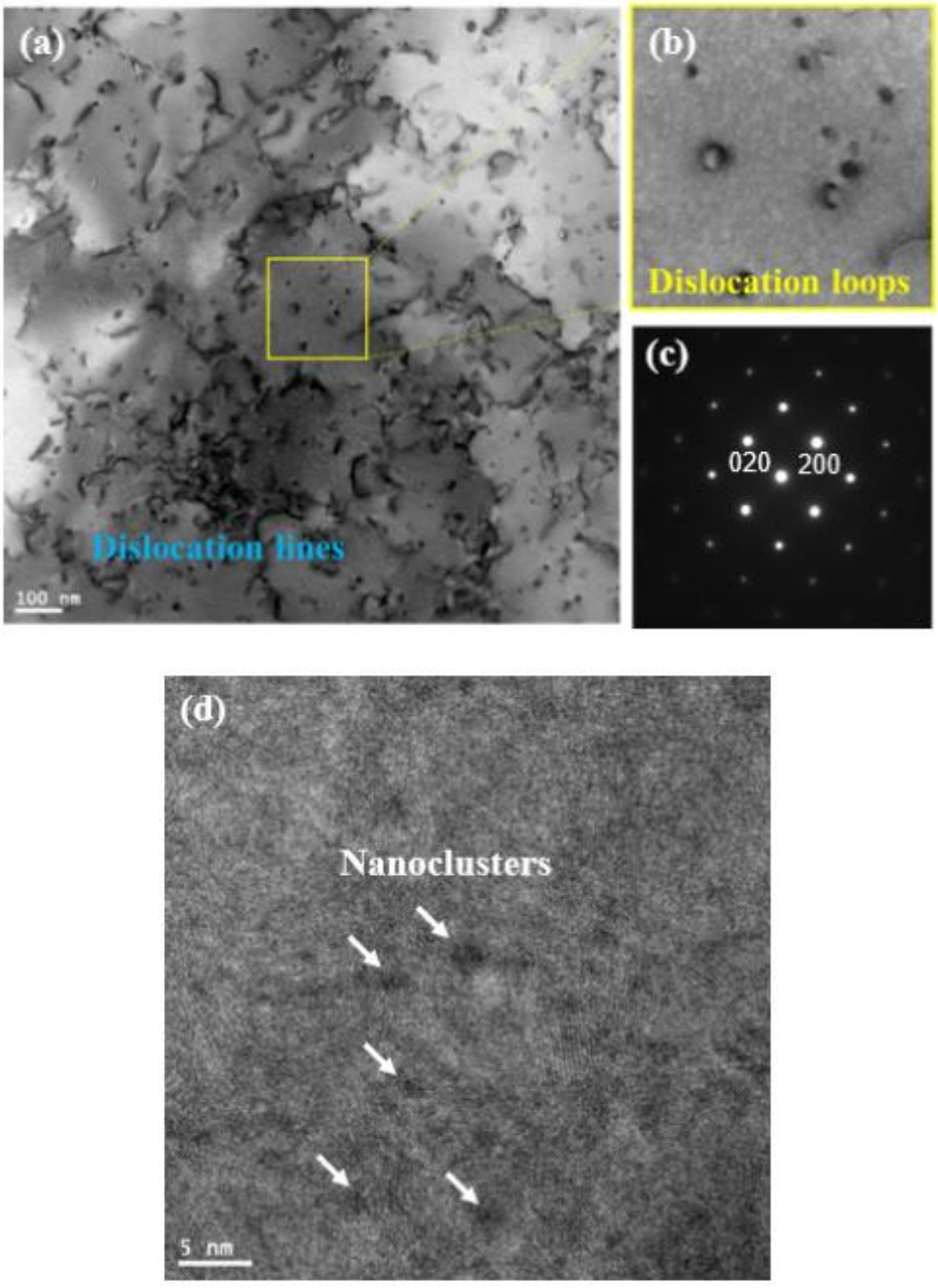

Fig. 4.3 Microstructure observations on the CS sample. (a) BF-STEM image showing dislocation lines and loops. (b) Magnified image of the framed area in (a). (c) The corresponding selected area electron diffraction pattern of (a). (d) HRTEM image showing several nanoclusters.

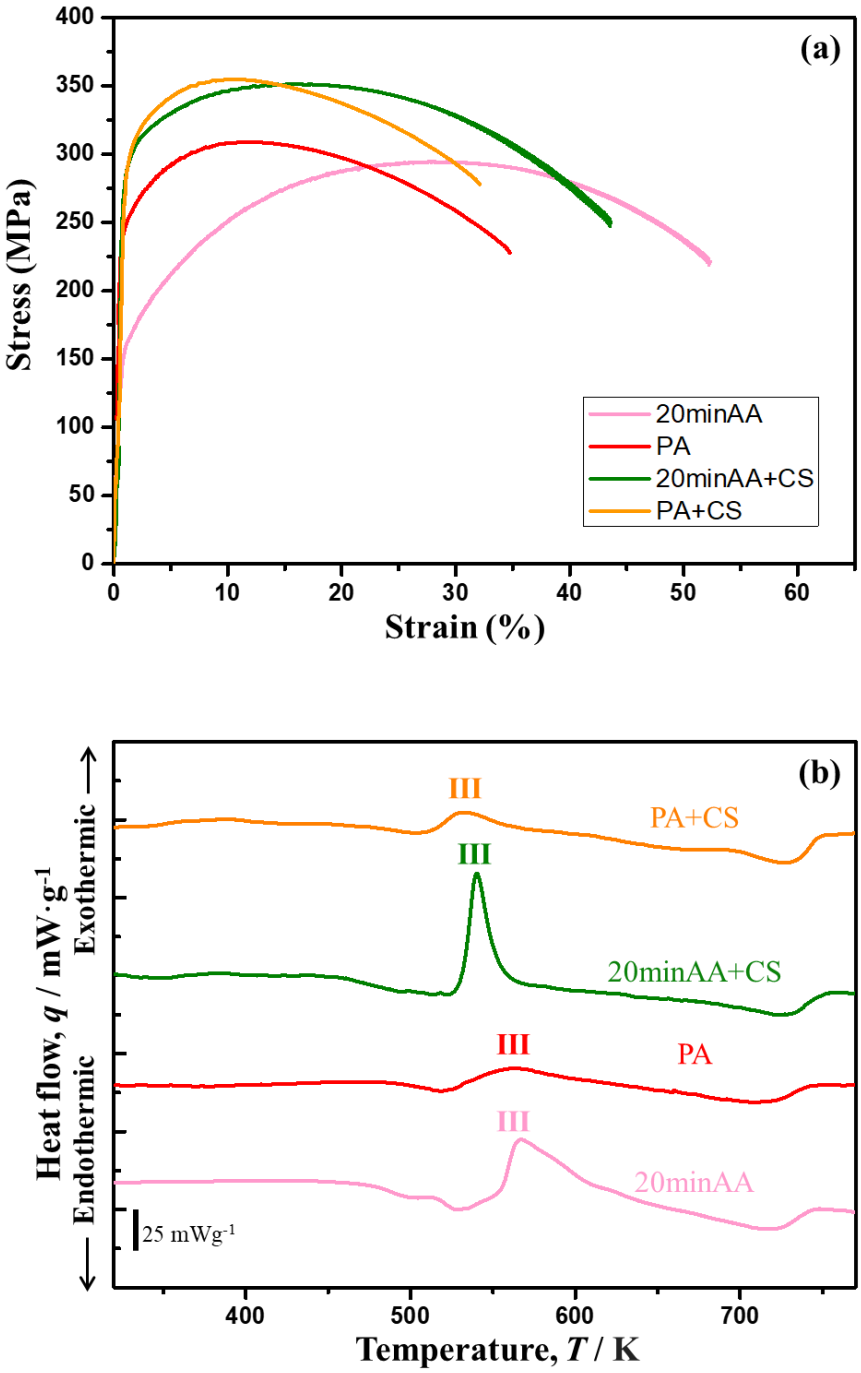

Fig. 4.4 (a) Engineering stress-strain curves and (b) DSC curves for the samples that were artificially aged for 20 min (20minAA), peak-aged (PA), artificially aged for 20 min then cyclically strengthened (20minAA+CS), peak-aged then cyclically strengthened (PA+CS).

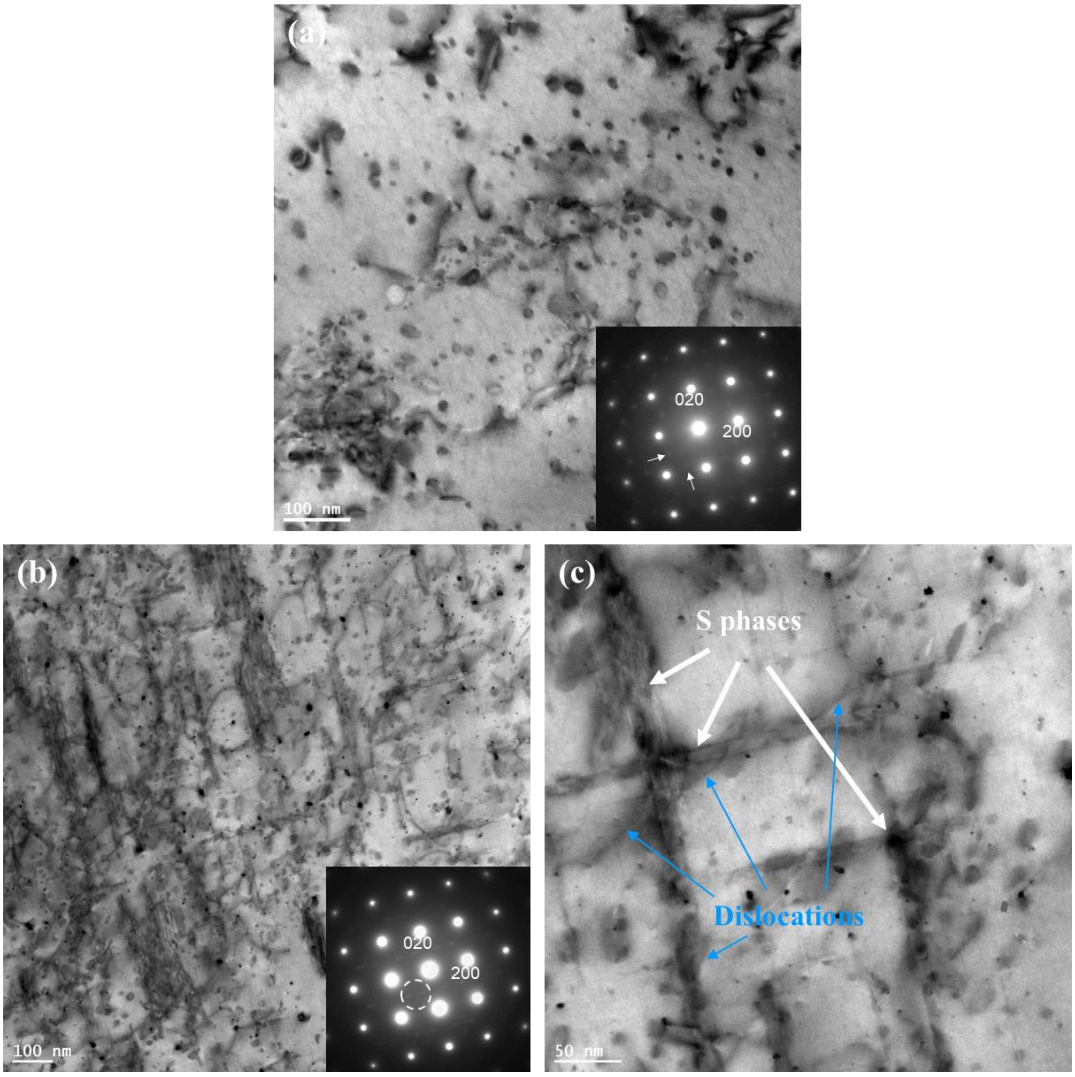

Fig. 4.5 BF-STEM images of (a) 20minAA+CS samples and (b) and (c) PA+CS samples. (a) dislocation lines and loops. (b) S phases and dislocation lines and loops. The inset in (a) shows the diffraction from the GPB zones while that in (b) shows that from the S phases. The many dislocations pinned by S phases are marked by arrows in (c).

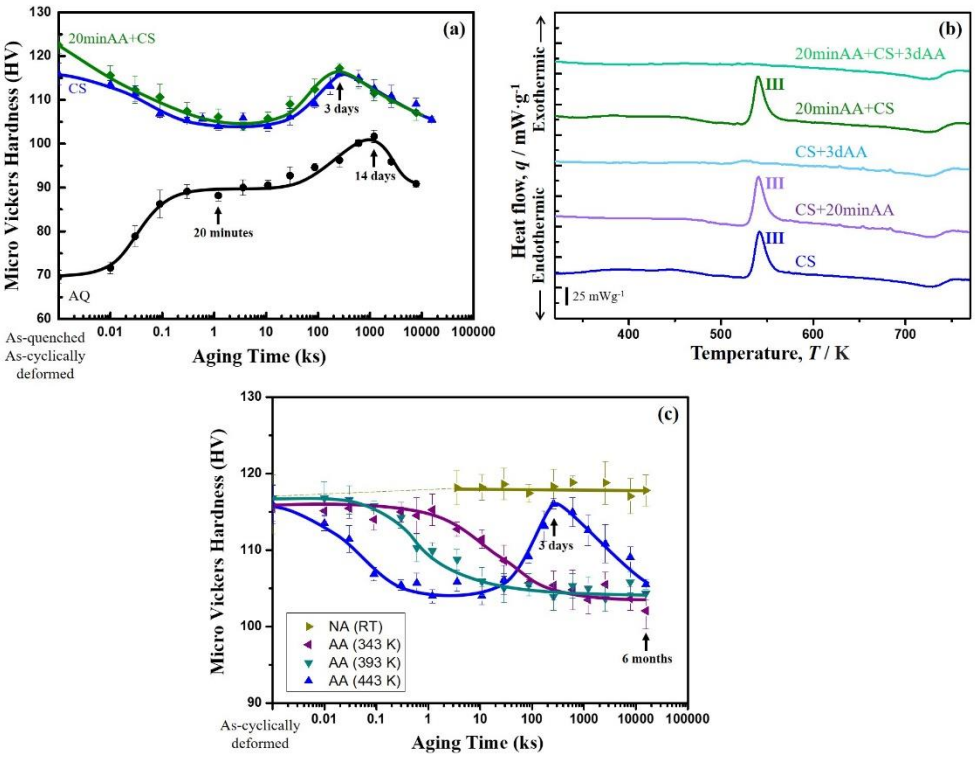

Fig. 4.6 (a) Age-hardening behaviors of the AQ, CS, 20minAA+CS samples at 443 K. (b) DSC curves of the CS and 20minAA+CS samples aged at 443 K for various times. (c) Age-hardening behaviors of the CS samples at different temperatures.

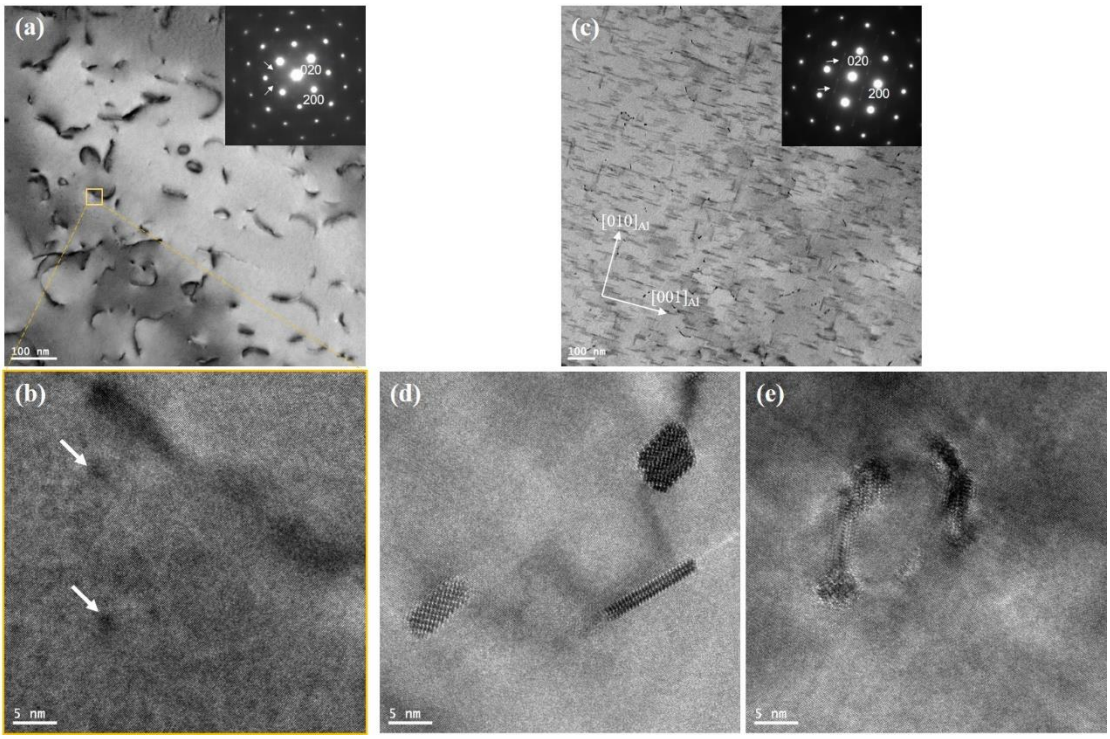

Fig. 4.7 BF-STEM and HRTEM images of CS samples aged at 443 K for (a) and (b) 20 minutes and (c) – (e) 3 d. (a) BF-STEM image showing fewer dislocations after aging. Inset: diffraction from GPB zones. (b) HRTEM image taken from the framed area in (a), showing some GPB zones existing near the dislocation line. (c) BF-STEM image showing fine S phase formed mainly along the [001] $_{Al}$ direction. Inset: diffraction from S phases (almost only one direction). The HRTEM images show two types of S phases formed along the (d) dislocation line and (e) dislocation loop.

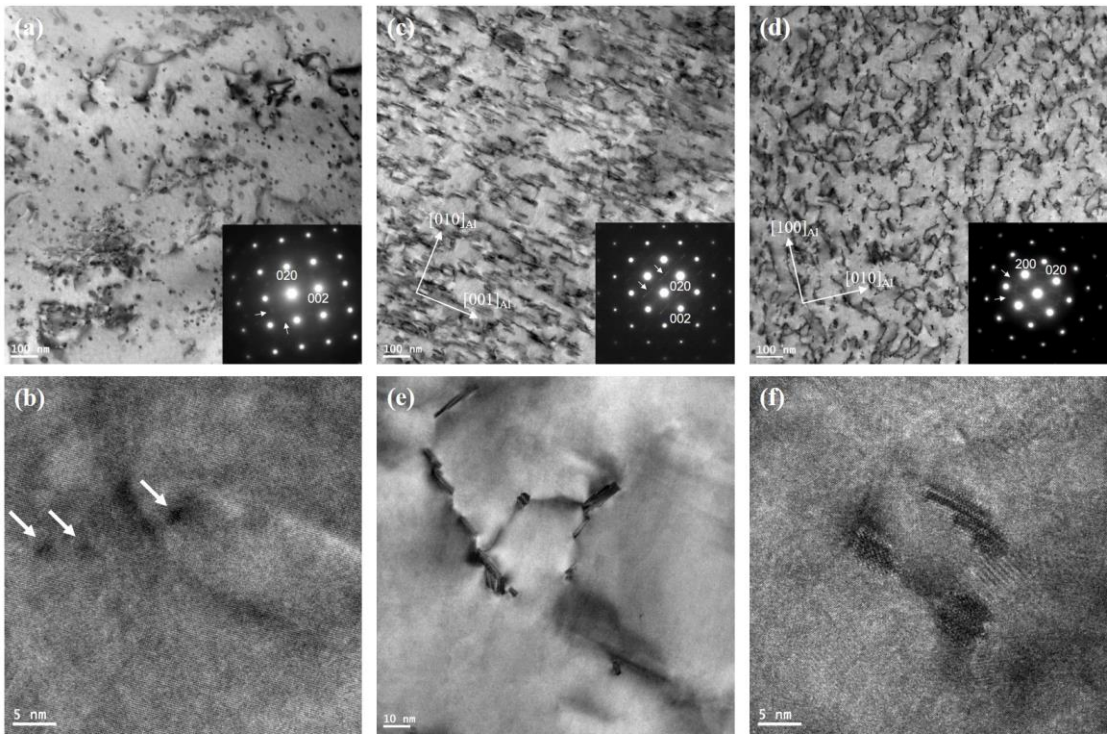

Fig. 4.8 BF-STEM and HRTEM images of (a) and (b) 20minAA+CS samples and (c)-(f) those further aged at 443 K for 3 d. (a) BF-STEM image showing dislocation lines and loops. Inset: diffraction from GPB zones. (b) HRTEM image showing some GPB zones existing near the dislocation line. (c) BF-STEM image showing fine S phases formed mainly along the [001] $_{Al}$ direction. Inset: diffraction from S phases (almost only one direction). (d) BF-STEM image observed along the [001] $_{Al}$ direction. Inset: diffraction from S phases elongated along the observation direction. (e) BF-STEM image showing S phases formed along dislocation lines. (f) HRTEM image showing two types of S phases formed along the dislocation loop.

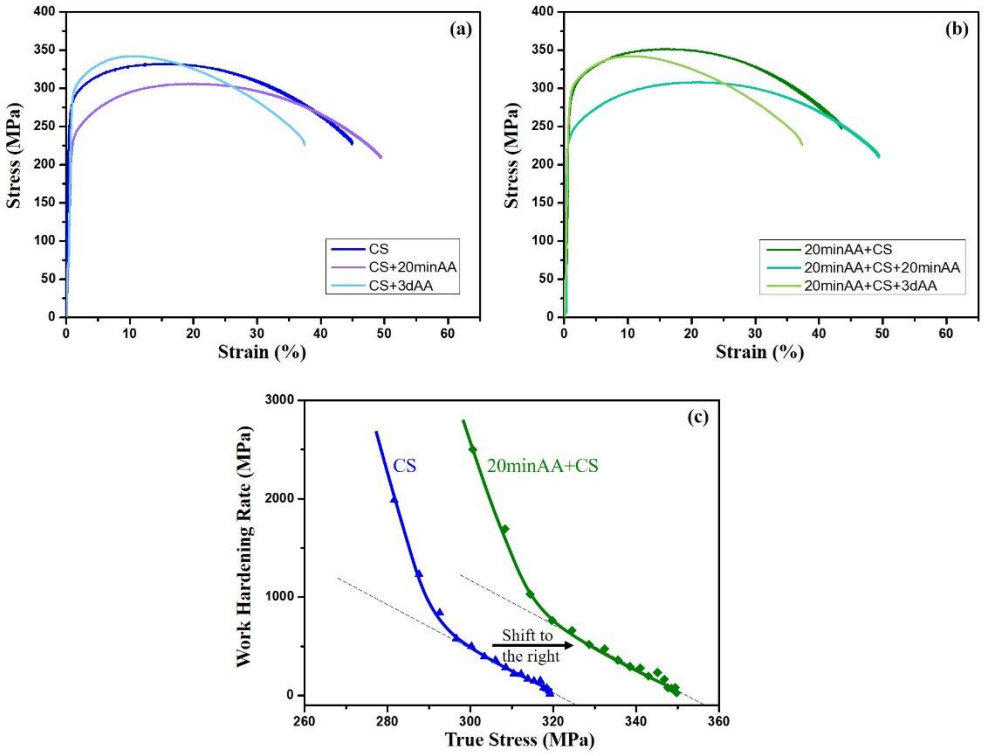

Fig. 4.9 Engineering stress-strain curves of (a) CS and (b) 20minAA+CS samples with different subsequent aging time. (c) Work hardening rate-true stress curves for CS and 20minAA+CS samples.

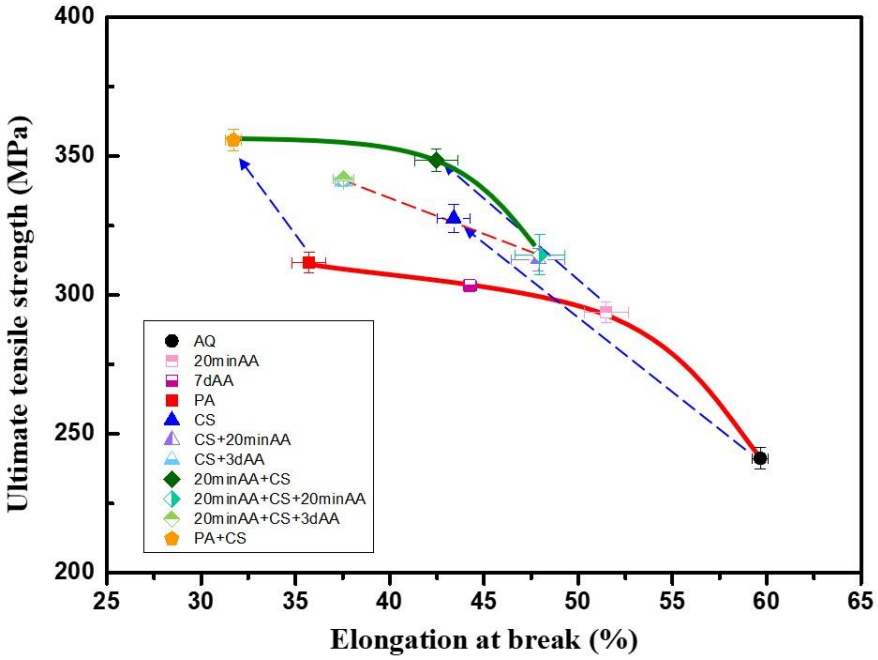

Fig. 4.10 Summary of the mechanical properties of the samples.

Table 4.2. Summary of elongation and UTS values of the samples.

	Elongation (%)		UTS (MPa)	
AQ	59.7	±0.4	241.2	±3.9
20minAA	51.5	±1.2	293.7	±3.8
7dAA	44.3	±0.4	303.4	±2.3
PA	35.7	±0.9	311.6	±3.6
CS	43.4	±0.9	327.6	±5.1
CS+20minAA	47.9	±1.4	312.8	±4.1
CS+3dAA	37.5	±0.4	340.9	±1.7
20minAA+CS	42.5	±1.2	348.5	±4.1
20minAA+CS+20minAA	48.0	±1.3	314.4	±7.2
20minAA+CS+3dAA	37.5	±0.6	341.8	±0.6
PA+CS	31.7	±0.4	355.8	±3.8

Supplementary Material

Age-hardening behavior

The age-hardening behavior of the Al-3Mg-1Cu alloy at 443 K is shown in Fig. S4.1. Four typical stages were observed. A rapid increase was followed by a hardness plateau. Subsequently, the hardness increased again until the peak. Finally, the hardness decreased owing to over-aging. The aging time for the peak-aged condition at 443 K was 14 d.

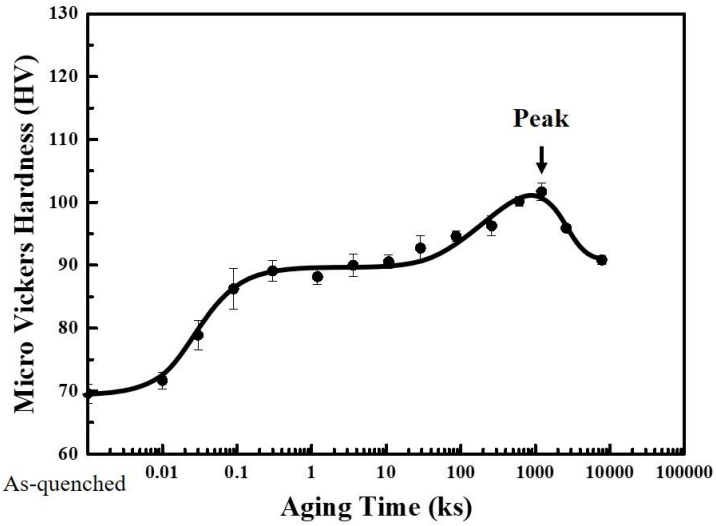

Fig. S4.1 Age-hardening behavior of Al-3Mg-1Cu alloy at 443 K.

Cyclic deformation

Cyclic plastic deformation was conducted at room temperature using a Shimazu Servopulser EHF-EA5, using fully reversed tension-compression cycles, that is, a strain ratio of R = -1 with a sinusoidal waveform. A schematic of this process is shown in Fig. S4.2. The temperature was maintained constant during the entire cyclic deformation. Different cycles, strain amplitudes, and frequencies were tested to study their effects on cyclic strengthening. The results are presented in Fig. S4.3.

As the number of deformation cycles increased, the material was first continuously strengthened, and then the cyclic loading stress tended to stabilize at approximately 500 cycles and remained almost constant until 2000 cycles. Thus, 500 cycles were selected as the standard condition.

A higher strain amplitude produces a greater strengthening effect. The UTS of samples was increased to 299.7 MPa by only applying a strain amplitude of 3.4×10^{-3}. When a strain amplitude of 6.3×10^{-3} was used, the UTS reached 333.2 MPa. However, cracks were generated during CS owing to the excessive strain amplitude, leading to premature fracture during the tensile test. Therefore, a large strain amplitude of 5.5×10^{-3} without microcracks formation was selected as the standard condition. Note that premature fracture may also be related to other factors such as the dislocation number and lattice distortion, which are worth investigating further.

The frequency had no significant influence on the cyclic strengthening effect, which may be due to the significant promotion of the diffusion of solute atoms by CS. In other words, even within a short time, solute atoms can diffuse and aggregate to form clusters, thereby providing a strengthening effect during cyclic deformation. At frequencies of 5 Hz and above, more cycles were required to stabilize the cyclic stress, which may be limited by the cluster formation speed or device stability. A frequency of 1 Hz was selected as the standard condition to ensure the consistency and stability of the experiments.

The advantage of the frequency independence of the cyclic strengthening effect is that the samples can be processed at a high frequency to reduce the time. For example, it only required 140 s to complete the cyclic deformation at 10 Hz. This has tremendous potential for industrial application.

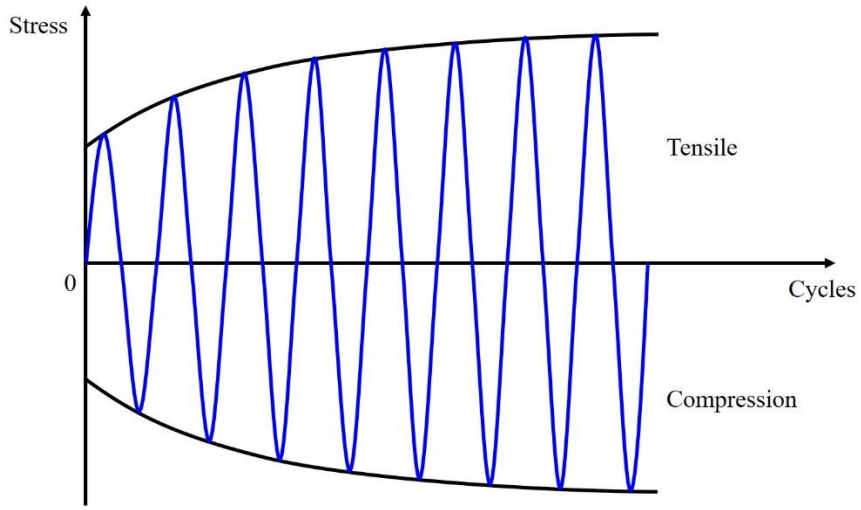

Fig. S4.2 Schematic diagram of the cyclic deformation process. The blue curve shows the load stress change. The black lines show the maximum stress change by connecting the vertices of the cyclic curve. Note that the experimental cyclic strengthening profile in Fig. S4.2(a) also shows maximum stress.

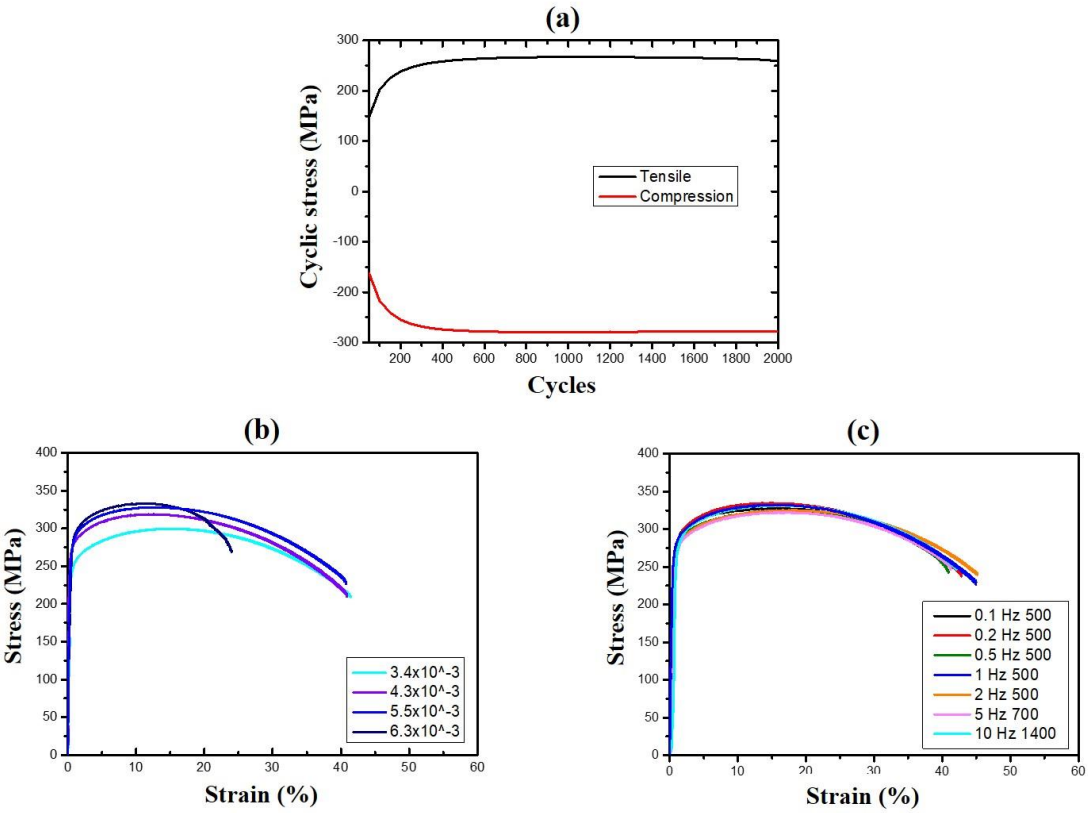

Fig. S4.3 (a) Cyclic strengthening profile, showing the cyclic stress change with cycles. Engineering stress-strain curves for cyclically-strengthened samples with various (b) strain amplitudes and (c) frequencies.

Chapter 5. General Conclusions

"Mechanical properties and microstructure of Al-Mg-Cu alloys processed by plastic deformation and aging heat treatment" has been successfully studied in previous chapters. Conclusions of the present thesis are summarized in this chapter based on both obtained experimental results as well as discussion described in each chapter.

The background and objective of the present thesis are introduced in Chapter 1. The age-hardening behavior and precipitation of Al-Mg-Cu alloys as well as several heat-treatment processes are described.

In Chapter 2, the aging behavior of Al-Mg-Cu alloys with and without pre-deformation in the form of cold rolling are investigated using Vickers hardness measurements, differential scanning calorimetry, transmission electron microscopy, tensile testing, and fracture surface observations. Recovery instead of rapid age hardening is observed at the beginning of aging in highly pre-deformed samples. The S phase formation peaks in the DSC curves of the CR alloys appears at lower temperatures. The GPB zones and S phases cause first and second hardness increases in cold-rolled samples, respectively. The hardness of the plateau is dynamically balanced by the dissolution of clusters/GPB zones and the formation of S phases. The contributions of clusters/GPB zones and S phases to hardness at various aging stages are evaluated. Pre-deformation with paint baking gives a better strength-plasticity combination.

In Chapter 3, precipitation processes and structural evolutions of various GPB zones and two types of S phases are studied in a cold-rolled Al-Mg-Cu alloy by means of Vickers hardness measurements, differential scanning calorimetry, transmission electron microscopy, and density functional theory calculations. A new type of GPB zone named "GPBX" is discovered, which has a higher atomic density than the Al matrix, usually forming along dislocation lines and arranging along the <041>Al direction. The crystal structure of the S-II phase is determined as monoclinic. Common GPB^n zones can only transform to S-I phases, while GPBX zones can grow into S-II phases near/along dislocation lines. The two types of S phases can coexist and nucleate

close to one-another, S-I phases have lath shape morphology, while S-II phases first grow along the dislocation line to become lath-like and further coarsen to rod-shaped precipitates. Cu and Si occupy similar atomic positions in the precipitates, and the complex mixed structures of S and E phases are confirmed.

In Chapter 4, the mechanical properties and microstructure of Al-Mg-Cu alloys processed by cyclic deformation and aging are studied by Vickers hardness measurements, tensile testing, differential scanning calorimetry, and transmission electron microscopy. Cyclic strengthening leads to both better strength and plasticity than the peak-aging because of the introduced or formed dislocation lines, loops, and clusters. Cyclic deformation can be completed at room temperature within 10 minutes while peak aging at 443 K requires 14 days. Recovery occurs first and the hardness peak appears higher and earlier during the aging of cyclically strengthened samples, compared to traditional aged samples. Clusters are partially formed in the cyclically strengthened sample, but can be completely formed after aging for 20 min. The combination of cyclic deformation and aging significantly enhanced the mechanical properties of materials.

In Chapter 5, the overall conclusions obtained from Chapter 2 to Chapter 4 are summarized.

Appendix. A Data on atomic structures of precipitates in an Al-Mg-Cu alloy studied by high-resolution transmission electron microscopy and first-principles calculations

A.1 Data Description

A.1.1 HAADF-STEM images

Fig. A.1 shows the HAADF-STEM images of the as-quenched (A.Q.) and as-rolled (A.R.) samples before aging. There is no precipitate found in the Al matrix (Fig.1 (a) and (d)) or near the defects (the dislocation loop in Fig. A.1(b) and the grain boundary in Fig. A.1(c)). Fig. A.2 shows two types of S phases [1] formed along dislocations in the A.Q. sample aged at 443 K for 8 hours. Fig. A.3 and A.4 are HAADF-STEM images observed in <100>Al orientation in the 7% cold-rolled Al-3Mg-1Cu alloy aged at 443 K for 20 min. Fig. A.3 shows several GPB zones and the GPBX zone as well as the thinnest S-I phase on a dislocation line. The marked area containing the GPBX zone corresponds to Fig. A.2(c) of reference [1]. Several GPBX zones and the thinnest S-I phase as well as a forming S-II phase are found to form along a dislocation line as shown in Fig. A.4. The selected area is magnified and atomic overlaid to be Fig. 7 of reference [1].

A.1.2 First-principles calculations and atomic models

Table A.1 shows the numerical values from DFT calculations of the precipitate structure models presented in Fig. 4 of reference [1], including formation enthalpy per solute atom, pressure and composition. The refined fractional coordinates in the DFT calculated atomic model containing various GPB zones and two types of S phases are listed in Tables A.2-13. In all of the atomic models, the precipitates are embedded in the Al matrix, so the P1 space group is used to give refined coordinates.

Tables A.2 and A.3 represent the models of the GPB^1 zone with Cu or Al interstitial, respectively. Tables A.4 and A.5 show models containing a single GPB^2 zone or a pair of GPB^2 zones, respectively. Table A.6 exhibits the model of the newly observed GPBX

zone. Tables A.7 and A.8 show models of two individual GPBX zones orientated along $<114>_{Al}$ or $<113>_{Al}$ directions, respectively. The illustration can be found in reference [1]. Tables A.9, A.10 and A.11 display the relaxed models of several GPBX zones listed in Tables A.6, A.7 and A.8, respectively. Tables A.12 and A.13 show the models of S-I and S-II phases, respectively.

A.2 Experimental Design, Materials and Methods

A.2.1 Materials

The investigated Al-Mg-Cu alloy (3.04% Mg, 1.01% Cu, 0.01% Si, 0.01% Fe, and Al of the remaining amount, all by mass) was provided by Furukawa sky (now, UACJ Corporation). In the factory, materials were mold cast into 400 x 170 x 40 mm bulk materials and homogenized at 773 K for 10 hours. After the facing work, the billets were rolled into 3 mm thick sheets at 683 K. Finally, the sheets were cold rolled to a thickness of 1.2 mm.

The received materials were cut to small sheet-shaped samples of dimension 10 x 10 x 1.2 (in mm), and then solution heat treated (SHT) in a salt bath at 793 K for 1 hour, followed by quenching in iced water (273 K). After SHT, cold rolling (CR) was performed at room temperature (approximately 293 K) with a reduction rate of 7%. The change in thickness of the sheet was monitored to determine the reduction rate. Isothermal artificial aging was performed on the A.Q. and A.R. samples in an oil bath at 443 K for 20 minutes and 8 hours, respectively. The as-quenched and as-rolled conditions are abbreviated as “A.Q.” and “A.R.” respectively.

A.2.2 Transmission electron microscopy

For the preparation of TEM specimens, 1.2 mm thick sheet samples were first ground down to around 100 μm thickness, and then from 3 mm diameter discs were punched out of ground thin sheets. Subsequently, a Struers TenuPol-5 machine was used to electropolishing the discs until perforation. Two liters of electrolyte was prepared by mixing the 667 ml nitric acid (60.0% concentration) and 1333 ml methanol (99.0% concentration), and the temperature was kept between 243 K and 253 K during electropolishing. To reduce the amount of contamination, prior to the HAADF-STEM observations, all specimens were plasma cleaned for 3 minutes in a Fischione 1020

Plasma Cleaner. All the high-resolution HAADF-STEM images in this article were taken in a $<100>_{Al}$ orientation, as precipitates extending along this direction. The instrument was a double Cs corrected JEOL ARM 200F operated at 200 kV. The convergence semi-angle was set to 28 mrad and the inner collection angle of the HAADF detector was 48 mrad.

Some of the HAADF-STEM images were filtered using a circular bandpass mask applied on the respective fast Fourier transform (FFT) to further improve the clarity, and an inverse FFT (IFFT) was performed on the masked area. This operation can cut all spatial frequencies that correspond to features in the real space smaller than 0.15nm. The operation was performed in the software "GMS 3".

A.2.3 First-principles calculations

The first principles calculations were carried out with density functional theory as implemented in the Vienna ab initio simulation package (VASP) [6,7]. All formation enthalpies were calculated at zero Kelvin using the projector augmented wave method within the PBE (Perdew–Burke–Ernzerhof) generalized gradient approximation [4] with a plane-wave energy cut-off of 400 eV. A Monkhorst-Pack gamma-centered k-point mesh was used, with maximal k-point distances of 0.18 $Å^{-1}$ in each direction [5]. Partial occupancies were smeared using the first-order Methfessel-Paxton method with a smearing factor (SIGMA) of 0.2. For final energies, the tetrahedron method with Blöchl correction for the smearing [8]. The convergence criteria for the electronic convergence in the self-consistent cycles was 10^{-6} eV and the atomic positions were relaxed to a maximal atomic force of 1 meV/Å.

The zero Kelvin formation enthalpies were calculated as described by Marioara et al. [9] using a fixed aluminum lattice parameter of 4.0400 Å, corresponding to the lattice parameter relaxed with VASP using the above parameters. Not relaxing the supercell size makes it easier to compare different calculations but also overestimates the strain contribution to the formation enthalpy (corresponding to the surrounding Al being infinitely hard). A lower limit to the strain contribution was found for the structures with the largest internal pressure as listed in Table A.1 by fully relaxing the supercell size (corresponding to the surrounding Al being infinitely soft). To reduce systematic errors arising from the k-point meshing of different supercell sizes, separate

reference calculations for a single solute atom in the Al lattice were performed for each supercell size.

References

[1] X. Chen, C.D. Marioara, S.J. Andersen, J. Friis, A. Lervik, R. Holmestad, E. Kobayashi, Precipitation processes and structural evolutions of various GPB zones and two types of S phases in a cold-rolled Al-Cu-Mg alloy, Materials and Design. https://doi.org/10.1016/j.matdes.2020.109425.

[2] S.J. Andersen, C.D. Marioara, J. Friis, R. Bjørge, Q. Du, I.G. Ringdalen, S. Wenner, E.A. Mørtsell, R. Holmestad, T. Saito, J. Røyset, O. Reiso, Directionality and column arrangement principles of precipitates in Al-Mg-Si-(Cu) and Al-Mg-Cu linked to line defect in Al, Mater. Sci. Forum. 877 (2017) 461–470. https://doi.org/10.4028/www.scientific.net/MSF.877.461.

[3] K. Momma and F. Izumi, VESTA 3 for three-dimensional visualization of crystal, volumetric and morphology data, J. Appl. Crystallogr., 44 (2011)1272-1276. http://jp-minerals.org/vesta/en/

[4] J.P. Perdew, K. Burke, M. Ernzerhof, Generalized Gradient Approximation Made Simple, Phys. Rev. Lett. 77 (1996) 3865–3868. https://doi.org/10.1103/PhysRevLett.77.3865.

[5] H.J. Monkhorst, J.D. Pack, Special points for Brillouin-zone integrations, Phys. Rev. B. 13 (1976) 5188–5192. https://doi.org/10.1103/PhysRevB.13.5188.

[6] G. Kresse, J. Hafner, Ab initio molecular dynamics for liquid metals, Phys. Rev. B. 47 (1993) 558–561. https://doi.org/10.1103/PhysRevB.47.558.

[7] G. Kresse, J. Furthmüller, Efficiency of ab-initio total energy calculations for metals and semiconductors using a plane-wave basis set, Comput. Mater. Sci. 6 (1996) 15–50. https://doi.org/10.1016/0927-0256(96)00008-0.

[8] P.E. Blöchl, Projector augmented-wave method, Phys. Rev. B. 50 (1994) 17953–17979. https://doi.org/10.1103/PhysRevB.50.17953.

[9] C.D. Marioara, W. Lefebvre, S.J. Andersen, J. Friis, Atomic structure of hardening precipitates in an Al-Mg-Zn-Cu alloy determined by HAADF-STEM and first-

principles calculations: Relation to η-MgZn2, J. Mater. Sci. 48 (2013) 3638–3651. https://doi.org/10.1007/s10853-013-7158-3.

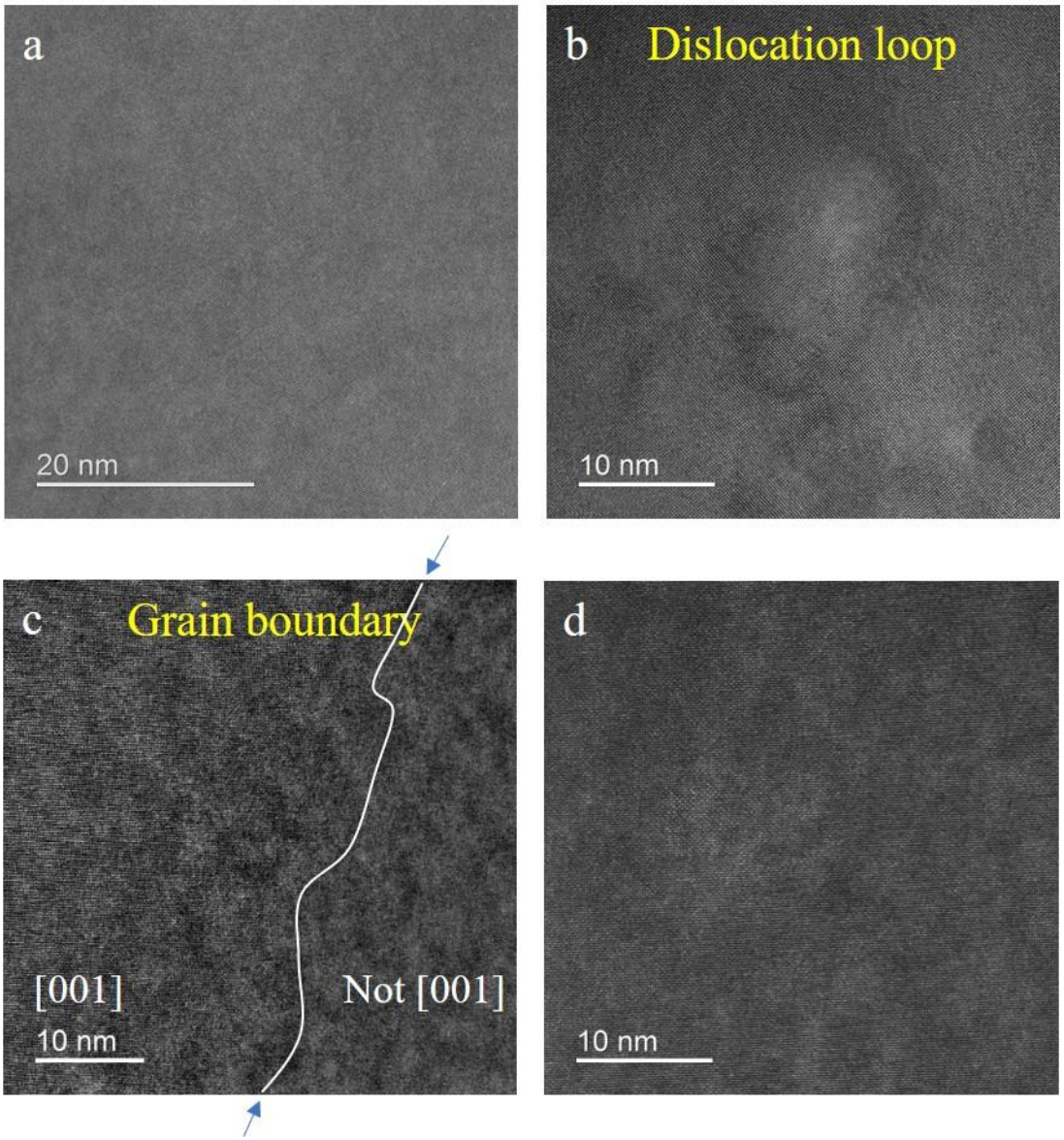

Fig. A.1. HAADF-STEM images of the as-quenched (AQ) and as-rolled (AR) samples, showing no precipitate has been formed. (a) The Al matrix in the AQ sample. (b) Example of quenched in dislocation loop in the AQ sample. (c) (FFT filtered image) Two grains in the AR sample, separated by blue arrowed grain boundary. The left side grain is orientated in a $<001>_{Al}$ direction, while the right side is different since no clear atomic arrangement cannot be found. (d) The Al matrix in the AR sample.

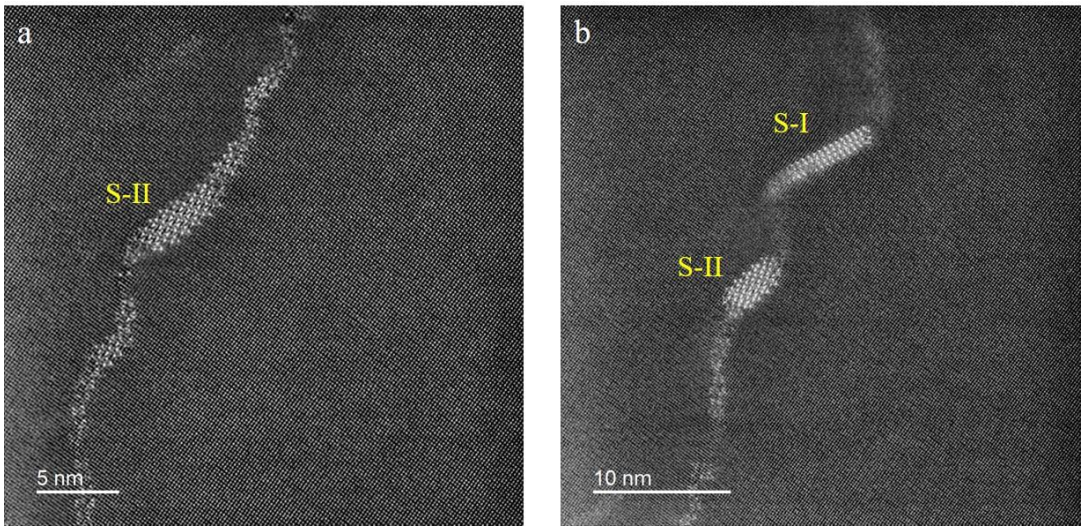

Fig. A.2. FFT filtered HAADF-STEM images in the AQ sample aged at 443 K for 8 hours. (a) The S-II phase, (b) Both the S-I and S-II phase were found on dislocations.

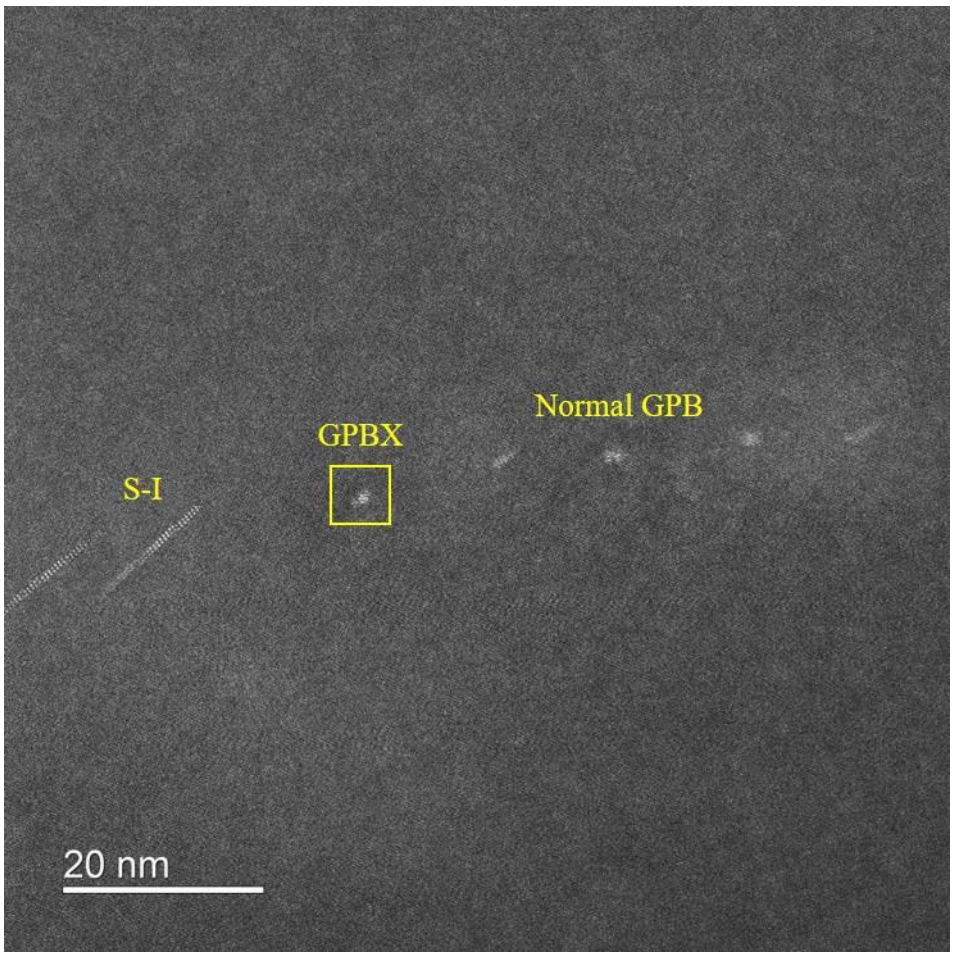

Fig. A.3 HAADF-STEM image in a $<100>_{Al}$ orientation showing normal GPB zones, novel GPBX zone, and S-I phase along dislocation line in the AR samples aged at 443 K for 20 min.

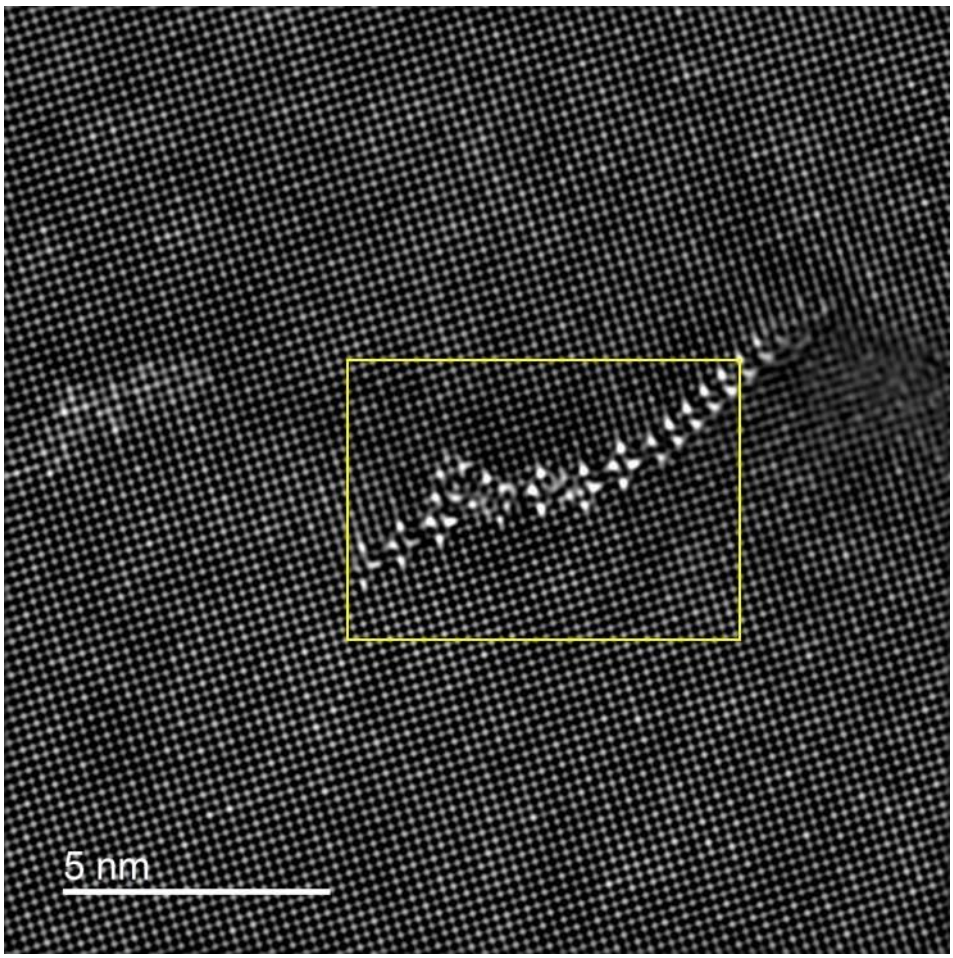

Fig. A.4 FFT filtered HAADF-STEM image in a $<100>_{Al}$ orientation showing precipitates along dislocation line in the AR samples aged at 443 K for 20 min.

Table A.1

Results from DFT calculations of the precipitate structure models.

Refined model	Formation enthalpy per solute atom	Pressure	Composition		
	(eV/solute atom)	(kBar)	Al	Cu	Mg
GPB[1] (Cu interstitial)	-0.1706	-0.630	135	5	4
GPB[1] (Al interstitial)	-0.2425	0.720	136	4	4
GPB[2]	-0.2515	1.260	132	6	6
2GPB[2]	-0.2644	2.130	120	12	12
GPBX	-0.1458	14.210	138	4	4
2GPBX_113	-0.1522	26.780	132	8	8
2GPBX_114	-0.1599	27.740	132	8	8
GPBX_relax	-0.2278	0.000	138	4	4
2GPBX_113_relax	-0.2397	-0.020	132	8	8
2GPBX_114_relax	-0.2522	0.000	132	8	8
S-I	-0.2339	6.210	34	4	4
S-II	-0.2171	-33.060	50	12	12

Table A.2

The refined fractional coordinates in the atomic model for the GPB[1] (Cu interstitial) zone.

GPB[1] (Cu interstitial)				a = 24.24 Å, b = 24.24 Å, c = 4.04 Å				α = 90.0°, β = 90.0°, γ = 90.0°			
Atoms	x	y	z	Atoms	x	y	z	Atoms	x	y	z
Al1	0.04162	0.04167	0.25	Al49	0.37466	0.04167	0.25	Al88	0.70842	0.04167	0.25
Al2	0.0418	0.12513	0.75	Al50	0.37473	0.12495	0.75	Al89	0.70826	0.1253	0.75
Al3	0.12489	0.04167	0.75	Al51	0.45833	0.04167	0.75	Al90	0.79178	0.04167	0.75
Al4	0.12511	0.12515	0.25	Al52	0.45833	0.12457	0.25	Al91	0.79156	0.12515	0.25
Al5	0.04181	0.20844	0.25	Al53	0.37459	0.20815	0.25	Al92	0.70822	0.20887	0.25
Al6	0.04196	0.29174	0.75	Al54	0.37539	0.29246	0.75	Al93	0.70759	0.29241	0.75
Al7	0.1252	0.20853	0.75	Al55	0.45833	0.20775	0.75	Al94	0.79147	0.20853	0.75
Al8	0.12554	0.29178	0.25	Al56	0.45833	0.29007	0.25	Al95	0.79113	0.29178	0.25
Al9	0.04181	0.37472	0.25	Al57	0.37748	0.37682	0.25	Al96	0.70717	0.37584	0.25
Al10	0.04162	0.45806	0.75	Mg1	0.38252	0.46585	0.75	Al97	0.70754	0.45872	0.75
Al11	0.1255	0.37488	0.75	Al58	0.45833	0.37511	0.75	Al98	0.79117	0.37488	0.75
Al12	0.12482	0.45792	0.25	Cu1	0.45833	0.45441	0.25	Al99	0.79185	0.45792	0.25
Al13	0.04124	0.54167	0.25	Cu2	0.37108	0.54167	0.25	Al100	0.70993	0.54167	0.25
Al14	0.04162	0.62527	0.75	Mg2	0.38252	0.61748	0.75	Al101	0.70754	0.62461	0.75
Al15	0.12442	0.54167	0.75	Cu3	0.45833	0.54167	0.75	Al102	0.79225	0.54167	0.75
Al16	0.12482	0.62541	0.25	Cu4	0.45833	0.62892	0.25	Al103	0.79185	0.62541	0.25
Al17	0.04181	0.70861	0.25	Al59	0.37748	0.70651	0.25	Al104	0.70717	0.7075	0.25
Al18	0.04196	0.7916	0.75	Al60	0.37539	0.79087	0.75	Al105	0.70759	0.79093	0.75
Al19	0.1255	0.70845	0.75	Al61	0.45833	0.70822	0.75	Al106	0.79117	0.70845	0.75
Al20	0.12554	0.79155	0.25	Al62	0.45833	0.79327	0.25	Al107	0.79113	0.79155	0.25
Al21	0.04181	0.87489	0.25	Al63	0.37459	0.87518	0.25	Al108	0.70822	0.87446	0.25
Al22	0.0418	0.9582	0.75	Al64	0.37473	0.95838	0.75	Al109	0.70826	0.95804	0.75
Al23	0.1252	0.8748	0.75	Al65	0.45833	0.87558	0.75	Al110	0.79147	0.8748	0.75
Al24	0.12511	0.95819	0.25	Al66	0.45833	0.95876	0.25	Al111	0.79156	0.95819	0.25
Al25	0.20825	0.04167	0.25	Al67	0.54201	0.04167	0.25	Al112	0.87505	0.04167	0.25
Al26	0.2084	0.1253	0.75	Al68	0.54194	0.12495	0.75	Al113	0.87487	0.12513	0.75
Al27	0.2914	0.04167	0.75	Al69	0.62527	0.04167	0.75	Al114	0.95833	0.04167	0.75
Al28	0.29139	0.12514	0.25	Al70	0.62528	0.12514	0.25	Al115	0.95833	0.12495	0.25
Al29	0.20845	0.20887	0.25	Al71	0.54208	0.20815	0.25	Al116	0.87485	0.20844	0.25
Al30	0.20907	0.29241	0.75	Al72	0.54128	0.29246	0.75	Al117	0.8747	0.29174	0.75
Al31	0.29155	0.20883	0.75	Al73	0.62512	0.20883	0.75	Al118	0.95833	0.20822	0.75
Al32	0.2925	0.29283	0.25	Al74	0.62417	0.29283	0.25	Al119	0.95833	0.29158	0.25
Al33	0.20949	0.37584	0.25	Al75	0.53919	0.37682	0.25	Al120	0.87486	0.37472	0.25
Al34	0.20913	0.45872	0.75	Mg3	0.53415	0.46585	0.75	Al121	0.87505	0.45806	0.75
Al35	0.2941	0.37744	0.75	Al76	0.62256	0.37744	0.75	Al122	0.95833	0.37473	0.75
Al36	0.29349	0.46081	0.25	Al77	0.62318	0.46081	0.25	Al123	0.95833	0.45799	0.25
Al37	0.20673	0.54167	0.25	Cu5	0.54559	0.54167	0.25	Al124	0.87543	0.54167	0.25
Al38	0.20913	0.62461	0.75	Mg4	0.53415	0.61748	0.75	Al125	0.87505	0.62527	0.75
Al39	0.29178	0.54167	0.75	Al78	0.62489	0.54167	0.75	Al126	0.95833	0.54167	0.75
Al40	0.29349	0.62252	0.25	Al79	0.62318	0.62252	0.25	Al127	0.95833	0.62534	0.25
Al41	0.20949	0.7075	0.25	Al80	0.53919	0.70651	0.25	Al128	0.87486	0.70861	0.25

Al42	0.20907	0.79093	0.75	Al81	0.54128	0.79087	0.75	Al129	0.8747	0.7916	0.75
Al43	0.2941	0.7059	0.75	Al82	0.62256	0.7059	0.75	Al130	0.95833	0.7086	0.75
Al44	0.2925	0.79051	0.25	Al83	0.62417	0.79051	0.25	Al131	0.95833	0.79175	0.25
Al45	0.20845	0.87446	0.25	Al84	0.54208	0.87518	0.25	Al132	0.87485	0.87489	0.25
Al46	0.2084	0.95804	0.75	Al85	0.54194	0.95838	0.75	Al133	0.87487	0.9582	0.75
Al47	0.29155	0.8745	0.75	Al86	0.62512	0.8745	0.75	Al134	0.95833	0.87511	0.75
Al48	0.29139	0.95819	0.25	Al87	0.62528	0.95819	0.25	Al135	0.95833	0.95838	0.25

Table A.3

The refined fractional coordinates in the atomic model for the GPB[1] (Al interstitial) zone.

GPB[1] (Al interstitial)				a = 24.24 Å, b = 24.24 Å, c = 4.04 Å				α = 90.0°, β = 90.0°, γ = 90.0°			
Atoms	x	y	z	Atoms	x	y	z	Atoms	x	y	z
Al1	0.0416	0.04167	0.25	Al49	0.37464	0.04167	0.25	Al89	0.70858	0.04167	0.25
Al2	0.04169	0.12503	0.75	Al50	0.37464	0.1248	0.75	Al90	0.70848	0.12511	0.75
Al3	0.12476	0.04167	0.75	Al51	0.45833	0.04167	0.75	Al91	0.79191	0.04167	0.75
Al4	0.12492	0.12502	0.25	Al52	0.45833	0.12451	0.25	Al92	0.79175	0.12502	0.25
Al5	0.04168	0.20825	0.25	Al53	0.37451	0.20777	0.25	Al93	0.70849	0.20848	0.25
Al6	0.04178	0.29152	0.75	Al54	0.37512	0.29177	0.75	Al94	0.70819	0.29181	0.75
Al7	0.12494	0.20827	0.75	Al55	0.45833	0.20744	0.75	Al95	0.79173	0.20827	0.75
Al8	0.12515	0.29151	0.25	Al56	0.45833	0.28963	0.25	Al96	0.79152	0.29151	0.25
Al9	0.04158	0.37457	0.25	Al57	0.37696	0.37538	0.25	Al97	0.70803	0.37534	0.25
Al10	0.04147	0.45797	0.75	Mg1	0.37883	0.46216	0.75	Al98	0.70823	0.45845	0.75
Al11	0.12499	0.37472	0.75	Al58	0.45833	0.37465	0.75	Al99	0.79168	0.37472	0.75
Al12	0.12443	0.45784	0.25	Cu1	0.45833	0.45518	0.25	Al100	0.79224	0.45784	0.25
Al13	0.04117	0.54167	0.25	Cu2	0.37185	0.54167	0.25	Al101	0.71037	0.54167	0.25
Al14	0.04147	0.62536	0.75	Mg2	0.37883	0.62117	0.75	Al102	0.70823	0.62488	0.75
Al15	0.12411	0.54167	0.75	Al59	0.45833	0.54167	0.75	Al103	0.79256	0.54167	0.75
Al16	0.12443	0.62549	0.25	Cu3	0.45833	0.62815	0.25	Al104	0.79224	0.62549	0.25
Al17	0.04158	0.70877	0.25	Al60	0.37696	0.70795	0.25	Al105	0.70803	0.708	0.25
Al18	0.04178	0.79181	0.75	Al61	0.37512	0.79156	0.75	Al106	0.70819	0.79152	0.75
Al19	0.12499	0.70862	0.75	Al62	0.45833	0.70869	0.75	Al107	0.79168	0.70862	0.75
Al20	0.12515	0.79182	0.25	Al63	0.45833	0.7937	0.25	Al108	0.79152	0.79182	0.25
Al21	0.04168	0.87508	0.25	Al64	0.37451	0.87557	0.25	Al109	0.70849	0.87485	0.25
Al22	0.04169	0.95831	0.75	Al65	0.37464	0.95853	0.75	Al110	0.70848	0.95822	0.75
Al23	0.12494	0.87506	0.75	Al66	0.45833	0.87589	0.75	Al111	0.79173	0.87506	0.75
Al24	0.12492	0.95832	0.25	Al67	0.45833	0.95883	0.25	Al112	0.79175	0.95832	0.25
Al25	0.20808	0.04167	0.25	Al68	0.54202	0.04167	0.25	Al113	0.87507	0.04167	0.25
Al26	0.20819	0.12511	0.75	Al69	0.54203	0.1248	0.75	Al114	0.87497	0.12503	0.75
Al27	0.29123	0.04167	0.75	Al70	0.62544	0.04167	0.75	Al115	0.95833	0.04167	0.75
Al28	0.29123	0.12492	0.25	Al71	0.62543	0.12492	0.25	Al116	0.95833	0.12493	0.25
Al29	0.20818	0.20848	0.25	Al72	0.54216	0.20777	0.25	Al117	0.87498	0.20825	0.25
Al30	0.20848	0.29181	0.75	Al73	0.54155	0.29177	0.75	Al118	0.87489	0.29152	0.75
Al31	0.29138	0.20832	0.75	Al74	0.62528	0.20832	0.75	Al119	0.95833	0.20809	0.75

Al32	0.292	0.29197	0.25	Al75	0.62466	0.29197	0.25	Al120	0.95833	0.29142	0.25
Al33	0.20864	0.37534	0.25	Al76	0.5397	0.37538	0.25	Al121	0.87508	0.37457	0.25
Al34	0.20844	0.45845	0.75	Mg3	0.53784	0.46216	0.75	Al122	0.8752	0.45797	0.75
Al35	0.29269	0.37602	0.75	Al77	0.62398	0.37602	0.75	Al123	0.95833	0.37456	0.75
Al36	0.29205	0.4603	0.25	Al78	0.62462	0.4603	0.25	Al124	0.95833	0.45798	0.25
Al37	0.2063	0.54167	0.25	Cu4	0.54482	0.54167	0.25	Al125	0.87549	0.54167	0.25
Al38	0.20844	0.62488	0.75	Mg4	0.53784	0.62117	0.75	Al126	0.8752	0.62536	0.75
Al39	0.29131	0.54167	0.75	Al79	0.62535	0.54167	0.75	Al127	0.95833	0.54167	0.75
Al40	0.29205	0.62304	0.25	Al80	0.62462	0.62304	0.25	Al128	0.95833	0.62536	0.25
Al41	0.20864	0.708	0.25	Al81	0.5397	0.70795	0.25	Al129	0.87508	0.70877	0.25
Al42	0.20848	0.79152	0.75	Al82	0.54155	0.79156	0.75	Al130	0.87489	0.79181	0.75
Al43	0.29269	0.70731	0.75	Al83	0.62398	0.70731	0.75	Al131	0.95833	0.70877	0.75
Al44	0.292	0.79136	0.25	Al84	0.62466	0.79136	0.25	Al132	0.95833	0.79191	0.25
Al45	0.20818	0.87485	0.25	Al85	0.54216	0.87557	0.25	Al133	0.87498	0.87508	0.25
Al46	0.20819	0.95822	0.75	Al86	0.54203	0.95853	0.75	Al134	0.87497	0.95831	0.75
Al47	0.29138	0.87501	0.75	Al87	0.62528	0.87501	0.75	Al135	0.95833	0.87524	0.75
Al48	0.29123	0.95842	0.25	Al88	0.62543	0.95842	0.25	Al136	0.95833	0.9584	0.25

Table A.4

The refined fractional coordinates in the atomic model for the GPB^2 zone.

GPB^2				a = 24.24 Å, b = 24.24 Å, c = 4.04 Å α = 90.0°, β = 90.0°, γ = 90.0°							
Atoms	x	y	z	Atoms	x	y	z	Atoms	x	y	z
Al1	0.0418	0.04178	0.25	Al46	0.37488	0.04126	0.25	Al85	0.70859	0.04158	0.25
Al2	0.04189	0.1252	0.75	Al47	0.37479	0.12418	0.75	Al86	0.70857	0.12494	0.75
Al3	0.12493	0.0419	0.75	Al48	0.45837	0.04148	0.75	Al87	0.7918	0.04162	0.75
Al4	0.12521	0.12539	0.25	Al49	0.45841	0.12427	0.25	Al88	0.79173	0.12506	0.25
Al5	0.04217	0.20823	0.25	Al50	0.37478	0.2066	0.25	Al89	0.70822	0.20835	0.25
Al6	0.04206	0.2914	0.75	Al51	0.37506	0.29105	0.75	Al90	0.70786	0.29186	0.75
Al7	0.12555	0.20872	0.75	Al52	0.45788	0.20808	0.75	Al91	0.79158	0.20854	0.75
Al8	0.12586	0.29215	0.25	Al53	0.45662	0.29199	0.25	Al92	0.79167	0.2916	0.25
Al9	0.04152	0.37429	0.25	Cu2	0.37623	0.37381	0.25	Al93	0.70775	0.37536	0.25
Al10	0.04104	0.4582	0.75	Al54	0.37513	0.46118	0.75	Al94	0.70887	0.46003	0.75
Al11	0.12555	0.37496	0.75	Mg3	0.45562	0.37746	0.75	Al95	0.79174	0.37511	0.75
Al12	0.12298	0.45817	0.25	Al55	0.45745	0.46127	0.25	Al96	0.79192	0.45841	0.25
Al13	0.04099	0.5421	0.25	Cu3	0.37708	0.54141	0.25	Al97	0.70884	0.54192	0.25
Al14	0.04149	0.62542	0.75	Al56	0.37564	0.62279	0.75	Al98	0.70722	0.62293	0.75
Al15	0.12475	0.54159	0.75	Al57	0.45922	0.53873	0.75	Al99	0.79368	0.54183	0.75
Al16	0.12492	0.62489	0.25	Mg4	0.46104	0.62254	0.25	Al100	0.79112	0.62504	0.25
Al17	0.04153	0.70872	0.25	Al58	0.37585	0.70922	0.25	Al101	0.70675	0.70694	0.25
Al18	0.04159	0.79179	0.75	Al59	0.37535	0.79225	0.75	Al102	0.70776	0.79104	0.75
Al19	0.125	0.7084	0.75	Al60	0.46004	0.70801	0.75	Al103	0.79081	0.70785	0.75
Al20	0.12508	0.79146	0.25	Al61	0.45879	0.79192	0.25	Al104	0.79111	0.79128	0.25
Al21	0.04153	0.87511	0.25	Al62	0.37489	0.87555	0.25	Al105	0.70845	0.87472	0.25
Al22	0.04144	0.95856	0.75	Al63	0.37486	0.95853	0.75	Al106	0.7087	0.95822	0.75

Al23	0.12493	0.87494	0.75	Al64	0.45825	0.87573	0.75	Al107	0.79146	0.87461	0.75
Al24	0.12486	0.95838	0.25	Al65	0.4583	0.95852	0.25	Al108	0.79174	0.9581	0.25
Al25	0.20797	0.04178	0.25	Al66	0.54181	0.04147	0.25	Al109	0.87523	0.04144	0.25
Al26	0.20822	0.12528	0.75	Al67	0.54178	0.12445	0.75	Al110	0.87513	0.12489	0.75
Al27	0.29137	0.04161	0.75	Al68	0.62523	0.04158	0.75	Al111	0.95854	0.04163	0.75
Al28	0.29131	0.12474	0.25	Al69	0.62517	0.12476	0.25	Al112	0.95854	0.12505	0.25
Al29	0.20891	0.20895	0.25	Al70	0.54132	0.20775	0.25	Al113	0.87507	0.20821	0.25
Al30	0.20992	0.29306	0.75	Al71	0.54081	0.29078	0.75	Al114	0.87514	0.29128	0.75
Al31	0.29179	0.20857	0.75	Al72	0.625	0.20789	0.75	Al115	0.95865	0.20825	0.75
Al32	0.29398	0.29252	0.25	Al73	0.62452	0.29199	0.25	Al116	0.95849	0.29131	0.25
Al33	0.20944	0.37706	0.25	Al74	0.54103	0.37721	0.25	Al117	0.87518	0.37458	0.25
Al34	0.20783	0.45808	0.75	Cu4	0.53958	0.45859	0.75	Al118	0.87567	0.4579	0.75
Mg1	0.29657	0.37948	0.75	Al75	0.62205	0.37551	0.75	Al119	0.95857	0.37447	0.75
Cu1	0.28912	0.45909	0.25	Mg5	0.62293	0.46158	0.25	Al120	0.95812	0.4581	0.25
Al35	0.20779	0.53997	0.25	Al76	0.54153	0.53882	0.25	Al121	0.87563	0.5418	0.25
Al36	0.20892	0.62464	0.75	Cu5	0.54044	0.62619	0.75	Al122	0.87514	0.62571	0.75
Mg2	0.29374	0.53842	0.75	Cu6	0.62754	0.54091	0.75	Al123	0.95855	0.5419	0.75
Al37	0.29462	0.62449	0.25	Mg6	0.6201	0.62052	0.25	Al124	0.9581	0.62553	0.25
Al38	0.2088	0.70814	0.25	Al77	0.54161	0.70895	0.25	Al125	0.87461	0.7086	0.25
Al39	0.20844	0.79165	0.75	Al78	0.54188	0.7934	0.75	Al126	0.8745	0.79177	0.75
Al40	0.29215	0.70801	0.75	Al79	0.62268	0.70748	0.75	Al127	0.95817	0.70869	0.75
Al41	0.29167	0.79211	0.25	Al80	0.62488	0.79143	0.25	Al128	0.95802	0.79175	0.25
Al42	0.2081	0.87506	0.25	Al81	0.54188	0.87583	0.25	Al129	0.87478	0.8748	0.25
Al43	0.20808	0.95842	0.75	Al82	0.54179	0.95874	0.75	Al130	0.87486	0.95822	0.75
Al44	0.29149	0.87524	0.75	Al83	0.62535	0.87526	0.75	Al131	0.95812	0.87495	0.75
Al45	0.29144	0.95842	0.25	Al84	0.62529	0.95839	0.25	Al132	0.95813	0.95837	0.25

Table A.5

The refined fractional coordinates in the atomic model for the 2GPB^2 zone.

2GPB^2				a = 24.24 Å, b = 24.24 Å, c = 4.04 Å				α = 90.0°, β = 90.0°, γ = 90.0°			
Atoms	x	y	z	Atoms	x	y	z	Atoms	x	y	z
Al1	0.04174	0.04169	0.25	Al43	0.37505	0.04235	0.25	Al79	0.70879	0.04101	0.25
Al2	0.04161	0.12507	0.75	Al44	0.37588	0.12527	0.75	Al80	0.70817	0.1248	0.75
Al3	0.12474	0.04154	0.75	Al45	0.45853	0.04187	0.75	Al81	0.79221	0.04151	0.75
Al4	0.12477	0.12506	0.25	Al46	0.45932	0.12593	0.25	Al82	0.79151	0.12493	0.25
Al5	0.04194	0.2085	0.25	Al47	0.37571	0.20911	0.25	Al83	0.70655	0.208	0.25
Al6	0.04202	0.29167	0.75	Al48	0.37375	0.29218	0.75	Mg10	0.70487	0.29373	0.75
Al7	0.12552	0.20878	0.75	Al49	0.45976	0.21042	0.75	Al84	0.79101	0.20886	0.75
Al8	0.12618	0.29271	0.25	Al50	0.45855	0.29495	0.25	Al85	0.79091	0.29418	0.25
Al9	0.04209	0.37467	0.25	Mg4	0.37047	0.3777	0.25	Cu10	0.70846	0.37695	0.25
Al10	0.04021	0.45803	0.75	Cu4	0.37505	0.45981	0.75	Al86	0.7057	0.45973	0.75
Al11	0.12546	0.37695	0.75	Al51	0.45691	0.37776	0.75	Al87	0.78916	0.37524	0.75
Al12	0.12438	0.45858	0.25	Al52	0.45682	0.45755	0.25	Mg11	0.78944	0.46056	0.25
Al13	0.04238	0.54163	0.25	Al53	0.37169	0.54144	0.25	Al88	0.70669	0.54172	0.25

Al14	0.04193	0.62537	0.75	Al54	0.37174	0.62434	0.75	Cu11	0.70879	0.62693	0.75
Al15	0.12551	0.54052	0.75	Mg5	0.45542	0.54388	0.75	Cu12	0.79384	0.54033	0.75
Al16	0.12459	0.62495	0.25	Cu5	0.45968	0.62319	0.25	Mg12	0.78788	0.62049	0.25
Al17	0.04152	0.70881	0.25	Cu6	0.37443	0.71072	0.25	Al89	0.7086	0.70891	0.25
Al18	0.04172	0.79158	0.75	Al55	0.37545	0.79176	0.75	Al90	0.708	0.7933	0.75
Al19	0.12584	0.70823	0.75	Mg6	0.45431	0.70231	0.75	Al91	0.78998	0.70738	0.75
Al20	0.12548	0.79121	0.25	Al56	0.45628	0.79011	0.25	Al92	0.79149	0.79129	0.25
Al21	0.04178	0.8749	0.25	Al57	0.37496	0.87692	0.25	Al93	0.70815	0.87521	0.25
Al22	0.04149	0.95821	0.75	Al58	0.37499	0.95905	0.75	Al94	0.70844	0.95834	0.75
Al23	0.12508	0.8749	0.75	Al59	0.45796	0.87437	0.75	Al95	0.79208	0.87531	0.75
Al24	0.12462	0.95811	0.25	Al60	0.45845	0.95869	0.25	Al96	0.79209	0.95815	0.25
Al25	0.20791	0.04185	0.25	Al61	0.54155	0.04131	0.25	Al97	0.87538	0.04189	0.25
Al26	0.20792	0.12469	0.75	Al62	0.54204	0.12563	0.75	Al98	0.87492	0.1251	0.75
Al27	0.29156	0.04166	0.75	Al63	0.62501	0.04095	0.75	Al99	0.95851	0.04179	0.75
Al28	0.29185	0.12479	0.25	Al64	0.62504	0.12308	0.25	Al100	0.95822	0.1251	0.25
Al29	0.20851	0.20871	0.25	Al65	0.54372	0.20989	0.25	Al101	0.87452	0.20879	0.25
Al30	0.21002	0.29262	0.75	Mg7	0.54569	0.29769	0.75	Al102	0.87416	0.29177	0.75
Al31	0.292	0.2067	0.75	Al66	0.62455	0.20824	0.75	Al103	0.95828	0.20842	0.75
Al32	0.2914	0.29109	0.25	Cu7	0.62557	0.28929	0.25	Al104	0.95848	0.29119	0.25
Mg1	0.21212	0.37951	0.25	Cu8	0.54032	0.37681	0.25	Al105	0.87541	0.37505	0.25
Cu1	0.20616	0.45967	0.75	Mg8	0.54458	0.45612	0.75	Al106	0.87449	0.45948	0.75
Cu2	0.29121	0.37307	0.75	Al67	0.62826	0.37566	0.75	Al107	0.95807	0.37463	0.75
Al33	0.29331	0.45828	0.25	Al68	0.62831	0.45856	0.25	Al108	0.95762	0.45837	0.25
Mg2	0.21056	0.53944	0.25	Al69	0.54318	0.54245	0.25	Al109	0.87562	0.54142	0.25
Al34	0.21084	0.62476	0.75	Al70	0.54309	0.62224	0.75	Al110	0.87454	0.62305	0.75
Al35	0.2943	0.54027	0.75	Cu9	0.62495	0.54019	0.75	Al111	0.95979	0.54197	0.75
Cu3	0.29154	0.62305	0.25	Mg9	0.62953	0.6223	0.25	Al112	0.95791	0.62533	0.25
Al36	0.20909	0.70582	0.25	Al71	0.54145	0.70505	0.25	Al113	0.87382	0.70729	0.25
Al37	0.20899	0.79114	0.75	Al72	0.54024	0.78958	0.75	Al114	0.87448	0.79122	0.75
Mg3	0.29513	0.70627	0.75	Al73	0.62625	0.70782	0.75	Al115	0.95798	0.70833	0.75
Al38	0.29345	0.792	0.25	Al74	0.62429	0.79089	0.25	Al116	0.95806	0.7915	0.25
Al39	0.20849	0.87507	0.25	Al75	0.54068	0.87407	0.25	Al117	0.87523	0.87493	0.25
Al40	0.20779	0.95849	0.75	Al76	0.54147	0.95813	0.75	Al118	0.87526	0.95846	0.75
Al41	0.29183	0.8752	0.75	Al77	0.62412	0.87472	0.75	Al119	0.95839	0.87493	0.75
Al42	0.29121	0.95899	0.25	Al78	0.62495	0.95765	0.25	Al120	0.95826	0.95831	0.25

Table A.6

The refined fractional coordinates in the atomic model for the GPBX zone.

GPBX				a = 24.24 Å, b = 24.24 Å, c = 4.04 Å				α = 90.0°, β = 90.0°, γ = 90.0°			
Atoms	x	y	z	Atoms	x	y	z	Atoms	x	y	z
Al1	0.03892	0.04266	0.25	Al50	0.70722	0.79094	0.75	Al98	0.29334	0.35722	0.75
Al2	0.03955	0.12523	0.75	Al51	0.79005	0.70834	0.75	Cu1	0.29549	0.41554	0.25
Al3	0.122	0.04279	0.75	Al52	0.78993	0.79154	0.25	Al99	0.19896	0.5525	0.25
Al4	0.12252	0.12445	0.25	Al53	0.7084	0.87435	0.25	Al100	0.2	0.63915	0.75
Al5	0.04044	0.20831	0.25	Al54	0.70923	0.9577	0.75	Cu2	0.26187	0.56079	0.75
Al6	0.0422	0.29221	0.75	Al55	0.79063	0.87473	0.75	Mg2	0.29685	0.63344	0.25
Al7	0.12319	0.207	0.75	Al56	0.79135	0.95784	0.25	Al101	0.20428	0.71779	0.25
Al8	0.12391	0.28988	0.25	Al57	0.87448	0.04201	0.25	Al102	0.20355	0.80065	0.75
Al9	0.20598	0.0423	0.25	Al58	0.87531	0.12545	0.75	Al103	0.2851	0.72282	0.75
Al10	0.20638	0.12276	0.75	Al59	0.95663	0.0424	0.75	Al104	0.28864	0.80271	0.25
Al11	0.29078	0.04171	0.75	Al60	0.95742	0.12559	0.25	Al105	0.20466	0.881	0.25
Al12	0.29112	0.12175	0.25	Al61	0.87602	0.20858	0.25	Al106	0.20514	0.96177	0.75
Al13	0.20681	0.20376	0.25	Al62	0.87671	0.29178	0.75	Al107	0.28955	0.88221	0.75
Al14	0.20712	0.28496	0.75	Al63	0.95824	0.20896	0.75	Al108	0.29009	0.96212	0.25
Al15	0.29177	0.20101	0.75	Al64	0.95943	0.29238	0.25	Al109	0.38156	0.36053	0.25
Al16	0.29242	0.28032	0.25	Al65	0.87663	0.37497	0.25	Mg3	0.36982	0.44988	0.75
Al17	0.37587	0.04164	0.25	Al66	0.87616	0.45836	0.75	Al110	0.46236	0.36555	0.75
Al18	0.37655	0.12123	0.75	Al67	0.95945	0.37564	0.75	Al111	0.46668	0.44418	0.25
Al19	0.46069	0.04105	0.75	Al68	0.95881	0.45891	0.25	Cu3	0.40483	0.52252	0.25
Al20	0.46151	0.12158	0.25	Al69	0.87445	0.54193	0.25	Cu4	0.37119	0.6678	0.75
Al21	0.37712	0.20113	0.25	Al70	0.87334	0.62564	0.75	Al112	0.46772	0.53084	0.75
Al22	0.378	0.28063	0.75	Al71	0.95737	0.54241	0.75	Mg4	0.44281	0.62517	0.25
Al23	0.46199	0.20236	0.75	Al72	0.95552	0.62644	0.25	Al113	0.37331	0.72612	0.25
Al24	0.4631	0.28269	0.25	Al73	0.87271	0.70915	0.25	Al114	0.37424	0.80302	0.75
Al25	0.54466	0.04056	0.25	Al74	0.8724	0.79236	0.75	Al115	0.46121	0.7149	0.75
Al26	0.54551	0.12216	0.75	Al75	0.95489	0.71033	0.75	Al116	0.45953	0.7984	0.25
Al27	0.62774	0.04067	0.75	Al76	0.95471	0.79382	0.25	Al117	0.37486	0.88234	0.25
Al28	0.62855	0.12282	0.25	Al77	0.87283	0.87556	0.25	Al118	0.37553	0.9616	0.75
Al29	0.54635	0.20383	0.25	Al78	0.87362	0.95873	0.75	Al119	0.45984	0.8796	0.75
Al30	0.54612	0.28612	0.75	Al79	0.95501	0.87682	0.75	Al120	0.46027	0.96059	0.25
Al31	0.62919	0.20528	0.75	Al80	0.95581	0.95956	0.25	Al121	0.54792	0.36816	0.25
Al32	0.62971	0.28762	0.25	Al81	0.04259	0.3759	0.25	Al122	0.54815	0.45215	0.75
Al33	0.71005	0.0409	0.25	Al82	0.04251	0.45932	0.75	Al123	0.62964	0.37123	0.75
Al34	0.71086	0.12374	0.75	Al83	0.12602	0.37637	0.75	Al124	0.62927	0.45542	0.25
Al35	0.79221	0.04127	0.75	Al84	0.12686	0.46018	0.25	Al125	0.5457	0.53873	0.25
Al36	0.79307	0.12457	0.25	Al85	0.03911	0.54339	0.25	Al126	0.5398	0.62317	0.75
Al37	0.71166	0.2065	0.25	Al86	0.03741	0.62792	0.75	Al127	0.62759	0.53995	0.75
Al38	0.71194	0.28951	0.75	Al87	0.121	0.54461	0.75	Al128	0.62419	0.624	0.25
Al39	0.79382	0.20776	0.75	Al88	0.11854	0.63119	0.25	Al129	0.54064	0.70695	0.25
Al40	0.79425	0.29097	0.25	Al89	0.03705	0.71212	0.25	Al130	0.54274	0.79346	0.75
Al41	0.7118	0.37299	0.25	Al90	0.03695	0.79573	0.75	Al131	0.62407	0.70742	0.75

Al42	0.71117	0.4569	0.75	Al91	0.11874	0.71519	0.75	Al132	0.62445	0.7911	0.25
Al43	0.79397	0.37419	0.75	Al92	0.12052	0.79725	0.25	Al133	0.54345	0.87635	0.25
Al44	0.79336	0.45769	0.25	Al93	0.03746	0.87806	0.25	Al134	0.54413	0.9589	0.75
Al45	0.70934	0.54091	0.25	Al94	0.03812	0.9605	0.75	Al135	0.62621	0.875	0.75
Al46	0.70789	0.62441	0.75	Al95	0.12032	0.87953	0.75	Al136	0.6271	0.95809	0.25
Al47	0.79228	0.54139	0.75	Al96	0.12113	0.96121	0.25	Al137	0.30332	0.51411	0.25
Al48	0.79054	0.62496	0.25	Al97	0.20546	0.36845	0.25	Al138	0.36336	0.5692	0.75
Al49	0.70722	0.70767	0.25	Mg1	0.22384	0.45818	0.75				

Table A.7

The refined fractional coordinates in the atomic model for the 2GPBX_113 zone.

2GPBX_113				a = 24.24 Å, b = 24.24 Å, c = 4.04 Å				α = 90.0°, β = 90.0°, γ = 90.0°			
Atoms	x	y	z	Atoms	x	y	z	Atoms	x	y	z
Al1	0.03899	0.04219	0.25	Al51	0.37142	0.96552	0.75	Al101	0.872	0.70766	0.25
Al2	0.04037	0.12502	0.75	Al52	0.45565	0.88755	0.75	Al102	0.87155	0.79083	0.75
Al3	0.12088	0.04298	0.75	Al53	0.4571	0.96594	0.25	Al103	0.95486	0.70924	0.75
Al4	0.1222	0.12489	0.25	Al54	0.54324	0.04416	0.25	Al104	0.95391	0.79256	0.25
Al5	0.04213	0.20826	0.25	Al55	0.54468	0.12255	0.75	Al105	0.87256	0.87468	0.25
Al6	0.04452	0.29201	0.75	Al56	0.62836	0.0437	0.75	Al106	0.87496	0.95847	0.75
Al7	0.12374	0.20782	0.75	Al57	0.62946	0.12307	0.25	Al107	0.95438	0.8758	0.75
Al8	0.12533	0.29051	0.25	Al58	0.5457	0.20118	0.25	Al108	0.95611	0.95863	0.25
Al9	0.04557	0.37583	0.25	Al59	0.54575	0.27981	0.75	Mg1	0.22584	0.45986	0.75
Al10	0.04511	0.45898	0.75	Al60	0.63057	0.20219	0.75	Al109	0.29422	0.35849	0.75
Al11	0.12828	0.37709	0.75	Al61	0.63145	0.28153	0.25	Cu1	0.29694	0.41698	0.25
Al12	0.12937	0.46062	0.25	Al62	0.54063	0.88685	0.25	Cu2	0.26484	0.56249	0.75
Al13	0.04149	0.54293	0.25	Al63	0.54226	0.96566	0.75	Mg2	0.29688	0.63442	0.25
Al14	0.03863	0.62746	0.75	Al64	0.62581	0.88555	0.75	Al110	0.28275	0.72483	0.75
Al15	0.123	0.54458	0.75	Al65	0.62738	0.96487	0.25	Al111	0.28554	0.80528	0.25
Al16	0.11938	0.63094	0.25	Al66	0.71225	0.04288	0.25	Al112	0.38097	0.35923	0.25
Al17	0.03672	0.71145	0.25	Al67	0.7133	0.12341	0.75	Mg3	0.37232	0.45029	0.75
Al18	0.03601	0.79496	0.75	Al68	0.79486	0.04183	0.75	Al113	0.46168	0.36035	0.75
Al19	0.11819	0.71493	0.75	Al69	0.7962	0.12374	0.25	Al114	0.46515	0.43803	0.25
Al20	0.11908	0.79697	0.25	Al70	0.71481	0.20377	0.25	Cu3	0.40709	0.52075	0.25
Al21	0.03643	0.87729	0.25	Al71	0.71537	0.28446	0.75	Cu4	0.36794	0.66889	0.75
Al22	0.03745	0.95977	0.75	Al72	0.79755	0.20552	0.75	Mg4	0.43492	0.63083	0.25
Al23	0.11854	0.87936	0.75	Al73	0.79854	0.28734	0.25	Al115	0.36847	0.73045	0.25
Al24	0.11953	0.96119	0.25	Al74	0.798	0.36974	0.75	Al116	0.36971	0.80876	0.75
Al25	0.20376	0.04331	0.25	Al75	0.79891	0.45181	0.25	Al117	0.45198	0.72874	0.75
Al26	0.20483	0.12383	0.75	Al76	0.71604	0.61365	0.75	Al118	0.45546	0.80638	0.25
Al27	0.28762	0.04364	0.75	Al77	0.79772	0.53578	0.75	Al119	0.30556	0.51531	0.25
Al28	0.28872	0.123	0.25	Al78	0.79407	0.62209	0.25	Al120	0.36728	0.56866	0.75
Al29	0.20603	0.20488	0.25	Al79	0.78774	0.70607	0.75	Mg5	0.48216	0.53589	0.75
Al30	0.20748	0.2864	0.75	Al80	0.78885	0.78959	0.25	Al121	0.54866	0.43629	0.75
Al31	0.28972	0.20181	0.75	Al81	0.70965	0.88031	0.25	Cu5	0.54922	0.49784	0.25

Al32	0.29131	0.28114	0.25	Al82	0.71107	0.96182	0.75	Cu6	0.50996	0.64599	0.75
Al33	0.20701	0.36981	0.25	Al83	0.79178	0.87619	0.75	Mg6	0.54481	0.71644	0.25
Al34	0.20103	0.55306	0.25	Al84	0.79337	0.9589	0.25	Al122	0.53618	0.80749	0.75
Al35	0.20049	0.6393	0.75	Al85	0.8767	0.04171	0.25	Al123	0.54741	0.35797	0.25
Al36	0.20276	0.71834	0.25	Al86	0.87809	0.12453	0.75	Al124	0.63439	0.44191	0.25
Al37	0.20121	0.80155	0.75	Al87	0.95773	0.04181	0.75	Mg7	0.62022	0.53231	0.75
Al38	0.20173	0.88226	0.25	Al88	0.95935	0.1249	0.25	Al125	0.71437	0.44841	0.75
Al39	0.20227	0.96295	0.75	Al89	0.87963	0.20694	0.25	Al126	0.71661	0.52744	0.25
Al40	0.28566	0.8852	0.75	Al90	0.88065	0.28943	0.75	Cu7	0.65224	0.60424	0.25
Al41	0.28652	0.96454	0.25	Al91	0.96097	0.20809	0.75	Cu8	0.62021	0.74975	0.75
Al42	0.37241	0.04414	0.25	Al92	0.96269	0.2909	0.25	Mg8	0.6913	0.70685	0.25
Al43	0.37387	0.12254	0.75	Al93	0.88106	0.37174	0.25	Al127	0.62293	0.80823	0.25
Al44	0.45778	0.04417	0.75	Al94	0.88039	0.45522	0.75	Al128	0.63157	0.36145	0.75
Al45	0.45933	0.12253	0.25	Al95	0.96318	0.37413	0.75	Al129	0.71014	0.79689	0.75
Al46	0.37486	0.20104	0.25	Al96	0.96227	0.45741	0.25	Al130	0.7159	0.36519	0.25
Al47	0.3765	0.27987	0.75	Al97	0.87847	0.53918	0.25	Al131	0.54978	0.59807	0.25
Al48	0.46001	0.20077	0.75	Al98	0.8756	0.62372	0.75	Al132	0.61151	0.65142	0.75
Al49	0.46149	0.27916	0.25	Al99	0.96014	0.54118	0.75				
Al50	0.37138	0.88692	0.25	Al100	0.95695	0.62546	0.25				

Table A.8

The refined fractional coordinates in the atomic model for the 2GPBX_114 zone.

2GPBX_114				a = 24.24 Å, b = 24.24 Å, c = 4.04 Å				α = 90.0°, β = 90.0°, γ = 90.0°			
Atoms	x	y	z	Atoms	x	y	z	Atoms	x	y	z
Al1	0.03984	0.0424	0.25	Al51	0.62617	0.04438	0.75	Al99	0.20077	0.55277	0.25
Al2	0.0412	0.1247	0.75	Al52	0.62762	0.12331	0.25	Al100	0.19969	0.63907	0.75
Al3	0.12161	0.04256	0.75	Al53	0.54422	0.20228	0.25	Cu2	0.26356	0.56201	0.75
Al4	0.12294	0.12439	0.25	Al54	0.54433	0.28239	0.75	Mg2	0.29586	0.63456	0.25
Al5	0.04287	0.20749	0.25	Al55	0.62842	0.20264	0.75	Al101	0.20234	0.71807	0.25
Al6	0.04513	0.29079	0.75	Al56	0.62942	0.28122	0.25	Al102	0.20121	0.80112	0.75
Al7	0.12455	0.20699	0.75	Al57	0.53865	0.88517	0.25	Al103	0.28231	0.7243	0.75
Al8	0.12593	0.28968	0.25	Al58	0.54058	0.96476	0.75	Al104	0.28548	0.80455	0.25
Al9	0.04609	0.37437	0.25	Al59	0.62326	0.8858	0.75	Al105	0.38177	0.36182	0.25
Al10	0.04593	0.45794	0.75	Al60	0.62504	0.9651	0.25	Mg3	0.3715	0.45147	0.75
Al11	0.12853	0.37633	0.75	Al61	0.7107	0.04409	0.25	Al106	0.46142	0.36457	0.75
Al12	0.12916	0.46016	0.25	Al62	0.71169	0.12396	0.75	Al107	0.46774	0.44518	0.25
Al13	0.04207	0.54242	0.25	Al63	0.79424	0.04356	0.75	Cu3	0.40759	0.52459	0.25
Al14	0.03834	0.62742	0.75	Al64	0.7954	0.12427	0.25	Cu4	0.36736	0.66934	0.75
Al15	0.12309	0.54451	0.75	Al65	0.71298	0.20335	0.25	Al108	0.47018	0.53317	0.75
Al16	0.11918	0.63086	0.25	Al66	0.71383	0.28302	0.75	Mg4	0.43895	0.6287	0.25
Al17	0.03651	0.71148	0.25	Al67	0.79683	0.20486	0.75	Al109	0.36938	0.72872	0.25
Al18	0.03593	0.79503	0.75	Al68	0.79772	0.2857	0.25	Al110	0.37047	0.80645	0.75
Al19	0.11776	0.71494	0.75	Al69	0.70802	0.8853	0.25	Al111	0.45448	0.72181	0.75
Al20	0.11897	0.79705	0.25	Al70	0.70938	0.96476	0.75	Al112	0.45372	0.80482	0.25

Al21	0.03661	0.8775	0.25	Al71	0.79204	0.88112	0.75	Al113	0.3056	0.51549	0.25
Al22	0.03823	0.96011	0.75	Al72	0.79299	0.96231	0.25	Al114	0.365	0.57041	0.75
Al23	0.1188	0.8793	0.75	Al73	0.87689	0.04279	0.25	Al115	0.5454	0.44537	0.75
Al24	0.12016	0.96096	0.25	Al74	0.87822	0.12464	0.75	Mg5	0.56093	0.53848	0.25
Al25	0.20443	0.04291	0.25	Al75	0.95863	0.04249	0.75	Al116	0.6305	0.43845	0.25
Al26	0.2056	0.12361	0.75	Al76	0.95997	0.12481	0.25	Cu5	0.63252	0.49781	0.75
Al27	0.28816	0.04323	0.75	Al77	0.87968	0.20624	0.25	Al117	0.52971	0.63402	0.75
Al28	0.28914	0.12309	0.25	Al78	0.88107	0.28789	0.75	Al118	0.53213	0.72202	0.25
Al29	0.20685	0.20486	0.25	Al79	0.96161	0.20708	0.75	Cu6	0.59228	0.64261	0.25
Al30	0.2078	0.28605	0.75	Al80	0.96325	0.28969	0.25	Mg6	0.62834	0.71572	0.75
Al31	0.29046	0.20242	0.75	Al81	0.88091	0.37016	0.25	Al119	0.53843	0.80264	0.75
Al32	0.2918	0.28189	0.25	Al82	0.88212	0.45227	0.75	Al120	0.54616	0.36238	0.25
Al33	0.20216	0.88152	0.25	Al83	0.96392	0.37216	0.75	Al121	0.61808	0.80539	0.25
Al34	0.20303	0.96235	0.75	Al84	0.96336	0.45572	0.25	Al122	0.62942	0.36073	0.75
Al35	0.28606	0.88418	0.75	Al85	0.8807	0.53635	0.25	Al123	0.71759	0.44289	0.75
Al36	0.28688	0.96385	0.25	Al86	0.87676	0.62269	0.75	Mg7	0.70402	0.53262	0.25
Al37	0.37222	0.0439	0.25	Al87	0.96155	0.53978	0.75	Al124	0.79754	0.44914	0.25
Al38	0.37369	0.12281	0.75	Al88	0.95781	0.62478	0.25	Al125	0.80019	0.52814	0.75
Al39	0.45676	0.04399	0.75	Al89	0.87071	0.70703	0.25	Cu7	0.73631	0.60521	0.75
Al40	0.45838	0.12321	0.25	Al90	0.87131	0.79083	0.75	Cu8	0.70348	0.75015	0.25
Al41	0.3748	0.20211	0.25	Al91	0.95394	0.70923	0.75	Al126	0.7991	0.61445	0.25
Al42	0.37658	0.2814	0.75	Al92	0.95377	0.79282	0.25	Mg8	0.77426	0.70784	0.75
Al43	0.45927	0.20244	0.75	Al93	0.87391	0.87749	0.25	Al127	0.70574	0.80836	0.75
Al44	0.46119	0.28203	0.25	Al94	0.87529	0.96016	0.75	Al128	0.71441	0.36265	0.25
Al45	0.37045	0.88596	0.25	Al95	0.9547	0.87639	0.75	Al129	0.79296	0.79784	0.25
Al46	0.37143	0.96456	0.75	Al96	0.95697	0.9597	0.25	Al130	0.79869	0.36609	0.75
Al47	0.45552	0.88481	0.75	Al97	0.20688	0.36934	0.25	Al131	0.63487	0.59675	0.75
Al48	0.45562	0.96493	0.25	Mg1	0.22556	0.45937	0.75	Al132	0.69426	0.6517	0.25
Al49	0.54146	0.044	0.25	Al98	0.29408	0.35883	0.75				
Al50	0.54309	0.1232	0.75	Cu1	0.29636	0.41704	0.25				

Table A.9

The refined fractional coordinates in the atomic model for the GPBX_relax zone.

GPBX_relax				a = 24.49 Å, b = 24.49 Å, c = 3.97 Å α = 90.0°, β = 90.0°, γ = 90.6°							
Atoms	x	y	z	Atoms	x	y	z	Atoms	x	y	z
Al1	0.0392	0.04248	0.25	Al50	0.70683	0.79076	0.75	Al99	0.19861	0.55269	0.25
Al2	0.03986	0.12542	0.75	Al51	0.78969	0.70826	0.75	Al100	0.20017	0.63872	0.75
Al3	0.12208	0.04269	0.75	Al52	0.78974	0.79131	0.25	Al101	0.20449	0.71767	0.25
Al4	0.12267	0.12472	0.25	Al53	0.70816	0.8741	0.25	Al102	0.20392	0.79995	0.75
Al5	0.04093	0.20885	0.25	Al54	0.70911	0.95768	0.75	Al103	0.28601	0.72292	0.75
Al6	0.04273	0.29278	0.75	Al55	0.79056	0.87451	0.75	Al104	0.28896	0.80245	0.25
Al7	0.12349	0.20768	0.75	Al56	0.79133	0.95786	0.25	Al105	0.20467	0.88036	0.25
Al8	0.12468	0.29085	0.25	Al57	0.87445	0.04207	0.25	Al106	0.20509	0.9614	0.75

Al9	0.2058	0.04204	0.25	Al58	0.87531	0.12547	0.75	Al107	0.28935	0.88217	0.75
Al10	0.20639	0.12272	0.75	Al59	0.95671	0.04237	0.75	Al108	0.29007	0.96205	0.25
Al11	0.29068	0.04156	0.75	Al60	0.95752	0.12566	0.25	Al109	0.38067	0.36041	0.25
Al12	0.29118	0.12137	0.25	Al61	0.87609	0.20882	0.25	Al110	0.46217	0.36566	0.75
Al13	0.20698	0.20387	0.25	Al62	0.87693	0.29201	0.75	Al111	0.4665	0.44461	0.25
Al14	0.20785	0.2854	0.75	Al63	0.9585	0.20923	0.75	Al112	0.46808	0.53066	0.74999
Al15	0.29196	0.20054	0.75	Al64	0.95985	0.29257	0.25	Al113	0.37295	0.726	0.24999
Al16	0.29281	0.27944	0.25	Al65	0.87698	0.37507	0.25	Al114	0.37387	0.8039	0.75
Al17	0.37598	0.04179	0.25	Al66	0.87637	0.45825	0.75	Al115	0.45989	0.71469	0.74999
Al18	0.37658	0.1213	0.75	Al67	0.96006	0.37573	0.75	Al116	0.45883	0.79792	0.25
Al19	0.46084	0.0413	0.75	Al68	0.95926	0.45891	0.25	Al117	0.3747	0.88281	0.25
Al20	0.46156	0.12192	0.25	Al69	0.87436	0.54204	0.25	Al118	0.37549	0.96198	0.75
Al21	0.37732	0.20117	0.25	Al70	0.87292	0.62574	0.75	Al119	0.45968	0.87946	0.75
Al22	0.37773	0.28088	0.75	Al71	0.95715	0.54261	0.75	Al120	0.46027	0.96061	0.25
Al23	0.46201	0.20296	0.75	Al72	0.95522	0.6265	0.25	Al121	0.54729	0.36872	0.25
Al24	0.46275	0.28338	0.25	Al73	0.87239	0.70911	0.25	Al122	0.54809	0.4527	0.75
Al25	0.54456	0.04064	0.25	Al74	0.87226	0.79217	0.75	Al123	0.62916	0.3715	0.75
Al26	0.54524	0.12256	0.75	Al75	0.95484	0.71023	0.75	Al124	0.62949	0.4553	0.25
Al27	0.62744	0.04085	0.75	Al76	0.95476	0.79335	0.25	Al125	0.54662	0.53828	0.25
Al28	0.62813	0.12319	0.25	Al77	0.87286	0.87529	0.25	Al126	0.53928	0.62272	0.74999
Al29	0.54597	0.2045	0.25	Al78	0.87362	0.95871	0.75	Al127	0.62796	0.53974	0.75
Al30	0.54591	0.2869	0.75	Al79	0.95525	0.87625	0.75	Al128	0.62353	0.62375	0.25
Al31	0.62888	0.20586	0.75	Al80	0.95592	0.95927	0.25	Al129	0.53988	0.70632	0.24999
Al32	0.62924	0.28821	0.25	Al81	0.04338	0.37632	0.25	Al130	0.542	0.79248	0.75
Al33	0.70994	0.04097	0.25	Al82	0.04313	0.45959	0.75	Al131	0.62332	0.70703	0.75
Al34	0.71072	0.12406	0.75	Al83	0.12681	0.37702	0.75	Al132	0.62396	0.79058	0.25
Al35	0.7922	0.04125	0.75	Al84	0.12739	0.46063	0.25	Al133	0.54317	0.87564	0.25
Al36	0.79303	0.12461	0.25	Al85	0.03871	0.54359	0.25	Al134	0.54397	0.95862	0.75
Al37	0.71141	0.20708	0.25	Al86	0.03718	0.62803	0.75	Al135	0.62573	0.8745	0.75
Al38	0.71191	0.28999	0.75	Al87	0.12005	0.54505	0.75	Al136	0.62679	0.9579	0.25
Al39	0.79378	0.20804	0.75	Al88	0.11858	0.63062	0.25	Al137	0.30316	0.51449	0.25
Al40	0.7944	0.29115	0.25	Al89	0.0375	0.71183	0.25	Al138	0.36353	0.56883	0.74999
Al41	0.71182	0.37311	0.25	Al90	0.03742	0.79512	0.75	Cu1	0.29622	0.41697	0.25
Al42	0.71145	0.45683	0.75	Al91	0.11938	0.71461	0.75	Cu2	0.26191	0.5618	0.75
Al43	0.79428	0.37421	0.75	Al92	0.12076	0.79643	0.25	Cu3	0.40479	0.52154	0.24999
Al44	0.79374	0.45758	0.25	Al93	0.03778	0.87747	0.25	Cu4	0.37048	0.66636	0.74999
Al45	0.70951	0.54071	0.25	Al94	0.0385	0.96015	0.75	Mg1	0.2248	0.4589	0.75
Al46	0.70741	0.62441	0.75	Al95	0.12068	0.87882	0.75	Mg2	0.29645	0.63329	0.25
Al47	0.79231	0.54128	0.75	Al96	0.1214	0.96077	0.25	Mg3	0.37024	0.45002	0.75
Al48	0.79029	0.62507	0.25	Al97	0.2068	0.36866	0.25	Mg4	0.44186	0.62447	0.24995
Al49	0.70661	0.70759	0.25	Al98	0.29373	0.35734	0.75				

Table A.10

The refined fractional coordinates in the atomic model for the 2GPBX_113_relax zone.

2GPBX_113_relax	a = 24.47 Å, b = 25.14 Å, c = 3.98 Å	α = 90.0°, β = 90.0°, γ = 91.1°								
Atoms	x	y	z	Atoms	x	y	z	Atoms	x	y	z
Al1	0.03984	0.0424	0.25	Al51	0.62617	0.04438	0.75	Al99	0.20077	0.55277	0.25
Al2	0.0412	0.1247	0.75	Al52	0.62762	0.12331	0.25	Al100	0.19969	0.63907	0.75
Al3	0.12161	0.04256	0.75	Al53	0.54422	0.20228	0.25	Cu2	0.26356	0.56201	0.75
Al4	0.12294	0.12439	0.25	Al54	0.54433	0.28239	0.75	Mg2	0.29586	0.63456	0.25
Al5	0.04287	0.20749	0.25	Al55	0.62842	0.20264	0.75	Al101	0.20234	0.71807	0.25
Al6	0.04513	0.29079	0.75	Al56	0.62942	0.28122	0.25	Al102	0.20121	0.80112	0.75
Al7	0.12455	0.20699	0.75	Al57	0.53865	0.88517	0.25	Al103	0.28231	0.7243	0.75
Al8	0.12593	0.28968	0.25	Al58	0.54058	0.96476	0.75	Al104	0.28548	0.80455	0.25
Al9	0.04609	0.37437	0.25	Al59	0.62326	0.8858	0.75	Al105	0.38177	0.36182	0.25
Al10	0.04593	0.45794	0.75	Al60	0.62504	0.9651	0.25	Mg3	0.3715	0.45147	0.75
Al11	0.12853	0.37633	0.75	Al61	0.7107	0.04409	0.25	Al106	0.46142	0.36457	0.75
Al12	0.12916	0.46016	0.25	Al62	0.71169	0.12396	0.75	Al107	0.46774	0.44518	0.25
Al13	0.04207	0.54242	0.25	Al63	0.79424	0.04356	0.75	Cu3	0.40759	0.52459	0.25
Al14	0.03834	0.62742	0.75	Al64	0.7954	0.12427	0.25	Cu4	0.36736	0.66934	0.75
Al15	0.12309	0.54451	0.75	Al65	0.71298	0.20335	0.25	Al108	0.47018	0.53317	0.75
Al16	0.11918	0.63086	0.25	Al66	0.71383	0.28302	0.75	Mg4	0.43895	0.6287	0.25
Al17	0.03651	0.71148	0.25	Al67	0.79683	0.20486	0.75	Al109	0.36938	0.72872	0.25
Al18	0.03593	0.79503	0.75	Al68	0.79772	0.2857	0.25	Al110	0.37047	0.80645	0.75
Al19	0.11776	0.71494	0.75	Al69	0.70802	0.8853	0.25	Al111	0.45448	0.72181	0.75
Al20	0.11897	0.79705	0.25	Al70	0.70938	0.96476	0.75	Al112	0.45372	0.80482	0.25
Al21	0.03661	0.8775	0.25	Al71	0.79204	0.88112	0.75	Al113	0.3056	0.51549	0.25
Al22	0.03823	0.96011	0.75	Al72	0.79299	0.96231	0.25	Al114	0.365	0.57041	0.75
Al23	0.1188	0.8793	0.75	Al73	0.87689	0.04279	0.25	Al115	0.5454	0.44537	0.75
Al24	0.12016	0.96096	0.25	Al74	0.87822	0.12464	0.75	Mg5	0.56093	0.53848	0.25
Al25	0.20443	0.04291	0.25	Al75	0.95863	0.04249	0.75	Al116	0.6305	0.43845	0.25
Al26	0.2056	0.12361	0.75	Al76	0.95997	0.12481	0.25	Cu5	0.63252	0.49781	0.75
Al27	0.28816	0.04323	0.75	Al77	0.87968	0.20624	0.25	Al117	0.52971	0.63402	0.75
Al28	0.28914	0.12309	0.25	Al78	0.88107	0.28789	0.75	Al118	0.53213	0.72202	0.25
Al29	0.20685	0.20486	0.25	Al79	0.96161	0.20708	0.75	Cu6	0.59228	0.64261	0.25
Al30	0.2078	0.28605	0.75	Al80	0.96325	0.28969	0.25	Mg6	0.62834	0.71572	0.75
Al31	0.29046	0.20242	0.75	Al81	0.88091	0.37016	0.25	Al119	0.53843	0.80264	0.75
Al32	0.2918	0.28189	0.25	Al82	0.88212	0.45227	0.75	Al120	0.54616	0.36238	0.25
Al33	0.20216	0.88152	0.25	Al83	0.96392	0.37216	0.75	Al121	0.61808	0.80539	0.25
Al34	0.20303	0.96235	0.75	Al84	0.96336	0.45572	0.25	Al122	0.62942	0.36073	0.75
Al35	0.28606	0.88418	0.75	Al85	0.8807	0.53635	0.25	Al123	0.71759	0.44289	0.75
Al36	0.28688	0.96385	0.25	Al86	0.87676	0.62269	0.75	Mg7	0.70402	0.53262	0.25
Al37	0.37222	0.0439	0.25	Al87	0.96155	0.53978	0.75	Al124	0.79754	0.44914	0.25
Al38	0.37369	0.12281	0.75	Al88	0.95781	0.62478	0.25	Al125	0.80019	0.52814	0.75
Al39	0.45676	0.04399	0.75	Al89	0.87071	0.70703	0.25	Cu7	0.73631	0.60521	0.75
Al40	0.45838	0.12321	0.25	Al90	0.87131	0.79083	0.75	Cu8	0.70348	0.75015	0.25
Al41	0.3748	0.20211	0.25	Al91	0.95394	0.70923	0.75	Al126	0.7991	0.61445	0.25

Al42	0.37658	0.2814	0.75	Al92	0.95377	0.79282	0.25	Mg8	0.77426	0.70784	0.75
Al43	0.45927	0.20244	0.75	Al93	0.87391	0.87749	0.25	Al127	0.70574	0.80836	0.75
Al44	0.46119	0.28203	0.25	Al94	0.87529	0.96016	0.75	Al128	0.71441	0.36265	0.25
Al45	0.37045	0.88596	0.25	Al95	0.9547	0.87639	0.75	Al129	0.79296	0.79784	0.25
Al46	0.37143	0.96456	0.75	Al96	0.95697	0.9597	0.25	Al130	0.79869	0.36609	0.75
Al47	0.45552	0.88481	0.75	Al97	0.20688	0.36934	0.25	Al131	0.63487	0.59675	0.75
Al48	0.45562	0.96493	0.25	Mg1	0.22556	0.45937	0.75	Al132	0.69426	0.6517	0.25
Al49	0.54146	0.044	0.25	Al98	0.29408	0.35883	0.75				
Al50	0.54309	0.1232	0.75	Cu1	0.29636	0.41704	0.25				

Table A.11

The refined fractional coordinates in the atomic model for the 2GPBX_114_relax zone.

2GPBX_114_relax	a = 24.46 Å, b = 25.18 Å, c = 3.98 Å			α = 90.0°, β = 90.0°, γ = 91.2°							
Atoms	x	y	z	Atoms	x	y	z	Atoms	x	y	z
Al1	0.03919	0.04202	0.25	Al51	0.37158	0.96499	0.75	Al101	0.87152	0.70754	0.25
Al2	0.04092	0.12499	0.75	Al52	0.45575	0.8866	0.75	Al102	0.87096	0.79067	0.75
Al3	0.1213	0.04265	0.75	Al53	0.45681	0.96518	0.25	Al103	0.95451	0.70928	0.75
Al4	0.12271	0.12485	0.25	Al54	0.54288	0.04436	0.25	Al104	0.95353	0.79231	0.25
Al5	0.04277	0.20867	0.25	Al55	0.54434	0.12303	0.75	Al105	0.87198	0.87426	0.25
Al6	0.04512	0.29243	0.75	Al56	0.62773	0.04461	0.75	Al106	0.87433	0.95802	0.75
Al7	0.12444	0.20813	0.75	Al57	0.62899	0.12383	0.25	Al107	0.95401	0.87531	0.75
Al8	0.12636	0.29108	0.25	Al58	0.54553	0.20172	0.25	Al108	0.95597	0.95831	0.25
Al9	0.04615	0.376	0.25	Al59	0.54595	0.28035	0.75	Al109	0.29497	0.35871	0.75
Al10	0.04562	0.45912	0.75	Al60	0.63016	0.20306	0.75	Al110	0.28308	0.72457	0.75
Al11	0.12889	0.37747	0.75	Al61	0.63112	0.28238	0.25	Al111	0.28617	0.80454	0.25
Al12	0.12936	0.46098	0.25	Al62	0.54054	0.88596	0.25	Al112	0.3804	0.35976	0.25
Al13	0.04071	0.54315	0.25	Al63	0.54159	0.96562	0.75	Al113	0.46199	0.36148	0.75
Al14	0.03836	0.62754	0.75	Al64	0.62473	0.88666	0.75	Al114	0.46551	0.43943	0.25
Al15	0.12156	0.5453	0.75	Al65	0.62662	0.96562	0.25	Al115	0.36806	0.72958	0.25
Al16	0.11923	0.63049	0.25	Al66	0.71175	0.04324	0.25	Al116	0.37003	0.80858	0.75
Al17	0.03675	0.71133	0.25	Al67	0.71295	0.12411	0.75	Al117	0.45157	0.72729	0.75
Al18	0.03612	0.79446	0.75	Al68	0.79436	0.04185	0.75	Al118	0.45513	0.80524	0.25
Al19	0.1183	0.71432	0.75	Al69	0.79578	0.12407	0.25	Al119	0.30445	0.51554	0.25
Al20	0.11897	0.79622	0.25	Al70	0.71424	0.20465	0.25	Al120	0.36668	0.5688	0.75
Al21	0.0365	0.87676	0.25	Al71	0.71522	0.28562	0.75	Al121	0.54903	0.43715	0.75
Al22	0.03772	0.95925	0.75	Al72	0.79713	0.20612	0.75	Al122	0.53671	0.80695	0.75
Al23	0.11875	0.87865	0.75	Al73	0.79837	0.28806	0.25	Al123	0.54708	0.35814	0.25
Al24	0.11996	0.96061	0.25	Al74	0.79814	0.3705	0.75	Al124	0.63401	0.44216	0.25
Al25	0.20414	0.04263	0.25	Al75	0.79882	0.45239	0.25	Al125	0.71481	0.44882	0.75
Al26	0.20534	0.1235	0.75	Al76	0.71709	0.61359	0.75	Al126	0.7166	0.52811	0.25
Al27	0.28809	0.0429	0.75	Al77	0.79788	0.53621	0.75	Al127	0.62213	0.808	0.25
Al28	0.28937	0.12212	0.25	Al78	0.79554	0.62139	0.25	Al128	0.63094	0.3622	0.75
Al29	0.20672	0.20454	0.25	Al79	0.78778	0.70569	0.75	Al129	0.70834	0.79742	0.75
Al30	0.20859	0.28641	0.75	Al80	0.78822	0.7892	0.25	Al130	0.71541	0.36598	0.25

Al31	0.29048	0.20109	0.75	Al81	0.70852	0.88028	0.25	Al131	0.55041	0.59792	0.25
Al32	0.29238	0.28005	0.25	Al82	0.71038	0.96218	0.75	Al132	0.61264	0.65117	0.75
Al33	0.20876	0.36927	0.25	Al83	0.79074	0.8756	0.75	Cu1	0.29795	0.41863	0.25
Al34	0.20001	0.55312	0.25	Al84	0.79266	0.95857	0.25	Cu2	0.26395	0.56308	0.75
Al35	0.2005	0.63861	0.75	Al85	0.87615	0.04172	0.25	Cu3	0.40643	0.51991	0.25
Al36	0.2023	0.71792	0.25	Al86	0.87789	0.12469	0.75	Cu4	0.3667	0.66761	0.75
Al37	0.20169	0.80076	0.75	Al87	0.95768	0.04173	0.75	Cu5	0.55034	0.49912	0.25
Al38	0.2019	0.88113	0.25	Al88	0.9594	0.12497	0.25	Cu6	0.51065	0.64682	0.75
Al39	0.20284	0.96209	0.75	Al89	0.87936	0.20745	0.25	Cu7	0.65314	0.60363	0.25
Al40	0.28599	0.88436	0.75	Al90	0.88062	0.28994	0.75	Cu8	0.61912	0.74808	0.75
Al41	0.28696	0.96368	0.25	Al91	0.96112	0.20838	0.75	Mg1	0.22678	0.46005	0.75
Al42	0.37277	0.04368	0.25	Al92	0.96309	0.29138	0.25	Mg2	0.29582	0.63389	0.25
Al43	0.37423	0.12235	0.75	Al93	0.881	0.37223	0.25	Mg3	0.37253	0.45097	0.75
Al44	0.45774	0.04412	0.75	Al94	0.88038	0.45534	0.75	Mg4	0.43458	0.63038	0.25
Al45	0.45938	0.12262	0.25	Al95	0.96357	0.37437	0.75	Mg5	0.4825	0.53639	0.75
Al46	0.37552	0.2011	0.25	Al96	0.96261	0.4574	0.25	Mg6	0.54457	0.71574	0.25
Al47	0.37657	0.28076	0.75	Al97	0.87875	0.53915	0.25	Mg7	0.62129	0.53282	0.75
Al48	0.46029	0.20155	0.75	Al98	0.8764	0.6235	0.75	Mg8	0.69033	0.70664	0.25
Al49	0.46137	0.28012	0.25	Al99	0.96009	0.54122	0.75				
Al50	0.37118	0.88636	0.25	Al100	0.95702	0.62545	0.25				

Table A.12

The refined fractional coordinates in the atomic model for the S-I phase.

S-I				a = 18.85 Å, b = 4.05 Å, c = 9.06 Å				α = 90.0°, β = 90.0°, γ = 90.0°			
Atoms	x	y	z	Atoms	x	y	z	Atoms	x	y	z
Al1	0	0	0.99983	Al15	0.19023	0	0.21569	Al29	0.33125	0.5	0.62921
Al2	0	0.5	0.49983	Al16	0.80977	0	0.78388	Al30	0.66875	0.5	0.37033
Al3	0.04719	0	0.30343	Al17	0.19023	0.5	0.71569	Cu1	0.4049	0.5	0.21593
Al4	0.95282	0	0.69619	Al18	0.80977	0.5	0.28388	Cu2	0.59509	0.5	0.78362
Al5	0.04719	0.5	0.80343	Al19	0.14163	0.5	0.41078	Cu3	0.4049	0	0.71592
Al6	0.95282	0.5	0.19619	Al20	0.85837	0.5	0.58881	Cu4	0.59509	0	0.28362
Al7	0.23839	0.5	0.01908	Al21	0.14163	0	0.91078	Mg1	0.40281	0	0.4269
Al8	0.76161	0.5	0.9805	Al22	0.85837	0	0.08881	Mg2	0.59718	0	0.57263
Al9	0.23839	0	0.51908	Al23	0.28507	0.5	0.33002	Mg3	0.40281	0.5	0.9269
Al10	0.76161	0	0.4805	Al24	0.71492	0.5	0.66954	Mg4	0.59718	0.5	0.07263
Al11	0.09453	0.5	0.10676	Al25	0.28507	0	0.83002	Al31	0.48019	0	0.14309
Al12	0.90548	0.5	0.89285	Al26	0.71492	0	0.16954	Al32	0.51981	0	0.85643
Al13	0.09453	0	0.60676	Al27	0.33125	0	0.1292	Al33	0.48019	0.5	0.64309
Al14	0.90548	0	0.39285	Al28	0.66875	0	0.87033	Al34	0.51981	0.5	0.35643
Al1	0	0	0.99983	Al15	0.19023	0	0.21569	Al29	0.33125	0.5	0.62921
Al2	0	0.5	0.49983	Al16	0.80977	0	0.78388	Al30	0.66875	0.5	0.37033
Al3	0.04719	0	0.30343	Al17	0.19023	0.5	0.71569	Cu1	0.4049	0.5	0.21593
Al4	0.95282	0	0.69619	Al18	0.80977	0.5	0.28388	Cu2	0.59509	0.5	0.78362
Al5	0.04719	0.5	0.80343	Al19	0.14163	0.5	0.41078	Cu3	0.4049	0	0.71592
Al6	0.95282	0.5	0.19619	Al20	0.85837	0.5	0.58881	Cu4	0.59509	0	0.28362
Al7	0.23839	0.5	0.01908	Al21	0.14163	0	0.91078	Mg1	0.40281	0	0.4269
Al8	0.76161	0.5	0.9805	Al22	0.85837	0	0.08881	Mg2	0.59718	0	0.57263
Al9	0.23839	0	0.51908	Al23	0.28507	0.5	0.33002	Mg3	0.40281	0.5	0.9269
Al10	0.76161	0	0.4805	Al24	0.71492	0.5	0.66954	Mg4	0.59718	0.5	0.07263
Al11	0.09453	0.5	0.10676	Al25	0.28507	0	0.83002	Al31	0.48019	0	0.14309
Al12	0.90548	0.5	0.89285	Al26	0.71492	0	0.16954	Al32	0.51981	0	0.85643
Al13	0.09453	0	0.60676	Al27	0.33125	0	0.1292	Al33	0.48019	0.5	0.64309
Al14	0.90548	0	0.39285	Al28	0.66875	0	0.87033	Al34	0.51981	0.5	0.35643

Table A.13

The refined fractional coordinates in the atomic model for the S-II phase.

S-II				a = 19.21 Å, b = 4.05 Å, c = 16.70 Å				α = 90.0°, β = 94.4°, γ = 90.0°			
Atoms	x	y	z	Atoms	x	y	z	Atoms	x	y	z
Al1	0	0	0	Al26	0.97135	0.5	0.11495	Mg5	0.26266	0	0.44095
Al2	0	0.5	0.5	Al27	0.19387	0.5	0.18178	Mg6	0.73734	0	0.55905
Al3	0.11264	0.5	0.03542	Al28	0.80613	0.5	0.81822	Mg7	0.26266	0.5	0.94095
Al4	0.88736	0.5	0.96458	Al29	0.19387	0	0.68178	Mg8	0.73734	0.5	0.05905
Al5	0.11264	0	0.53542	Al30	0.80613	0	0.31822	Cu5	0.34888	0	0.01608
Al6	0.88736	0	0.46458	Al31	0.1571	0	0.30071	Cu6	0.65112	0	0.98392
Al7	0.22605	0	0.07248	Al32	0.8429	0	0.69929	Cu7	0.34888	0.5	0.51608
Al8	0.77395	0	0.92752	Al33	0.1571	0.5	0.80071	Cu8	0.65112	0.5	0.48392
Al9	0.22605	0.5	0.57248	Al34	0.8429	0.5	0.19929	Al43	0.42612	0	0.47551
Al10	0.77395	0.5	0.42752	Al35	0.13619	0.5	0.42135	Al44	0.57388	0	0.52449
Al11	0.33674	0.5	0.10651	Al36	0.86381	0.5	0.57865	Al45	0.42612	0.5	0.97551
Al12	0.66326	0.5	0.89349	Al37	0.13619	0	0.92135	Al46	0.57388	0.5	0.02449
Al13	0.33674	0	0.60651	Al38	0.86381	0	0.07865	Cu9	0.44025	0	0.32664
Al14	0.66326	0	0.39349	Cu1	0.23794	0.5	0.32789	Cu10	0.55975	0	0.67336
Al15	0.0812	0	0.1513	Cu2	0.76206	0.5	0.67211	Cu11	0.44025	0.5	0.82664
Al16	0.9188	0	0.8487	Cu3	0.23794	0	0.82789	Cu12	0.55975	0.5	0.17336
Al17	0.0812	0.5	0.6513	Cu4	0.76206	0	0.17211	Mg9	0.47095	0	0.10642
Al18	0.9188	0.5	0.3487	Al39	0.36817	0.5	0.36824	Mg10	0.52905	0	0.89358
Al19	0.05171	0.5	0.2675	Al40	0.63183	0.5	0.63176	Mg11	0.47095	0.5	0.60642
Al20	0.94829	0.5	0.7325	Al41	0.36817	0	0.86824	Mg12	0.52905	0.5	0.39358
Al21	0.05171	0	0.7675	Al42	0.63183	0	0.13176	Al47	0.44198	0.5	0.2336
Al22	0.94829	0	0.2325	Mg1	0.31008	0	0.24296	Al48	0.55802	0.5	0.7664
Al23	0.02865	0	0.38505	Mg2	0.68992	0	0.75704	Al49	0.44198	0	0.7336
Al24	0.97135	0	0.61495	Mg3	0.31008	0.5	0.74296	Al50	0.55802	0	0.2664
Al25	0.02865	0.5	0.88505	Mg4	0.68992	0.5	0.25704				